MECHANISTIC-EMPIRICAL DESIGN OF ASPHALT PAVEMENTS AND AUTONOMOUS TRUCK AND TRUCK PLATOONING IMPACT ON TEXAS HIGHWAY SYSTEM

A Dissertation

by

SHENGXIN CAI

Submitted to the Graduate and Professional School of
Texas A&M University
in partial fulfillment of the requirements for the degree of

DOCTOR OF PHILOSOPHY

Chair of Committee,	Bjorn Birgisson
Committee Members,	Robert Lytton
	Anastasia Muliana
	Amy Epps Martin
	Marcelo Sanchez
Head of Department,	Zachary Grasley

August 2023

Major Subject: Civil Engineering

Copyright 2023 Shengxin Cai

ABSTRACT

Autonomous trucks (ATs) are different from Human-driven trucks (HTs) in traffic characteristics in terms of lane choice and lateral positioning. Current design method (i.e. MEPDG) and existing highway system is to serve traditional traffic configurations. Therefore, it is crucial to develop a framework for studying the potential impact of autonomous truck and truck platooning on the long-term performance of current and future highway system (pavements and bridges).

This dissertation enhanced Pavement ME design by proposing a mechanics-based framework to evaluate autonomous truck and truck platooning impact on long-term performance of Texas highway system. The developed framework consists of input module, traffic characterization module, material property module, pavement performance module, and bridge analysis module. We adopted the traffic load spectra model developed in NCHRP 1-41 with some modifications. The modified traffic model considers axle load distribution for each axle and vehicle type, different wheel wander parameters for HTs and ATs, respectively, AT percentage, and traffic growth rate. Several models were integrated into the material property module that cover pavement temperature, asphalt aging, dynamic modulus of asphalt mixture, Thornthwaite moisture index, equilibrium soil suction for subgrade soil, moisture variation in unbound materials, stress-moisture-dependent resilient modulus of unbound materials, and pavement response. In the pavement performance module, we adopted and improved NCHRP project 1-52 model to predict TDC initiation and propagation in asphalt pavements. The primary improvements to the NCHRP 1-52 model includes the coupling

of the HMA-FM-based crack initiation model, and the incorporation of a novel aging model for asphalt mixture. The bridge module was developed to conduct a high-level prioritization of about 55000 existing Texas bridges due to future platooning loads. Prioritization levels (from 5 to 1) were established for Texas bridge inventory under vertical loading of 6 different platooned truck configurations. The developed framework can be effectively implemented for assessing the potential impact of autonomous truck and truck platooning on the long-term performance of Texas highway system.

DEDICATION

To my parents for their sacrifices and unconditional love.

ACKNOWLEDGEMENTS

Completing this PhD would not have been possible without the support, encouragement, and guidance of numerous individuals and organizations.

Firstly, I would like to express my sincere gratitude to my advisor and committee chair, Dr. Bjorn Birgisson, whose mentorship and unwavering support helped me navigate through the challenges and uncertainties of this journey. His guidance, constructive feedback, and belief in my potential have been instrumental in shaping my research and academic growth.

Second, I would like to thank Dr. Robert Lytton for his constant support and encouragement on both academic and personal sides. I am lucky to work with him during this journey.

I am also deeply grateful to the rest of my committee members, Dr. Amy Epps Martin, Dr. Marcelo Sanchez, and Dr. Anastasia Muliana for their valuable feedback, insightful comments, and suggestions that greatly enhanced the quality of this work.

I would like to extend my gratitude to the staff and faculty of Department of Civil and Environmental Engineering, for providing a stimulating intellectual environment and facilitating various academic and professional opportunities that broadened my horizons and enriched my experience. Special thanks go to my colleagues Dr. Kai Huang, Dr. Ibrahim Onifade, Yadong Guo and others for their help in achieving the project goals.

I could never forget to thank my best friends: Moises Saca, Umme Zakira, Jianxin Huang, and Yong Deng. Their friendship was one of the most valuable gifts I have received in College Station.

Finally, I would like to acknowledge the funding agency TxDOT that provided financial support for this research. Their support was crucial in enabling me to pursue this work and contribute to advancing knowledge in my field.

In conclusion, this dissertation represents the culmination of years of hard work, dedication, and collaboration, and I am indebted to everyone who contributed to its success. Thank you.

CONTRIBUTORS AND FUNDING SOURCES

Contributors

This work was supervised by a dissertation committee consisting of Professor Dr. Bjorn Birgisson, Professor Dr. Robert Lytton, Professor Dr. Amy Epps Martin, and Professor Dr. Marcelo Sanchez of the Department of Civil and Environmental Engineering and Professor Anastasia Muliana of the Department of Mechanical Engineering.

The analyses depicted in Chapter 2 were conducted in part by Kai Huang of the School of Environmental, Civil, Agricultural and Mechanical Engineering from University of Georgia. The methodology for section 6.3.1 was provided by Professor Dr. Matthew Yarnold from department of Civil and Environmental Engineering.

All other work conducted for this dissertation was completed by the student independently.

Funding Sources

This research was based in part upon work supported by TxDOT project #0-6984: “Evaluate Potential Impacts, Benefits, Impediments, and Solutions of Automated Trucks and Truck Platooning on Texas Highway Infrastructure” and TxDOT project #0-7124: “Develop A New Tool for Evaluating Infrastructure and Planning Impacts from Changes in Truck Traffic and Truck Technologies”.

Its contents are solely the responsibility of the authors and do not necessarily represent the official views of the funding institution.

TABLE OF CONTENTS

Page

ABSTRACT ii

DEDICATION iv

ACKNOWLEDGEMENTS v

CONTRIBUTORS AND FUNDING SOURCES vii

TABLE OF CONTENTS viii

LIST OF FIGURES xi

LIST OF TABLES xvii

1. INTRODUCTION 1

1.1. Background 1
1.2. Problem Statement 2
1.3. Objectives of Study 3
1.4. Dissertation Outline 4

2. PERFORMANCE IMPACT OF AUTONOMOUS TRUCKS ON FLEXIBLE PAVEMENTS 7

2.1. Introduction 7
2.2. Traffic Variations 11
2.2.1. Variation of Tire Load Positions 11
2.2.2. Variations of Axle Load on Categories and Magnitude 12
2.3. A Generalized Framework for Evaluating Performance Impact of ATs 18
2.3.1. Framework 18
2.3.2. Impact Indicator 21
2.4. Evaluation and Parametric Analysis of AT Impact on Texas Flexible Pavement 23
2.4.1. Assessment of AT Impact on Major Type of Flexible Pavement Distress 24
2.4.2. Parametric Analysis of Variations of Mixture Parameters 32
2.4.3. Other Factors of ATs Under Development 36
2.5. Conclusions 39

3. A MECHANISTIC-EMPIRICAL MODEL FOR PREDICTING MOISTURE VARIATION IN SUBGRADE SOIL 43

3.1. Introduction 43
3.2. Data Collection and Processing 47
3.3. Model Development 51
3.3.1. Thornthwaite Moisture Index 51
3.3.2. Equilibrium Soil Suction 54
3.3.3. Prediction of Subgrade Soil Moisture Variation with Time and Depth 60
3.4. Model Validation 62
3.4.1. Validation of New TMI Model 62
3.4.2. Validation of Modified Equilibrium Soil Suction Model 63
3.4.3. Validation of Mitchell's Diffusion Equation 66
3.5. Conclusion 70

4. BACKCALCULATION OF RESILIENT MODULUS OF FINE-GRAINED SUBGRADE SOIL FROM FALLING WEIGHT DEFLECTIONS 73

4.1. Introduction 73
4.2. Characterization of Moisture Distribution within Fine-grained Subgrade Soil 77
4.3. Resilient Modulus Model for Fine-grained Subgrade Soil 80
4.4. Nonlinear Forward Calculation Procedure 83
4.5. Nonlinear Backcalculation Procedure 85
4.6. Verification of Nonlinear Backcalculation Module 88
4.7. Temperature Effect on Backcalculated Material Properties 96
4.8. Effect of Drop Load of FWD Test on Backcalculated Material Properties 101
4.9. Effect of Moisture and k-values on Resilient Modulus Distribution within Subgrade soil 103
4.10. Conclusion 104

5. A UNIFIED MECHANICS-BASED FRAMEWORK FOR TOP-DOWN CRACK INITIATION AND PROPAGATION IN ASPHALT PAVEMENTS 108

5.1. Introduction 108
5.2. Development of A Unified Mechanics-based TDC Predictive Framework 114
5.2.1. General Flow Chart of Developed Framework 114
5.2.2. Input Module 115
5.2.3. Material Module 120
5.2.4. TDC Initiation Framework 127
5.2.5. TDC Propagation Framework 128
5.3. Data Collection 132
5.4. Evaluation of NCHRP 1-52 Model 134
5.5. A Case Study 136
5.6. Long-term TDC Prediction 144

5.7. Conclusions 147

6. PERFORMANCE IMPACTS OF TRUCK AUTOMATION AND TRUCK PLATOONING ON TEXAS PAVEMENTS AND BRIDGES 149

6.1. Introduction 149
6.2. Framework for Evaluating Autonomous Truck Effect on TDC Performance of Asphalt Pavements in Texas 151
6.2.1. General Flow Chart of Framework 151
6.2.2. Input Module 152
6.2.3. Traffic Module 154
6.2.4. Material Module 157
6.2.5. Pavement Performance Module 164
6.2.6. Data Collection 167
6.2.7. Results and Discussion 169
6.3. Truck Platooning Effect on Texas Highway Bridges 175
6.3.1. Methodology 175
6.3.2. Prioritization Metric for Bridges Subjected to Truck Platoon Loading 176
6.3.3. Prioritization Results 178
6.4. Conclusion 180

7. SUMMARY, CONCLUSIONS, AND RECOMMENDATIONS 182

7.1. Summary 182
7.2. Conclusions 182
7.2.1. Traffic Characterization Module 182
7.2.2. Material Property Module 183
7.2.3. Pavement Performance Prediction Module 185
7.2.4. Bridge Analysis Module 185
7.2.5. Evaluation of Autonomous Truck effect on TDC Performance of Asphalt Pavements 186
7.3. Limitations and Future Work 187

REFERENCE 188

APPENDIX A 208

LIST OF FIGURES

Page

Figure 1.1 High-level illustration of the process and interdependencies of each module developed in this dissertation (left: Pavement framework; right: bridge framework). 6

Figure 2.1 Tire deviation distributions following normal distribution of 1 million tire repetitions with different standard deviations: 127 mm (5 inches), 254 mm (10 inches), and 381 mm (15 inches).....12

Figure 2.2 Cumulative axle load distribution versus load intervals for all categories using default class, axle type and axle load distribution. 17

Figure 2.3 Number of axle load repetition versus load intervals based on 2×10^6 annual truck traffic repetitions for (a) single and (b) dual tire type. 17

Figure 2.4 Illustration of variation of traffic load spectra, tire deviation, and dynamic modulus of AC layers. 19

Figure 2.5 (a) Typical temperature profiles of pavement at various depths tied to the time of a year (Epps 2002), and (b) a plot of predicted dynamic modulus for twenty-year considering aging.....19

Figure 2.6 Flow chart for evaluation of the impact by autonomous trucks considering variations of traffic load spectra, and tire deviation. 21

Figure 2.7 The driving force profiles (tensile strain at AC bottom) induced by each tire load with (pink curves) and without (dark grey curve) wheel wander.....23

Figure 2.8 The plot of the typical accumulated driving force for (a) TDC, (b) BUC, and (c) rutting for Texas LTPP section 3689.....25

Figure 2.9 Impact factors of ATs (50% and 100% AT) for different distress: (a) BUC, (b) TDC, and (c) rutting: AC, (d) rutting: base, and (e) subgrade on twenty-two (22) Texas LTPP sections. 28

Figure 2.10 Cross comparison of the AT impact with different AT standard deviations and percentages of AT for (a) TDC, (b) BUC, and (c) rutting on Texas LTPP section 1039.....31

Figure 2.11 Parameter analysis of pavement design on AT impact for (a) TDC, (b) BUC, and (c) rutting for a high traffic volume section 1039 (1010 AADTT) and a low traffic volume section 1174 (244 AADTT). 35

Figure 2.12 Typical AT types under Federal Highway Administration (FHWA) vehicle classification (Randall 2012).....37

Figure 2.13 Tire deviation distributions of self-drive trucks and human-operated trucks (TuSimple 2023).....38

Figure 3.1 MnROAD map (map data: Google Earth).....47

Figure 3.2 Classification of MnROAD materials.....50

Figure 3.3 Schematic representation of pavement sections with sensor locations.....51

Figure 3.4 Schematic of maximum available annual moisture depth (d_{am}) (Saha et al. 2019).....57

Figure 3.5. Schematic of mean annual moisture depth (d_m) (Saha et al. 2019).....60

Figure 3.6 Flow chart for predicting soil suction (moisture) within subgrade soil.....62

Figure 3.7 Comparison between TMI-2006 model (Witczak et al. 2006) and new TMI model.....63

Figure 3.8 Comparison between measured and predicted VWC using calibrated model parameters (a) Cell 17 (b) Cell 19 (c) Cell 35 (d) LTPP-0102.....65

Figure 3.9 Comparison between predicted and calibrated equilibrium soil suction.....65

Figure 3.10 Comparison between measured and predicted VWC using calibrated model parameters for other sensors.....67

Figure 3.11 Comparisons of predicted volumetric water content (VWC) at different depths in the subgrade soil in cell 35.....69

Figure 3.12 Comparison between predicted and measured amplitude of volumetric water content (VWC) in cell 35.....70

Figure 4.1 Predicted volumetric water content vs. depth on 05/20/1996 (left) and 08/23/1996 (right).....80

Figure 4.2 Axisymmetric finite element model of pavement section ALABAMA 01-0102.....85

Figure 4.3 Step one of developed backcalculation procedure.....87

Figure 4.4 Step two of developed backcalculation procedure.....88

Figure 4.5 Aggregate gradation of the subgrade in LTPP ALABAMA 01-0102 89

Figure 4.6 Comparison between measured and predicted deflection basins obtained in step one. 90

Figure 4.7 Comparison of backcalculated moduli by LTPP, linear backcalculation and nonlinear backcalculation algorithms. 90

Figure 4.8 Comparison between measured and predicted resilient moduli using the fitted k-values 92

Figure 4.9 Predicted (a) volumetric water content profile and (b) multiplication of volumetric water content, saturation factor, and suction within the subgrade layer on 04/17/1996 for LTPP pavement section ALABAMA 01-0102.....92

Figure 4.10 Comparison between measured and predicted deflection basins obtained in step two. 93

Figure 4.11 Contour of stress- and moisture-dependent modulus (MPa) in subgrade course at a load level of 1068 kPa for pavement section ALABAMA 01-0102. 94

Figure 4.12 Contour of first invariant of stress tensor (MPa) in subgrade course at a load level of 1068 kPa for pavement section ALABAMA 01-0102. 95

Figure 4.13 Comparison of k-values backcalculated using FWD and lab resilient modulus test data, respectively. 96

Figure 4.14 Measured temperatures at depths of 25, 51, and 76mm below pavement surface within asphalt layer in 1996 for LTPP section 01-0102. 97

Figure 4.15 Deflection basins measured at different dates in 1996 for LTPP 01-0102. ..98

Figure 4.16 Drop load of the FWD tests conducted on different days in 1996 for LTPP 01-0102. 98

Figure 4.17 Predcited volumetric water content and suction profiles within subgrade layer at different dates in 1996 for LTPP 01-0102. 98

Figure 4.18 Backcalculated material properties with different temperature and moisture conditions (a) AC modulus; (b) base modulus; (c) k_1 for subgrade layer; (d) k_2 for subgrade layer; (e) k_3 for subgrade layer.....100

Figure 4.19 FWD deflection basins measured at 91.4m away from start of LTPP pavement section 01-0102 mid lane at 7:23AM on 04/17/1996 with different drop loads. 102

Figure 4.20 Backcalculated material properties by different drop loads. 103

Figure 4.21 Resilient modulus profile within subgrade layer predicted using different combinations of mositure condition and k-values 104

Figure 5.1 Illustration of the process and interdependencies of each module in our unified TDC framework. 115

Figure 5.2 Default (a) axle load distribution and (b) accumulative axle load distribution. 119

Figure 5.3 Entire aging evolution of asphalt pavement in terms of binder viscosity (Zhang *et al.* 2019a). 121

Figure 5.4 Workflow of HMA dynamic modulus prediction. 125

Figure 5.5 Flowchart of TDC initiation framework. 128

Figure 5.6 Flowchart of TDC propagation framework. 129

Figure 5.7 Comparison between observed and predicted crack initiation times using NCHRP 1-52 model: (a) measured and predicted initiation time; (b) relative difference between measured data and predicted results (positive values indicate over-predicted and negative values under-predicted). 135

Figure 5.8 Aggregate gradation of asphalt mixture for Florida pavement section St.Lucie (TPK-2C). 137

Figure 5.9 Predicted hourly pavement temperature at different depths of AC in a year for Florida section St.Lucie (TPK-2C). 138

Figure 5.10 Predicted dynamic modulus of AC at different depths in asphalt layer for Florida section St.Lucie (TPK-2C). 138

Figure 5.11 Predicted remaining *ACSE* and *DCSE_lim* with time for Florida section St.Lucie (TPK-2C). 139

Figure 5.12 (a) Predicted dynamic modulus master curve and (b) converted relaxation modulus of asphalt mixture for Florida section St.Lucie (TPK-2C). 140

Figure 5.13 Fitting result of aggregate gradation of asphalt mixture for Florida section St.Lucie (TPK-2C). 140

Figure 5.14 Predicted dynamic modulus gradient parameters (*N* and *K*) with time for Florida section St.Lucie (TPK-2C). 141

Figure 5.15 (a) ANN predicted J-integrals due to different tire loads for single and dual tires and (b) Predicted crack growth for Florida section St.Lucie (TPK-2C). 143

Figure 5.16 CR history of Florida section St.Lucie (TPK-2C). 144

Figure 5.17 Comparison between observed and predicted crack initiation times for Swedish, Florida, and Texas pavement sections used in the study. 146

Figure 5.18 Comparison between observed and predicted pavement failure time. 146

Figure 6.1 Illustration of the process and interdependencies of each module in TDC framework. 152

Figure 6.2 Selected axle configuration of autonomous truck (vehicle class 14).....155

Figure 6.3 Default axle load distribution for (a) HTs and (b) ATs. 156

Figure 6.4 Normally distributed tire deviations with different standard deviations: 127 mm (5 inches), 254 mm (10 inches), and 381 mm (15 inches). 157

Figure 6.5 Training and validation results of k_1, k_2, and k_3 for plastic (P) and non-plastic (NP) subgrade soils. 160

Figure 6.6 Comparison of measured and ANN predicted resilient modulus for plastic (P) and non-plastic (NP) subgrade soil. 162

Figure 6.7 Flowchart of resilient modulus prediction framework. 162

Figure 6.8 Flowchart of dynamic modulus prediction framework for asphalt mixture. 163

Figure 6.9 Flowchart of TDC initiation framework. 165

Figure 6.10 Pavement response calculated by WinJULEA and scipy interpolation, respectively. 166

Figure 6.11 Comparison of pavement response calculated by WinJULEA and scipy interpolation function.....167

Figure 6.12 Geographic locations of selected LTPP sections on Texas freight network. 168

Figure 6.13 Pavement structures of selected LTPP sections. 168

Figure 6.14 Calculated TMI vs. time for LTPP 48-1183. 169

Figure 6.15 ANN-predicted SWCC for base and subgrade layers (LTPP 48-1183). 170

Figure 6.16 Predicted vs. measured resilient modulus for base and subgrade layers (LTPP 48-1183). 171

Figure 6.17 Converged resilient modulus for base and subgrade layers (LTPP 48-1183). 172

Figure 6.18 Predicted crack initiation time caused by human-driven and autonomous trucks, respectively, using simplified traffic model.....174

Figure 6.19 Predicted crack initiation time caused by a mixture of HTs and ATs using complete traffic model. 175

Figure 6.20 Load rating modification factor for two-truck platoons with 20-foot spacing. 177

Figure 6.21 Bridge Prioritization Levels for Future Truck Platoon Loading.....179

Figure 6.22 Geographical locations of bridges categorized as Level 1 - 5 due to platooned truck configuration of two trucks with 20 ft. spacing. 179

LIST OF TABLES

Page

Table 2.1 Vehicle categories classified by vehicle class, axle type, and the number of tires (Lytton *et al.* 2010). 13

Table 2.2 Default normalized vehicle class distribution factor (Lytton *et al.* 2010). 14

Table 2.3 Typical number of axles for each vehicle (Lytton *et al.* 2010). 15

Table 2.4 Default CALD vs. load intervals for each traffic category (Lytton *et al.* 2010). 16

Table 2.5 Distress types and their corresponding driving force. 24

Table 2.6 Selection of design parameters and range of values used for parametric analysis. 33

Table 3.1 Material properties and coefficients of the calibration function for TE and 5TE (Teshale et al. 2019) 50

Table 3.2 Day Length correction factors (McKeen and Johnson 1990). 53

Table 4.1. Pavement Structures, Material Models, Parameters used in the forward calculation Program. 85

Table 4.2 Input for the moisture prediction model 89

Table 5.1 Distribution of vehicle classes (USDOT 2016). 119

Table 5.2 Average number of axle for each vehicle class (USDOT 2016). 119

Table 5.3 Categories of traffic load (Lytton *et al.* 2010). 120

Table 5.4 Summary of Input Variables for the Top-down Crack Propagation Framework. 132

Table 5.5 Input data of Florida pavement section St.Lucie (TPK-2C). 136

Table 5.6 Fracture Coefficients and Performance-related Material Properties. 145

Table 6.1 Distribution of vehicle classes (USDOT 2016). 155

Table 6.2 Average number of axle for each vehicle class (USDOT 2016). 155

Table 6.3 Categories of traffic load (Lytton *et al.* 2010). 156

Table 6.4 Input and output of ANN for plastic and non-plastic subgrade soil. 160

Table 6.5 Input for the resilient moduli prediction framework.....169

Table 6.6 Predicted resilient modulus for base, subbase, and subgrade layers.....172

Table 6.7 Condition Factors for each bridge Appraisal Rating.....178

1. INTRODUCTION

1.1. Background

The mechanistic empirical pavement design guide (MEPDG) was developed under the National Cooperative Highway Research Program (NCHRP) Project 1-37A (ARA Inc. 2004) to overcome the limitations of the empirical design procedures in the American Association of State Highway and Transportation Officials (AASHTO) Guide for Design of Pavement Structures (AASHTO 1993). MEPDG replaced the AASHTO design procedure due to the inability of the AASHTO methods to incorporate significant material properties into the design procedure, not recognizing the impacts of various climatic conditions, and its over extrapolation of traffic projections beyond what was encountered at the AASHO Test Road.

Research efforts to develop improved tools and models for more accurate consideration of varying design scenarios and improved pavement performance prediction led to the development of the mechanistic-empirical pavement design guide (MEPDG) which was incorporated into AASHTOWare Pavement ME Design™ software. PavementME incorporates mechanistic approach in the calculation of stress, strain and deformation fields in the pavement structure due to a specific combination of material types and pavement structure under given climatic condition and traffic loads. Unlike the AASHTO 1993 design guide, PavementME combines the mechanistically obtained stress, strain and deformation fields with empirical distress models to correlate predicted cumulative damage to the observed pavement performance.

The introduction of PavementME promises to represent significant improvement in pavement design and performance evaluation allowing the prediction and optimization of pavement performance with respect to specific failure or distress modes in both flexible and rigid pavements. Unfortunately, some state DOTs have not yet realized the potential benefits of PavementME due to various implementation and development issues, such as the demand of conducting extensive dynamic modulus tests, lack of well-documented pavement sections for local calibration, as well as some of the key models in the Pavement ME framework currently being placeholders.

The main components of the Pavement ME include: (a) the climate module to predict the temperature distribution in the pavement layers and account for the environmental effects on the pavement performance using the Enhanced Integrated Climate Model (EICM); (b) the materials characterization module to obtain the relevant material properties of HMA layer, PCC layer and unbound granular layer materials; (c) the traffic module to characterize traffic load on the pavement; (d) the pavement response module to account for the effect of the pavement structural configuration and various traffic loads on the resulting stress and strain fields; (e) the damage accumulation module to predict the amount of distress in the pavement structure by using empirical transfer functions.

1.2. Problem Statement

Autonomous vehicles (AVs) have gained tremendous attention over the past a few years due to progressive development in Intelligent Transportation Systems (ITS). Autonomous trucks (ATs) are different from human-driven trucks (HTs) in terms of lane

choice and lateral positioning, which might introduce new risks and challenges for current infrastructure system. For example, the application of autonomous truck and truck platooning can potentially reduce wheel wander and increase highway capacity due to lane-keeping system and elimination of human factors, which will lead to faster deterioration of pavement condition and shorten pavement service life (Forrest and Konca 2007, VdM Steyn and Fisher 2008, Litman 2017, Georgouli *et al.* 2021). Therefore, it is crucial to study the potential impact of autonomous truck and truck platooning on the long-term performance of existing highway system (pavements and bridges) and structure design of new pavements and bridges accommodating the epoch of AT.

1.3. Objectives of Study

This dissertation aims for the enhancements to pavement ME design by proposing a mechanics-based framework to study the potential autonomous truck and truck platooning impact on the long-term performance of Texas highway system (pavements and bridges). The main goals of this research were summarized in the following.

- Develop a traffic load spectra model that considers axle load distribution for each axle and vehicle type, different wheel wander parameters for human-driven trucks and autonomous trucks, autonomous truck percentage, and traffic growth rate.
- Develop a mechanistic-empirical model for predicting moisture variation in subgrade soil.
- Develop a FWD-based backcalculation program to determine stress-moisture dependent resilient modulus of unbound materials.

- Develop a unified mechanics-based framework to evaluate long-term top-down cracking performance (crack initiation and propagation) of asphalt pavements.
- Conduct a high-level prioritization study for about 55000 existing bridges in Texas to evaluate the potential bridge performance under vertical loading of 6 different platooned truck configurations.

1.4. Dissertation Outline

This dissertation is divided into 7 chapters. A brief review of each chapter is presented as follows.

Chapter 1 consists of study background, problem statement, study objectives, and dissertation outline.

Chapter 2 presents a generalized framework to characterize traffic for both human-driven trucks and autonomous trucks. Wheel wander, axle load spectra, autonomous truck percentage are considered in the traffic model. The impact indicator was introduced to quantify the autonomous truck impact on the performance of asphalt pavements in TX in terms of top-down fatigue cracking (TDC), bottom-up fatigue cracking (BUC), and rutting. A parametric study is conducted to identify the significance of some key parameters in different pavement designs in responds to autonomous truck (AT) implementation, and to test how sensitive a pavement response to autonomous trucks is in terms of its performance.

Chapter 3 presents a mechanistic-empirical model for predicting moisture variation in subgrade soil by coupling a modified ME-based equilibrium soil suction model and

Mitchell's diffusion equation. The proposed moisture prediction mode was validated using the moisture data collected from MnROAD and LTPP databases.

Chapter 4 introduces a FWD-based backcalculation program to backcalculate stress-moisture-dependent resilient modulus of subgrade soil using COMSOL Multiphysics. Lytton model was employed to characterize the stress dependency and moisture sensitivity of subgrade resilient modulus. The new moisture prediction model was incorporated into the program to predict moisture and suction profile on the date when FWD testing was conducted. We used Bound Optimization by Quadratic Approximation (BOBYQA) as the optimization method to backcalculate the parameters used in Lytton model. The backcalculation program was verified using the FWD data collected from LTPP database.

Chapter 5 introduces a new unified mechanics-based framework to predict TDC initiation and propagation in asphalt pavements. The unified framework was developed based on NCHRP 1-52 model and improved the robustness of NCHRP 1-52 model by replacing their empirical crack initiation model with a HMA-FM-based crack initiation model and incorporating with a novel aging model for asphalt mixture. The proposed framework was validated by 18 pavement sections from different geographical locations with well-documented performance history and material properties.

Chapter 6 presents a framework for evaluating performance impact of autonomous truck and truck platooning on Texas highway system (pavements and bridges). This framework consists of pavement module and bridge module. In the pavement module, the mechanics-based TDC initiation sub-framework introduced in chapter 5 was

improved to study the effects of autonomous truck loads and autonomous truck percentage on the TDC performance of asphalt pavements. The major improvement includes the incorporation of a more realistic traffic load spectra model that distinguishes HTs from ATs, and a stress-moisture-dependent resilient modulus prediction model for unbound layers. In the bridge module, we developed an approach to conduct a prioritization study in about 55000 existing Texas bridges due to future platooning loads. The developed approach leveraged the National Bridge Inventory (NBI) database along with prior research to evaluate each bridge structure in Texas.

Chapter 7 presents the summary, conclusions, limitations, and recommendations of the research work included in this dissertation.

Two generalized flowcharts are presented in Figure 1.1 to illustrate the process and interdependencies of each module developed in this dissertation.

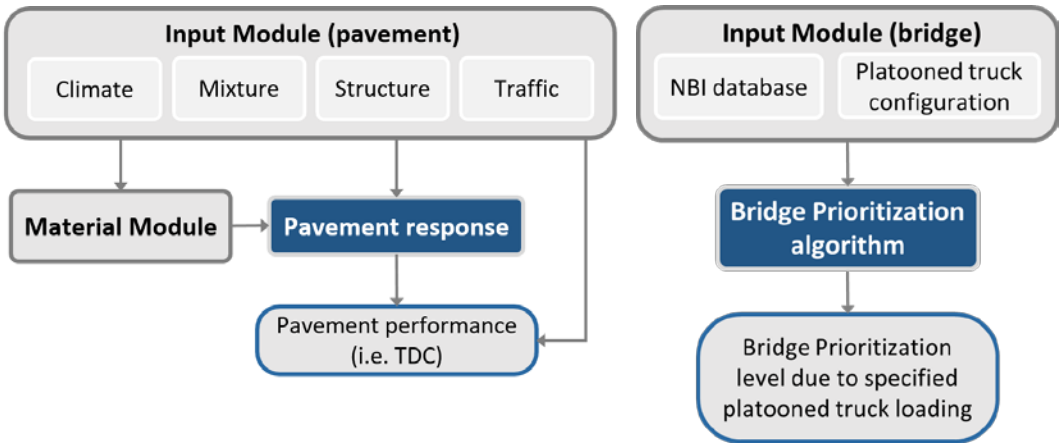

Figure 1.1 High-level illustration of the process and interdependencies of each module developed in this dissertation (left: Pavement framework; right: bridge framework).

2. PERFORMANCE IMPACT OF AUTONOMOUS TRUCKS ON FLEXIBLE PAVEMENTS

2.1. Introduction

Automated vehicles (AVs) are enabled by substantial advances in sensing, communication, and computer science, and have received significant worldwide interest. The Society of Automotive Engineers International (SAE International 2018) published the definitions of six levels of driving automation, ranging from no driving automation (level 0) to full driving automation in all circumstances (level 5), while the level 3 automation has been achieved in the current AVs market. Polls (Rainie *et al.* 2022) have shown concerns from the public regarding riding in a driverless vehicle and sharing the road with driverless vehicles. Nevertheless, the expectation of AVs from the market is exceedingly positive despite that high-level automated vehicles are not available yet. The U.S. Department of Transportation announced a $100 million budget for automated vehicle research and development in 2018, including a $60 million grant for demonstration projects that test the feasibility and safety for private companies(Shepardson 2018). The proportion of AVs circulating (Liu *et al.* 2019) was predicted to reach 20% by the end of the 2030s and occupy 50% by the end of the 2050s. Autonomous truck (AT) as a new category of vehicles has been making their progress towards commercial implementation that will profoundly impact the whole industry of the transportation of goods(Ackerman 2021). TuSimple, an automated vehicle company, has completed the first fully automated test of a heavy-duty autonomous truck on open public roads for more than 80 miles of travel in Arizona in December of 2021, among a

long list of other companies developing their trucks without a driver in the cab. A report (Research and Markets 2022) regarding autonomous trucking market forecasts predicted growth of the global market of ATs to 5.2 billion US dollars by 2027, at a compound annual growth rate of 4.6% between 2021 and 2027.

Birgisson et al. (Birgisson *et al.* 2020) presented a detailed review to identify the potential impacts, benefits, impediments, and solutions for autonomous truck and truck platooning technologies. AT as an essential subset of AV relies on underlying technology such as sensors (cameras and LiDAR sensors, etc. (Dennis *et al.* 2019)), communications (Dedicated Short-Range Communications (DSRC) and 5G (Yoshino *et al.* 2018)), and software systems (artificial intelligence technologies (Greer *et al.* 2018)) that are mainly used for identifying objects, measuring vehicle speed, and maintaining vehicle position when cruising (Slowik and Sharpe 2018). AT technologies would provide potential solutions for many problems caused by traditional trucks such as increasing CO2 emission, energy efficiency, the human-error induced accident occurrence, and exacerbating traffic congestion (Weisser 1998, Fagnant and Kockelman 2015, Litman 2017, Vahidi and Sciarretta 2018). Still, commercial operations of ATs need to consider many other aspects than traditional trucks, including safety (Greer *et al.* 2018), environmental (Sun and Yin 2019), roadway capacity, labor (Short and Murray 2016), and economic impacts (Chottani *et al.* 2018).

To better accommodate AT, automation technologies and emerging intelligent transportation systems should be tied together to pose a great influence on the fuel efficiency and environmental impacts of medium- and heavy-duty vehicles (National

Academies of Sciences and Medicine 2020). Fitzpatrick et al. (Fitzpatrick *et al.* 2017) suggested that the investment in infrastructure should be focused on road widening with better lane markings, improved geometric design, and higher quality pavements with thicker pavement layers. The design and performance of pavements depend on climate, truck traffic, pavement configuration, and material properties (Mallick and El-Korchi 2008). ATs are different from Human-driven trucks (HTs) in traffic characteristics in terms of lane choice and lateral positioning within the lane. It is crucial to study the impact of ATs on the long-term performance of existing pavement structures and the design of new pavements accommodating the epoch of AT.

HTs normally do not follow the exact path on a road while traveling. The term, wheel wander, is used to characterize this phenomenon and is defined as the lateral deviations of tire loads over a pavement cross-section (Gungor 2018). Wheel wander of a human-driven truck is affected by several factors including weather conditions (i.e. wind speed and precipitation), environment, time, type of vehicle, traffic conditions, road characteristics (i.e. road type, road configuration, road roughness, road markings) (Buiter *et al.* 1989), and rutting depth (Blab and Litzka 1995). Field measurements showed that the wheel-path of HTs is normally distributed within a traffic lane (Buiter *et al.* 1989). The standard deviation characterizes the spread of wheel loads, which ranges from 8 to 24 inches depending on the lane width, vehicle size, etc. 10 inches of standard deviation is taken in most pavement designs (ARA Inc. 2004). The wheel wander of ATs is programmed by the vehicle computer controlling the steering system using a specific lane-keeping algorithm. Therefore, ATs, theoretically, can follow any predefined lateral

distributions such as channelized wheel path with a much smaller wheel wander. Narrower wheel wander helps with increasing traffic safety due to a more predictable traffic trajectory and increasing passenger comfort. However, the studies (Forrest and Konca 2007, VdM Steyn and Fisher 2008, Litman 2017, Georgouli *et al.* 2021) showed that the channelized wheel loads caused faster damage accumulation on a specific spot of the pavement thereby yielding a reduced service life. Noorvand (Noorvand *et al.* 2017) compared the effect of uniform distribution of wheel loads with the zero-wander scenario. Different combinations of ATs and HTs were considered in the analysis of the long-term performance of asphalt pavements using Pavement ME software. It was found that the inclusion of uniformly distributed ATs improves the long-term performance or reduces the required design thickness of pavements, whereas the opposite occurs when there is zero-wander is deployed in ATs. Siddharthan et al. (Siddharthan *et al.* 2017) developed a Monte-Carlo simulation scheme to study the wheel wander effect of trucks on the pavement performances. The proposed method calculates pavement responses (strains in different directions) of 10000 randomly generated wheel wanders that conform to normal distribution.

To this end, this research focuses on addressing the following question: How autonomous trucks will affect the performance of current pavements due to their unique traffic characteristics compared with HTs? In this context, we describe the following key points that are necessary for a realistic characterizing the traffic for both ATs and HTs: (i) the variation of the position of tire loads (wheel wander); (ii) the variation of axle loads on categories and magnitude (load spectra); and (iii) the variations of how many

ATs in service on the road (percentages of AT loads in all truck loads). Following that, we propose a new generalized framework based on emphasized aspects to appropriately assess the impact of AT. The proposed framework is applied to evaluate the AT impact on Texas flexible pavement. Additionally, a parametric study is conducted to identify the significance of some key parameters in different pavement designs in response to AT implementation. Finally, some actual factors and characteristics of ATs are to be determined in the future since ATs still have a long journey before being commercially available and the narrative of their utilization remains unknown.

The rest of the paper is organized as follows. Section 2.2 defines all the traffic related variations and the detailed mathematical formulation that are necessary to be included in performance impact analysis. We propose a generalized framework for evaluating ATs impact in section 2.3. Section 2.4 presents extended evaluation and a parametric analysis of AT impact on Texas flexible pavement. Finally, we wrap up with a summary and conclusions in Section 2.5.

2.2. Traffic Variations

2.2.1. Variation of Tire Load Positions

Human-driven truck wheels are distributed randomly at different locations on specific pavement sections. Their lateral positions with respect to the center of wheel-path are called transverse wheel wander that significantly affect loading conditions and pavement performance. Field measurements exhibit the positions where the tires of HTs landed following a normal distribution with a specific standard deviation in a traffic lane (Buiter *et al.* 1989). The standard deviation of its probability density characterizes the spread of

wheel loads, which usually range from 8 to 24 inches depending on lane width, weight and size of vehicles, etc. As an illustration example, Figure 2.1 shows the tire deviation distributions of 1 million tire repetitions following a normal distribution with different standard deviations: 127 mm (5 inches), 254 mm (10 inches), and 381 mm (15 inches). The concentration of tire loads is much higher when the standard deviation is smaller, and would cause a higher level of distress around the center of wheel-path. Having defined the standard deviation, tire location on the cross-section of pavement for both HTs and ATs can be precisely characterized statistically.

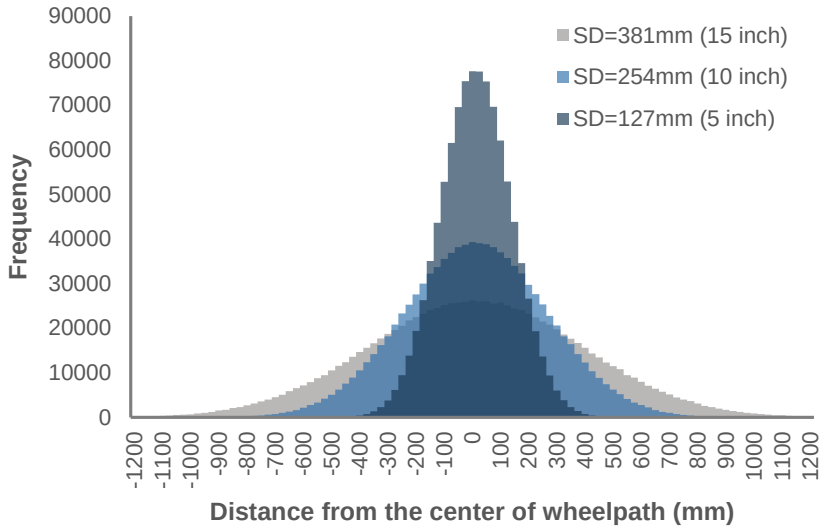

Figure 2.1 Tire deviation distributions following normal distribution of 1 million tire repetitions with different standard deviations: 127 mm (5 inches), 254 mm (10 inches), and 381 mm (15 inches).

2.2.2. Variations of Axle Load on Categories and Magnitude

The tire load repetitions also vary in magnitude depending on the load weight and the category of trucks. This work employs a hierarchical approach to characterize the

normalized axle load distribution for each axle and vehicle type using typical Weigh-In-Motion (WIM) data gathered from field. Federal Highway Administration (FHWA) characterizes traffic into thirteen (13) vehicle classes. Vehicle class 1 to class 3 are the light vehicle groups that are neglected in pavement performance analysis since they do not have a significant impact on pavement distress. Vehicle classes 4 to 13 are the heavy load categories that are the cause of pavement distress. The axle types for the vehicles in each class are categorized as single, tandem, tridem, and quadrem axles. Additionally, each axle has single or dual tires. According to the mentioned FHWA vehicle classification and following NCHRP 1-41 (Lytton et al. 2010), the traffic load is finally characterized into 8 categories shown in Table 2.1 that is used as traffic input for the pavement performance evaluation.

Table 2.1 Vehicle categories classified by vehicle class, axle type, and the number of tires (Lytton *et al.* 2010).

Vehicle Class	Single axle	Tandem axle	Tridem axle	Quadrem axle
4	1	3	5	7
5				
6		4	6	8
7				
8	2			
9				
10				
11				
12				
13				

single tire dual tire

The detailed axle load distribution for each load category can be obtained from the WIM data for each axle type of each vehicle class. In case WIM data is not available, the annual average daily truck traffic (AADTT) is used to estimate the number of axle loads for each category using a model of cumulative axle load distribution (CALD) with a

series of default distributions (Lytton *et al.* 2010). A typical CALD is a sigmoidal-shaped curve that is obtained from summarizing the individual load intervals in each load category. NCHRP 1-41 (Lytton *et al.* 2010) employed the Gompertz model to characterize the statistic properties of the CALD,

$$y = \alpha \exp[-\exp(\beta - \gamma x)] \quad \textbf{(2.1)}$$

where x is load interval (lb), α, β, and γ are the shape parameters defining the curve. With the default parameters summarized from historical traffic data, a series of traffic data with the information of vehicle category, axle type, tire type, and load interval can be estimated based on AADTT in following steps:

1) The following equation expends AADTT data to the annual number of trucks for each vehicle class based on a normalized vehicle distribution,

$$DNT_i = AADTT \cdot P_i^{VC} \quad \textbf{(2.2)}$$

where DNT_i is the daily number of trucks for vehicle class i, P_i^{VC} is normalized truck class distribution factor of class i shown in Table 2.2 that is obtained from the principal arterials in the roadway function class and the major multi-trailer truck route in Truck Traffic Classification.

Table 2.2 Default normalized vehicle class distribution factor (Lytton *et al.* 2010).

Vehicle class	4	5	6	7	8	9	10	11	12	13
Distribution factors (percentage)	1.8	24.6	7.6	0.5	5.0	31.3	9.8	0.8	3.3	15.3

2) Using the typical number of axles for each vehicle shown in Table 2.3, the daily number of trucks for each vehicle class, DNT_i, is derived to the daily number of axle loads for each vehicle class and axle type,

$$DNA_{ij} = DNT_i \cdot P_{ij}^{AN} \tag{2.3}$$

where DNA_{ij} is the daily number of axle load for vehicle class i and axle type j ($j=1$: single axle, …, $j=4$: quadrem axle), P_{ij}^{AN} is typical number of axles for each vehicle class listed in Table 2.3. Here, the subscripts i and j do not follow the Einstein notation convention.

Table 2.3 Typical number of axles for each vehicle (Lytton *et al.* 2010).

Vehicle class	Single axle	Tandem axle	Tridem axle	Quadrem axle
4	1.62	0.39	0.00	0.00
5	2.00	0.00	0.00	0.00
6	1.02	0.99	0.00	0.00
7	1.00	0.26	0.83	0.00
8	2.38	0.67	0.00	0.00
9	1.13	1.93	0.00	0.00
10	1.19	1.09	0.89	0.00
11	4.29	0.26	0.06	0.00
12	3.52	1.14	0.06	0.00
13	2.15	2.13	0.35	0.00

single tire dual tire

3) According to the categorization method shown in Table 2.1, the daily number of axle load DNA_{ij} are summarized into eight traffic load categories and are rewritten as DNA_k, where k is the vehicle categories. Then, the daily number of axle load is attributed to different load intervals according to their distributions,

$$DNA_{km}^{INT} = DNA_k \cdot P_{km}^{INT} \tag{2.4}$$

where k is vehicle categories (1~8), m is the order of load magnitude internals (1-38), P_{km}^{INT} is the default distribution of load intervals for each traffic category calculated based on the CALD listed in Table 2.4 and illustrated in Figure 2.2.

Table 2.4 Default CALD vs. load intervals for each traffic category (Lytton *et al.* 2010).

	Category							
	1	2	3	4	5	6	7	8
Axle type	Single		Tandem		Tridem		Quadrem	
Tire type	Single	Dual	Single	Dual	Single	Dual	Single	Dual
Interval No. 1~38	From 3000 lb, 1000 lb interval		From 6000 lb, 2000 lb interval		From 3000 lb, 3000 lb interval		From 12000 lb, 3000 lb interval	
1	0.132	0.0896	0.0971	0.0269	0.5835	0.0754	0.4005	0.0056
2	0.2541	0.1941	0.1654	0.0596	0.7411	0.1318	0.5384	0.0187
3	0.3958	0.3282	0.2494	0.1109	0.8465	0.2044	0.6578	0.0472
4	0.5341	0.4689	0.3424	0.1799	0.9115	0.2882	0.7532	0.0962
5	0.6542	0.5977	0.4373	0.2624	0.9498	0.3772	0.8255	0.166
6	0.7505	0.7048	0.5281	0.3522	0.9718	0.4658	0.8783	0.2523
7	0.8235	0.7884	0.611	0.4431	0.9842	0.5496	0.916	0.3478
8	0.8769	0.8508	0.6837	0.53	0.9912	0.6256	0.9423	0.4449
9	0.9149	0.896	0.7457	0.6094	0.9951	0.6924	0.9606	0.5373
10	0.9416	0.9281	0.7973	0.6796	0.9973	0.7497	0.9732	0.621
11	0.9601	0.9505	0.8396	0.7398	0.9985	0.7979	0.9818	0.694
12	0.9728	0.9661	0.8738	0.7905	0.9992	0.8379	0.9876	0.7557
13	0.9815	0.9768	0.9011	0.8325	0.9995	0.8706	0.9916	0.8067
14	0.9875	0.9842	0.9228	0.8668	0.9997	0.8971	0.9943	0.8481
15	0.9915	0.9892	0.9399	0.8945	0.9999	0.9184	0.9962	0.8813
16	0.9942	0.9927	0.9533	0.9167	0.9999	0.9355	0.9974	0.9076
17	0.9961	0.995	0.9637	0.9344	1	0.9491	0.9982	0.9284
18	0.9974	0.9966	0.9719	0.9484		0.9599	0.9988	0.9446
19	0.9982	0.9977	0.9782	0.9596		0.9684	0.9992	0.9572
20	0.9988	0.9984	0.9832	0.9683		0.9752	0.9995	0.967
21	0.9992	0.9989	0.987	0.9752		0.9805	0.9996	0.9746
22	0.9994	0.9993	0.9899	0.9806		0.9847	0.9997	0.9805
23	0.9996	0.9995	0.9922	0.9848		0.988	0.9998	0.985
24	0.9997	0.9997	0.994	0.9882		0.9906	0.9999	0.9885
25	0.9998	0.9998	0.9954	0.9907		0.9926	0.9999	0.9911
26	0.9999	0.9998	0.9964	0.9928		0.9942	0.9999	0.9932
27	0.9999	0.9999	0.9972	0.9944		0.9954	1	0.9948
28	0.9999	0.9999	0.9979	0.9956		0.9964		0.996
29	1	1	0.9984	0.9966		0.9972		0.9969
30			0.9987	0.9973		0.9978		0.9976
31			0.999	0.9979		0.9983		0.9982
32			0.9992	0.9984		0.9987		0.9986
33			0.9994	0.9987		0.9989		0.9989
34			0.9995	0.999		0.9992		0.9992
35			0.9997	0.9992		0.9994		0.9994
36			0.9997	0.9994		0.9995		0.9995
37			0.9998	0.9995		1		1
38			1	1				

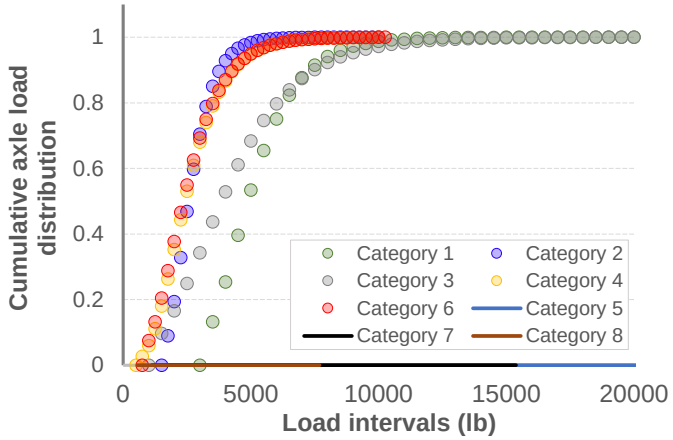

Figure 2.2 Cumulative axle load distribution versus load intervals for all categories using default class, axle type and axle load distribution.

4) Finally, for sake of simplicity, the daily number of axle loads with different levels of load intervals of each category, DNA_{km}^{INT} with eight traffic categories are summarized into the ones for two different tire types (single tire and dual tire), DNA_{nm}^{INT}, where n indicates tire type ($n=1$ represents single tire, $n=2$ represents dual tire). Using the aforementioned steps, Figure 2.3 shows the number of axle load repetitions versus load intervals based on 2,000,000 annual trucks for single tire and dual tire loads.

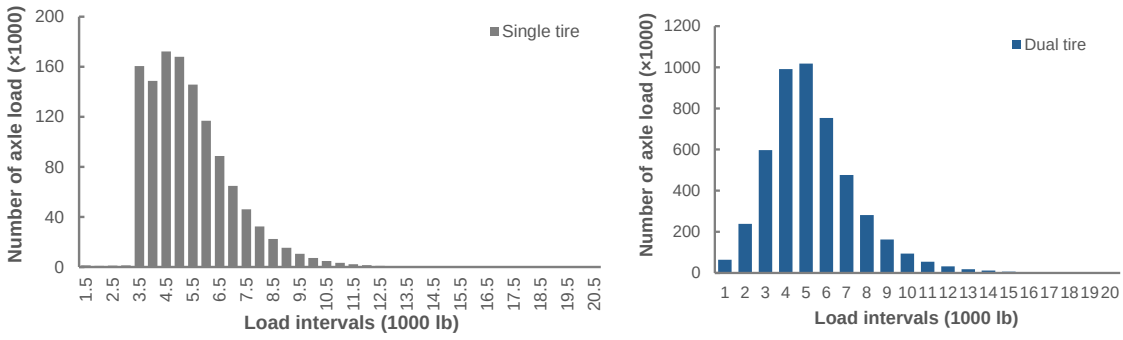

(a) (b)

Figure 2.3 Number of axle load repetition versus load intervals based on 2×10^6 annual truck traffic repetitions for (a) single and (b) dual tire type.

2.3. A Generalized Framework for Evaluating Performance Impact of ATs

2.3.1. Framework

To emerge the impact of AT, the pavement performance analysis for both HTs and ATs are necessary to be performed for us to compare. The most obvious differences between the loading patterns of the HTs and AT are the lateral wheel wander and load spectra. Pavement performance subjected to ATs can be evaluated using the same framework by adjusting the standard deviation, load spectra of load magnitude, among other factors like the proportion of ATs operating on road in total traffic, etc., if these data are available. In the analysis, every tire load's location and magnitude during pavement life can be sampled from the probability given in Figure 2.1 and Figure 2.3 for example. Figure 2.4 illustrates the scenarios of tire loads that can possibly be located and be in a certain load magnitude intervals, along with the age- and temperature-dependent mechanical properties of the AC layer when the tire load applies.

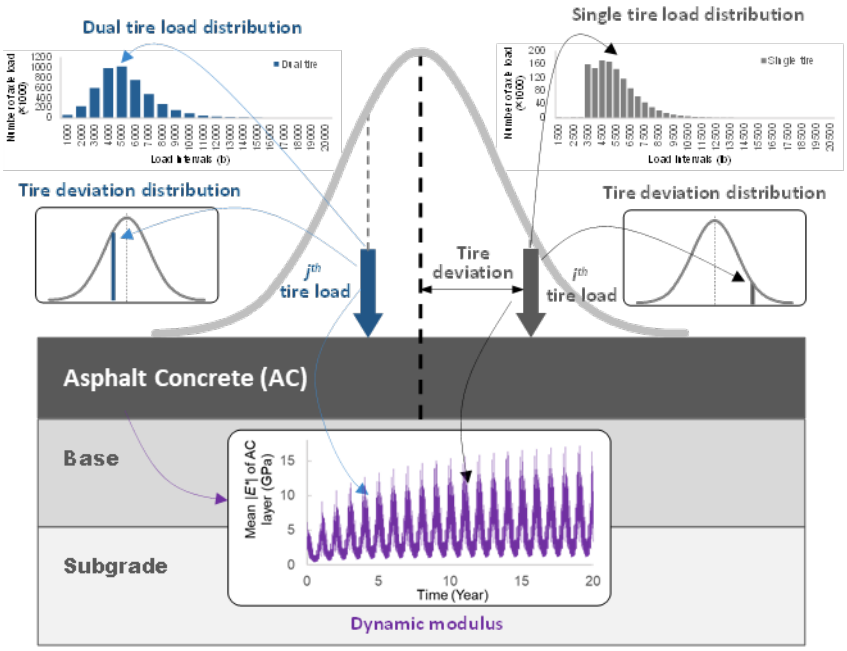

Figure 2.4 Illustration of variation of traffic load spectra, tire deviation, and dynamic modulus of AC layers.

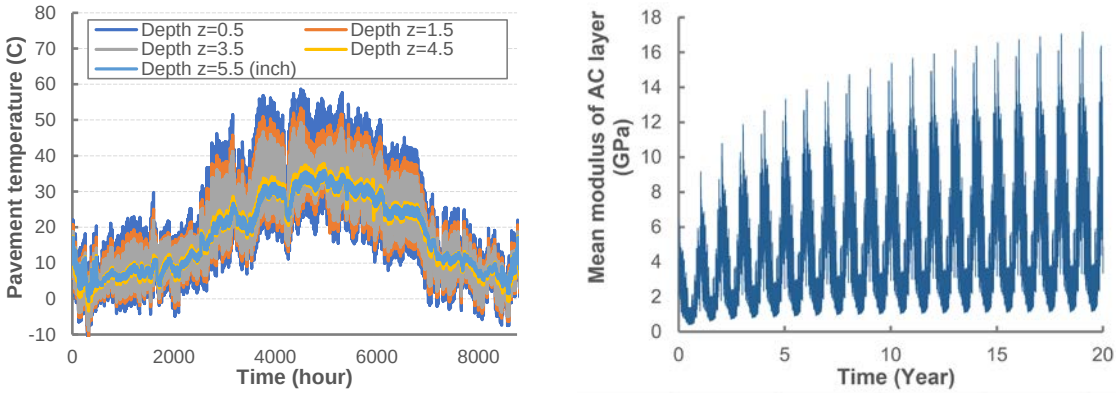

(a) (b)

Figure 2.5 (a) Typical temperature profiles of pavement at various depths tied to the time of a year (Epps 2002), and (b) a plot of predicted dynamic modulus for twenty-year considering aging.

This work adopts a similar framework structure and uses the same material properties module presented in (Huang *et al.* 2021). Given a temperature profile of pavement throughout a year (Figure 2.5(a)), the dynamic modulus of asphalt concrete can be

estimated (Figure 2.5(b)) using the material module presented in (Huang *et al.* 2021). A generalized flowchart is presented in Figure 2.6 designed specifically for the evaluation of the impact of ATs considering their unique loading characteristics. Pavement sections are designed to accommodate the specific design conditions and exhibit different variations in modulus of AC layers, resilience modulus of unbound layers, geographical climate conditions, etc. Thus, the performance impact of ATs on each pavement section would vary and should be examined individually. The following points are emphasized to appropriately assess the impact of AT:

- The variability of the lateral wheel wander follows a normal distribution with a standard deviation of 10 inches (25.4 cm) for HTs, compared to a much smaller standard deviation for ATs.
- The variation of tire load magnitude follows the axle load distribution modelled by the Gompertz model with default parameters used in NCHRP 1-41 (Lytton *et al.* 2010), which is the same for both HTs and ATs since the load spectra for ATs has not been adequately studied up to now.
- In the framework, we can define the percentages of truck traffic that are from ATs. The tire deviations of HTs and ATs sharing the same pavement are sampled separately from the normal distributions with different standard deviations.
- Depending on the objectives of the analysis, the effects are investigated specifically based on the driving force responsible for different pavement distress types (e.g., top-down cracking) at the location (e.g., pavement surface) where the distress is likely to occur.

In this work, we only consider the impact of ATs at a general level without employing any specific models to predict the development of certain distress like rutting, top-down cracking, etc. The accumulated value of distress driving force is chosen to be an impact indicator due to its straightforwardness and objectivity that is not subjected to any bias by a specific model. The accumulated values of distress driving force profile induced by both AT loads and human-driven truck loads will be obtained and compared.

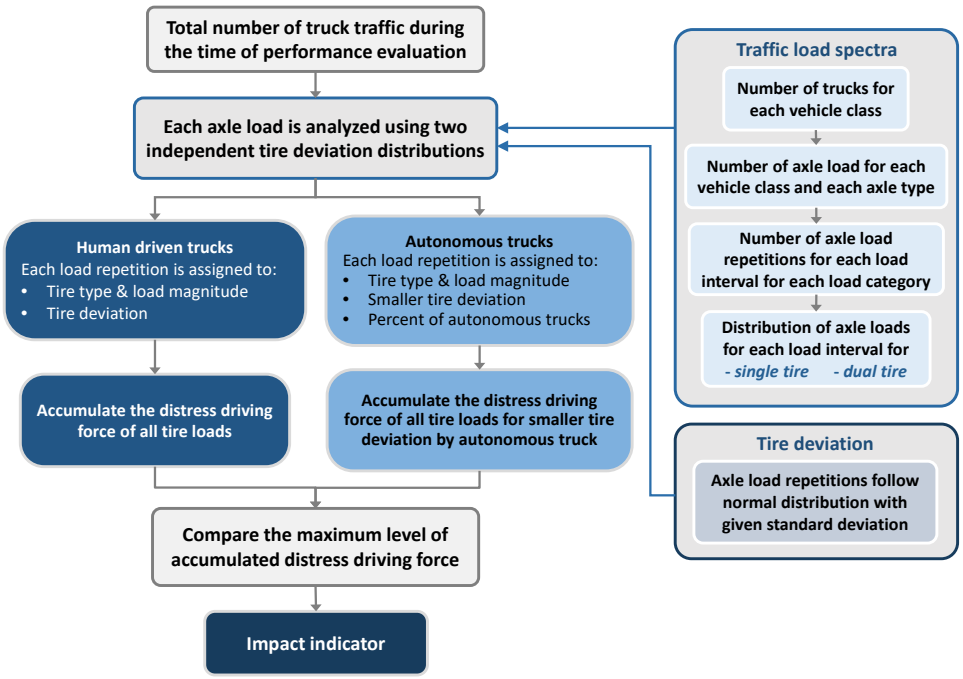

Figure 2.6 Flow chart for evaluation of the impact by autonomous trucks considering variations of traffic load spectra, and tire deviation.

2.3.2. Impact Indicator

The horizontal tensile strain at the bottom of the AC layer is commonly considered as the cause of fatigue cracking of AC pavements, which is taken as an example of distress driving force to analyze the severity of performance impact by AT. As illustrated in

Figure 2.7, the load position and load magnitude of every single tire load (blue and grey arrows) are sampled from the probabilities calculated in the previous section. The number of tire loads on a pavement section over its lifetime is statistically large enough. Through the mechanical response analysis module, we obtain a tensile strain profile at the bottom of the AC layer induced by each tire load. The variations in tire location, load magnitude, and the modulus of each layer will result in different strain profiles. The strain profiles $\varepsilon(x)$ induced by each tire load of HTs and ATs are both recorded, which are shown as blue and dark grey curves in Figure 2.7, respectively. The blue curves are the tensile strain profiles caused by HTs with wider tire deviation, while the grey curves are the profiles induced by ATs with narrower, even zero tire deviation. Both profiles are respectively summed up using the superposition principle.

$$D(x) = \sum_{i=1}^{2} \sum_{j=1}^{J_i} \sum_{m=1}^{M_{ij}} \varepsilon_{ijm}(x) \quad \textbf{(2.5)}$$

where $i = 1, 2$ indicates single and dual tire load type respectively, j is the total number of tire load interval for i^{th} tire type, m is the number of tire repetitions in j^{th} tire load interval for i^{th} tire type. The maximum value of summed strain profiles for both ATs and HTs are compared as an indicator of performance impact. Since the strain profiles induced by AT are commonly more concentrated near the center of wheel-path due to narrower tire deviation, the summed $\varepsilon(x)$ profile ($D^{AT}(x)$) will be much higher compared with the one by HTs ($D^{HT}(x)$). The impact indicator I is calculated by comparing maximum values of $D(x)$ profile for ATs and HTs shown as follows,

$$I = \frac{\max\left(D^{AT}(x)\right)}{\max\left(D^{HT}(x)\right)} \tag{2.6}$$

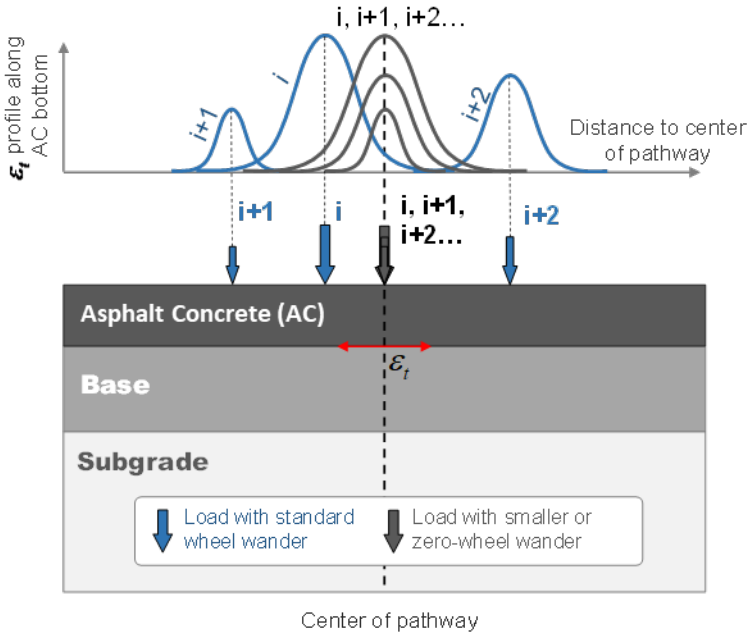

Figure 2.7 The driving force profiles (tensile strain at AC bottom) induced by each tire load with (pink curves) and without (dark grey curve) wheel wander.

2.4. Evaluation and Parametric Analysis of AT Impact on Texas Flexible Pavement

This section evaluates the impact of ATs based on the variations of tire deviation and the percentage of ATs driving on flexible pavements. The design of flexible pavements is based on various conditions and criteria such as specific service traffic volume, environmental condition, design reliability, roadbed resilient modulus, structural asphalt thickness, and mixture design, which covers a wide range of parametric variations. These different design features influence extensively and diversely on the AT effects on pavement performance. Thus, distress acceleration induced by AT would not be a uniform factor but is a case-dependent one that needs to be studied section by section.

The AT impact on twenty-two (22) Texas LTPP sections is analyzed in this section. Furthermore, a sensitivity analysis is carried out on the variations of mixture parameters and design features to exhibit how sensitive the pavement section is in response to the changes or the uncertainty of some of these parameters such as asphalt concrete thickness, and binder content, etc.

2.4.1. Assessment of AT Impact on Major Type of Flexible Pavement Distress

Following the evaluation procedure shown in Figure 2.6, the AT impact on major types of flexible pavement distress such as top-down cracking (TDC), bottom-up cracking (BUC), and rutting can be evaluated based on their corresponding driving force introduced by each tire load:

Table 2.5 Distress types and their corresponding driving force.

Distress type	Objective driving force
TDC	The tensile stress profile at pavement surface adjacent to tire load
BUC	The tensile strain profile at bottom of AC layer
rutting	The vertical strain profiles in AC, base, and subgrade layers, respectively

Since driving force profiles induced by ATs are more concentrated near the center of wheel-path due to smaller tire deviation, the accumulated profile by ATs is higher in magnitude and narrower in distribution compared with the profile by HTs. As illustrated in Figure 2.8, the twenty-year accumulated driving force for TDC, BUC, and rutting for Texas LTPP section 3689 are plotted respectively. These plots visualize the comparison of the shape of accumulated driving force profile and their maximum level that is used to quantify the AT impact indicator.

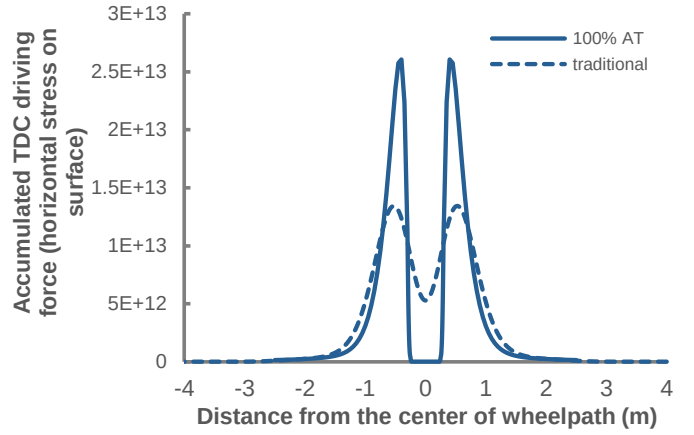

(a)

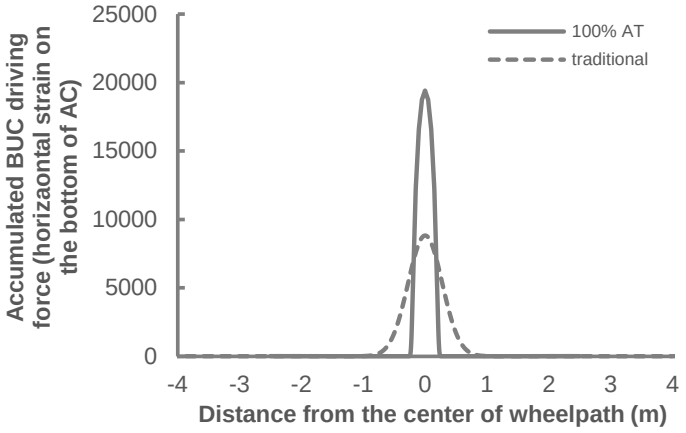

(b)

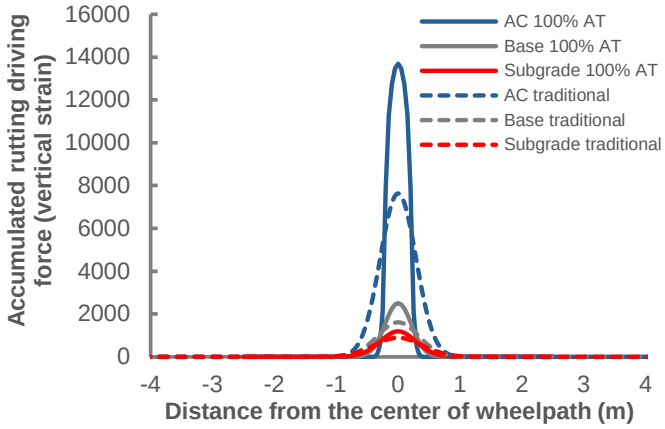

(c)

Figure 2.8 The plot of the typical accumulated driving force for (a) TDC, (b) BUC, and (c) rutting for Texas LTPP section 3689.

Figure 2.9 shows the impact indicators of ATs for BUC, TDC, and rutting respectively for twenty-two (22) Texas LTPP sections. The higher the impact indicator value, the more the pavement section suffer from AT impact. The blue and grey bars are the impact indicators of 100% and 50% ATs in service, which are plotted in descending order. The red connected dots are the AC thickness of each section exhibiting that the sections with thinner AC layer and lower AADTT are more affected by ATs (with higher impact factors and more on the left-hand side), while the sections with thicker AC layer and higher AADTT are less vulnerable to ATs (with lower impact factors and more on the right-hand side). Besides, the impact indicators on TDC are overall smaller than the ones for BUC. It could be explained that the driving force profile for BUC (horizontal strain at AC bottom) is more concentrated under the tire load, therefore, highly concentrated tire loads further intensify the accumulation of driving force. While the driving force profile of TDC is flatter, even with more concentrated tire loads, the level of accumulation of TDC is much lower than the one for BUC. Overall, the sections with higher traffic volume, higher reliability, and thicker AC layer are less affected by AT implementation for BUC and TDC.

Figure 2.9 (c)-(e) show the AT impact indicators of rutting in AC, base, and subgrade layers, respectively. These charts are plotted using the same scale showing that the relative magnitudes of the AT impact indicators gradually decrease from AC to subgrade. It is rational since the vertical stress and strain are gradually dispersed to become widespread with the increase of depth. As mentioned before, a less concentrated driving force results in lower impact by ATs. Therefore, the highest level of impact

indicator decreases from 1.99 in the AC layer to 1.69 in base, and 1.41 in the subgrade. The impact indicators for AC layer do not change much from section to section. No strong correlation is found between impact indicators and pavement features such as AADTT, AC, base, or subgrade layers for rutting in the AC layer. While for base and subgrade, the section with higher AADTT is less affected by ATs due to the fact that they are designed with higher reliability and are to serve higher traffic volume.

As shown in Figure 2.10, we run a cross-comparison of the AT impact with different AT standard deviations (0 inches, 2.5 inches, and 5 inches) and percentages of AT in service(25%, 50%, and 100%) for TDC, BUC, and rutting on Texas LTPP section 1039 that is a high AADTT and thick AC pavement section. With the development of AT technology and implementation, there would be more ATs on the flexible pavement in the near future, while the tire deviation would be intentionally adjusted by an advanced lane-keeping algorithm. The full spectrum analysis would benefit the AT design and pavement management for a specific pavement section with known potential impacts of different scenarios.

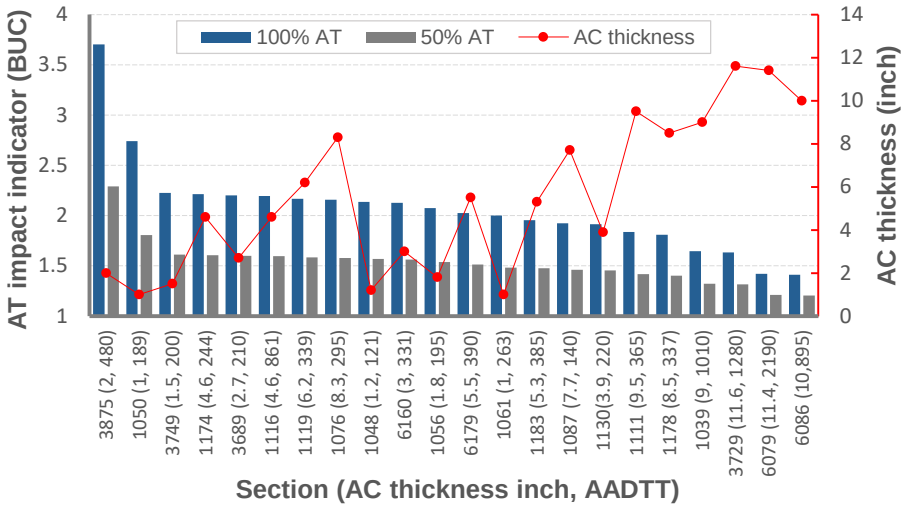

(a)

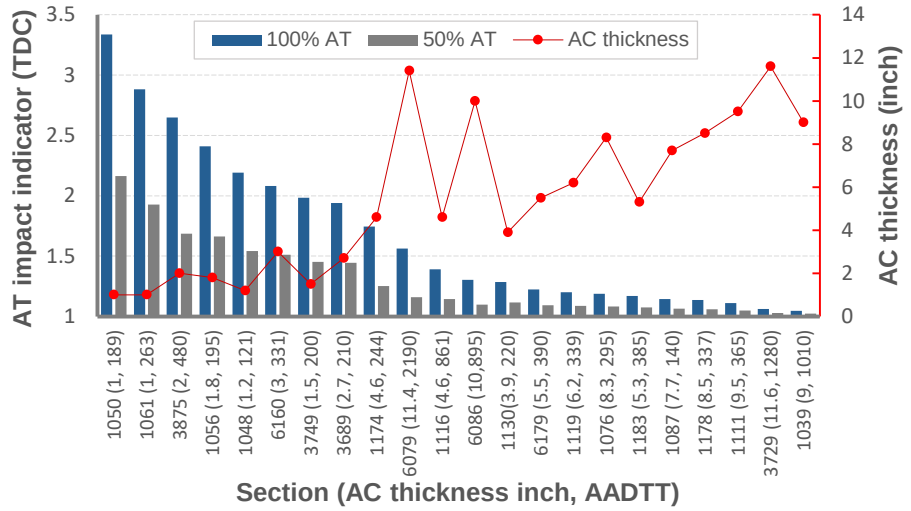

(b)

Figure 2.9 Impact factors of ATs (50% and 100% AT) for different distress: (a) BUC, (b) TDC, and (c) rutting: AC, (d) rutting: base, and (e) subgrade on twenty-two (22) Texas LTPP sections.

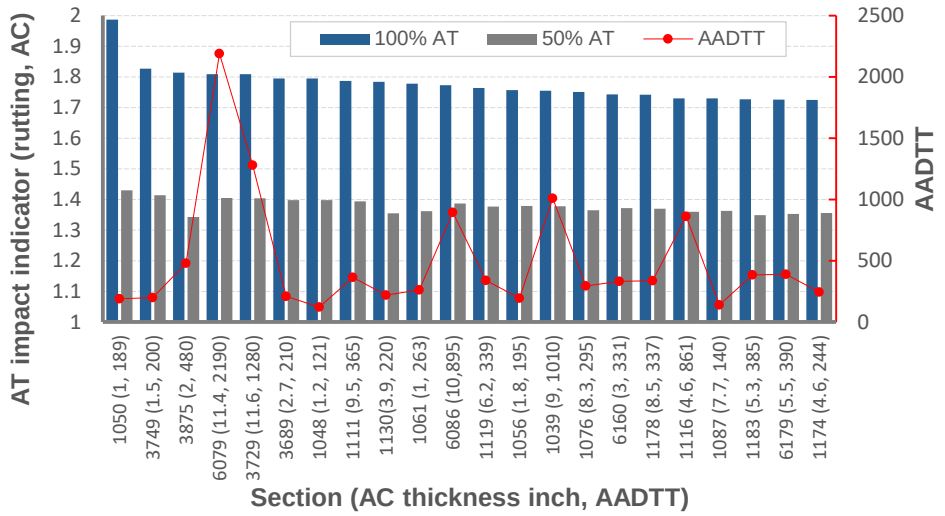

(c)

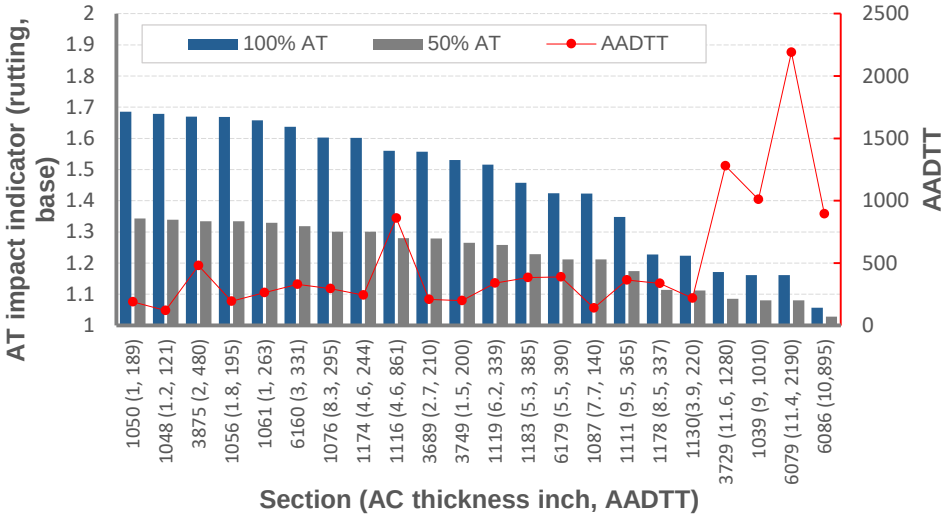

(d)

Figure 2.9 Impact factors of ATs (50% and 100% AT) for different distress: (a) BUC, (b) TDC, and (c) rutting: AC, (d) rutting: base, and (e) subgrade on twenty-two (22) Texas LTPP sections (cont'd).

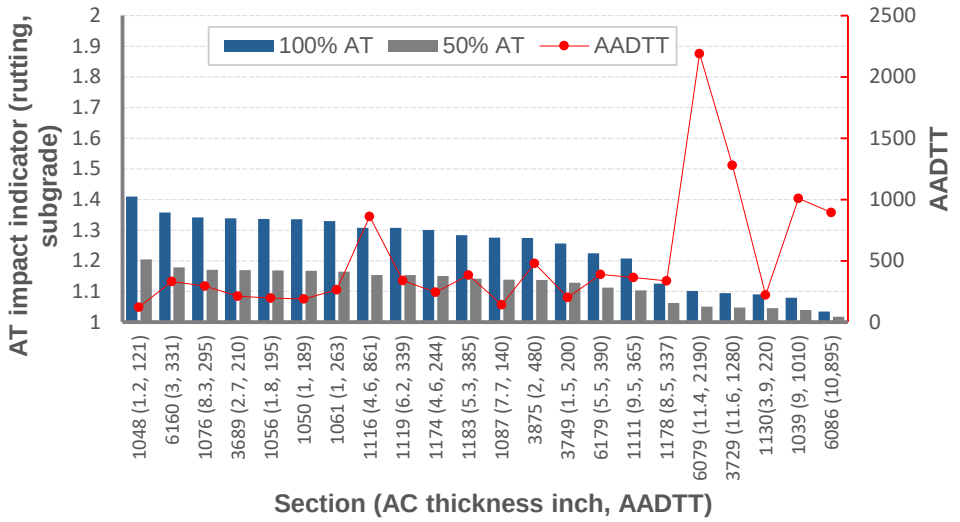

(e)

Figure 2.9 Impact factors of ATs (50% and 100% AT) for different distress: (a) BUC, (b) TDC, and (c) rutting: AC, (d) rutting: base, and (e) subgrade on twenty-two (22) Texas LTPP sections (cont'd).

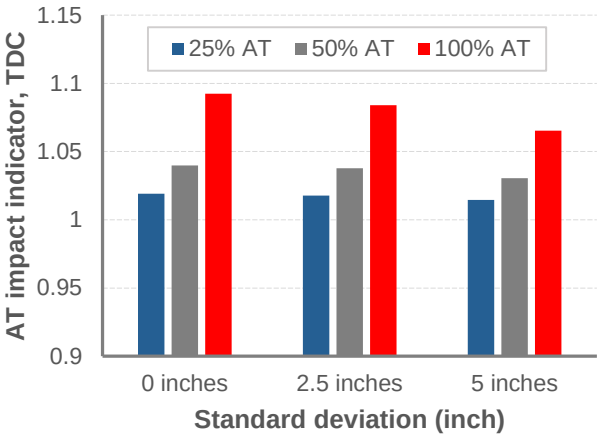

(a)

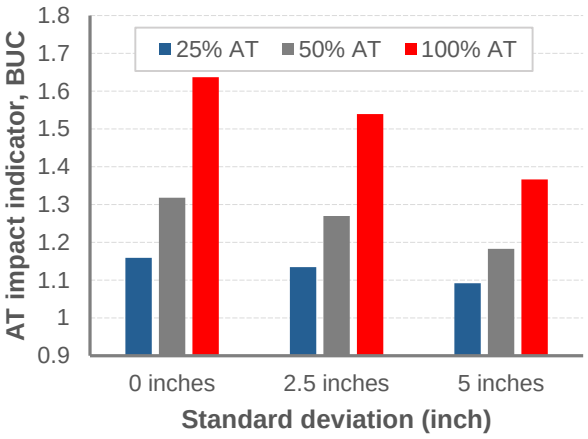

(b)

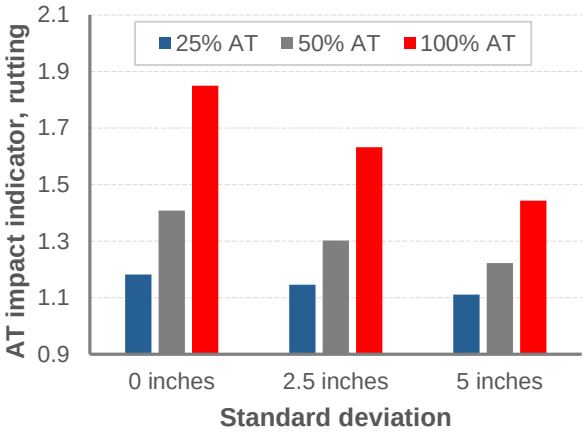

(c)

Figure 2.10 Cross comparison of the AT impact with different AT standard deviations and percentages of AT for (a) TDC, (b) BUC, and (c) rutting on Texas LTPP section 1039.

2.4.2. Parametric Analysis of Variations of Mixture Parameters

The design features of a flexible pavement vary upon specific conditions and criteria. A parametric study is necessary to identify those parameters in different pavement designs that have a significant influence on pavement performance in response to AT implementation. Two typical pavement sections, a high traffic volume section 1039 (1010 AADTT) and a low traffic section 1174 (244 AADTT), were selected for this purpose. The parametric study was conducted by varying one parameter at a time. The key parameters that may link to pavement vulnerability to ATs are listed in Table 2.6. The middle column of each section represents the actual design inputs value, while the left column is 70% of its original value and the right column is 130% of its original value, respectively. 30 simulations were undertaken for these two sections using the range of values specified in Table 2.6. The normalized error E_n between the varied and the original values is used to recognize the significance of each parameter on AT impact on pavement performance. The E_n is obtained by normalizing the error of impact indicators between the original parameters I_{original} and the varied parameters I_{varied}.

$$E_n = \frac{\left| I_{\text{varied}} - I_{\text{original}} \right|}{I_{\text{original}}} \cdot 100\% \qquad \textbf{(2.7)}$$

The overall normalized error of each parameter is the averaged E_n values of the minimum (70% of the original value) and maximum (130% of the original value) design parameters. The averaged E_n is utilized to quantify how much variation in AT impact will yield from changing certain input parameters within a certain range. In other words, it is to test how sensitive a pavement responds to ATs in terms of its performance.

Table 2.6 Selection of design parameters and range of values used for parametric analysis.

Parameter	Range of values section 1039 (high AADTT)			Range of values section 1174 (low AADTT)		
Thickness of AC, H_{AC}, inch	6.3	9	11.7	3.22	4.6	5.98
Thickness of base, H_{base}, inch	15.26	21.8	28.34	9.24	13.2	17.16
Dynamic modulus of AC, E_{AC}, ksi	$0.7E_{AC}$	Determined by material module	$1.3E_{AC}$	$0.7E_{AC}$	Determined by material module	$1.3E_{AC}$
Resilient modulus of base, E_{base}, ksi	89.33	127.61	165.89	175.90	251.28	326.66
Resilient modulus of subgrade, $E_{subgrade}$, ksi	38.67	55.24	71.81	61.16	87.37	113.58
Air void, V_{av}, %	4.42	6.32	8.21	9.24	13.2	17.16
Volume of effective asphalt binder, V_{be}, %	6.9	9.86	12.81	5.07	7.24	9.41

Figure 2.11 shows the normalized error of AT impact for each parameter. As shown in Figure 2.11(a), AC thickness has a significant influence on the AT impact for both low- and high-traffic sections in the TDC scenario. Other parameters in the high traffic volume section, such as the thickness H_{base} and the stiffness E_{base} of base, cause much fewer variations in the impact factor. For the low volume section, on the other hand, the overall level of E_n is much higher, in which the thickness of AC, the thickness and the stiffness of base, and the stiffness of subgrade are the highly influencing parameters that caused significant variation in the impact factor. For BUC shown in Figure 2.11(b), the thickness and modulus of AC are the top two influencing parameters for the high-volume section. While for the low-volume section, the parameters like the thickness of AC, the thickness and the stiffness of base are the significant influencing parameters on AT effect. These results indicate the thick AC layer in high volume section is generally less sensitive to the impact by ATs, and the parameters in the layers under AC are less

significant in resisting AT impact. The low volume section with thin AC layer is not only highly affected by AC thickness but also greatly impacted by the underlying materials and configurations since the mechanical support by base and subgrade is more crucial to this type of pavement. The parametric analysis for rutting is particularly interesting. Since rutting mainly occurs in the AC layer of pavement sections with thick AC layers, all the parameters related to AC have a significant influence on rutting caused by AT, such as thickness, dynamic modulus, air void, and effective asphalt binder content for AC layer. If pavement has a thin AC layer, rutting is most likely to occur in the underlying layers. Therefore, the thickness of the base layer and the modulus of base and subgrade layers can remarkably affect the rutting performance in response to ATs, which can be observed in Figure 2.11(c). Higher rutting is expected by AT when the pavement has a weak base and subgrade layers. The parametric analysis indicates the key parameters of pavement design that should be noticed when it comes to AT implementation.

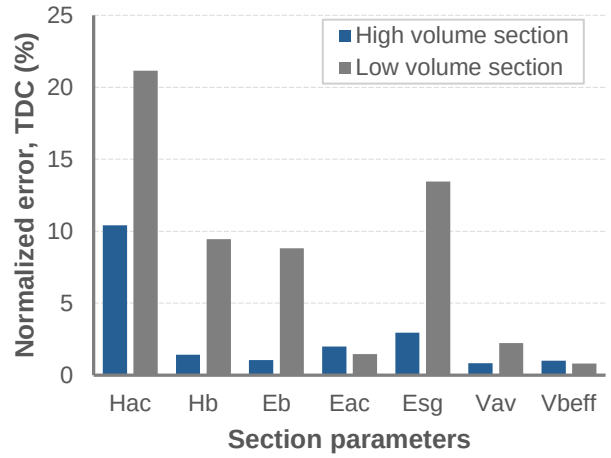

(a)

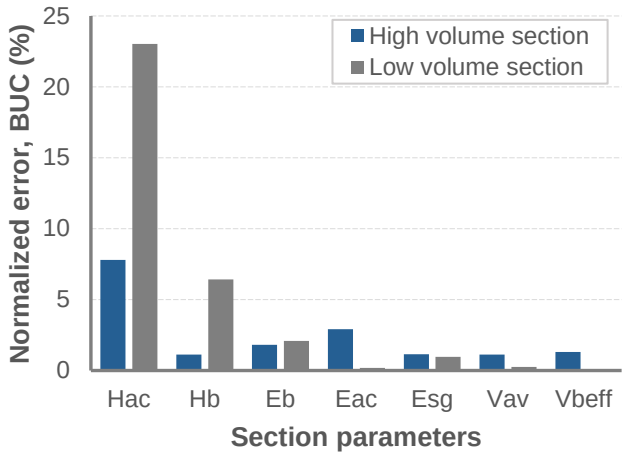

(b)

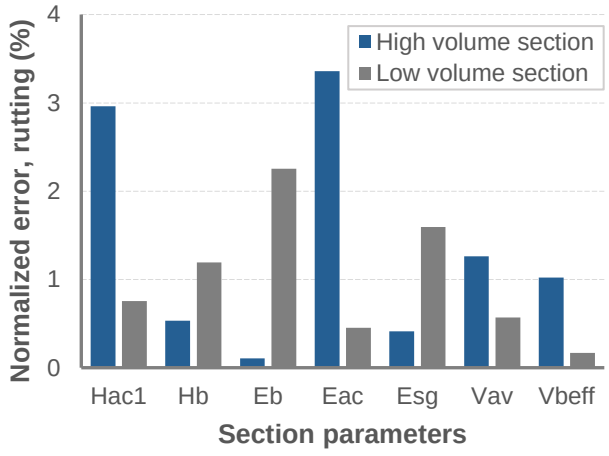

(c)

Figure 2.11 Parameter analysis of pavement design on AT impact for (a) TDC, (b) BUC, and (c) rutting for a high traffic volume section 1039 (1010 AADTT) and a low traffic volume section 1174 (244 AADTT).

2.4.3. Other Factors of ATs Under Development

Though the expectation of ATs is exceedingly positive, ATs still have a long journey before being commercially available and the narrative of their utilization remains unknown. Thus, the following facts cannot be determined at this stage:

- *ATs fleet proportion*: regardless of the fact that there are many insights and forecasts on the development of ATs, the actual extent of AT implementation remains uncertain and considerably related to a much bigger picture linked to technologies, efficiency, global economy, legislation, and even situation of COVID-19 pandemic (Laing 2022), etc.
- *Intensified loading frequency induced by platooned-autonomous truck:* The platooning of vehicles is a technology applied under AT umbrella that a group of vehicles closely follows a common leading vehicle on the highway. With the advent of computers and wireless communication devices equipped in these trucks, they can maintain close distances from each other to enhance fuel-efficiency, improve road capacity, etc. (Lu *et al.* 2017). Meanwhile, the platooning behavior can greatly shorten the resting time of flexible pavement between each axle load since the distance between trucks is much smaller than HTs. This phenomenon is not considered in this work but would make a flexible pavement more vulnerable if the resting time for recovery is shortened thus aggravating the accumulation of pavement distress.

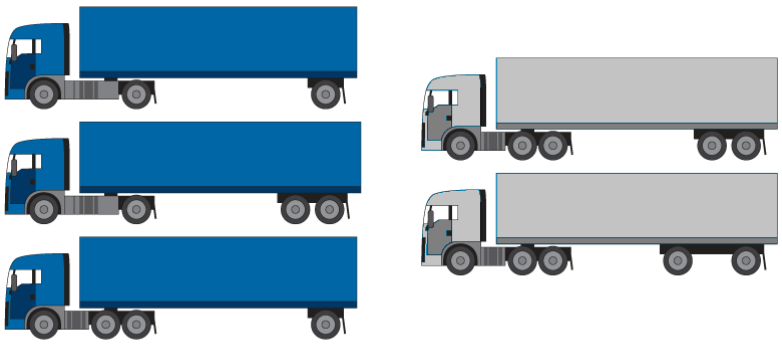

Figure 2.12 Typical AT types under Federal Highway Administration (FHWA) vehicle classification (Randall 2012).

- *Load spectra with AT operation*: the analyses presented in the previous sections are based on the load spectra obtained from historical traffic data by fully HTs. Implementation of ATs is a game-changer that would drastically reshape the load spectra curves of flexible pavement considering factors such as safety, operational cost efficiency, and related regulations in the future. Till now, the most common types of self-driving trucks under development are classes 8 and 9 under Federal Highway Administration (FHWA) vehicle classification shown in Figure 2.12. Most of the investment of ATs have been bet on the middle mile solution involving heavy duty class 8 trucks (Banker 2022). If these truck classes will be the majority of models in the future, the truck categories distribution shown from Table 2.1 - 2.4 and Figure 2.2 will be changed drastically and can no longer precisely describe actual traffic scenarios with ATs.
- *Lateral tire deviation of ATs*: Zhou et al.(Zhou *et al.* 2019) directly measured the patterns of AVs lateral tire deviation. It was found that the standard deviation of AVs

is at least 3 times smaller than human-driven vehicles. The narrower wheel wonder pattern is also measured by an AT technology company (Figure 2.13). Nevertheless, different lane-keeping algorithms utilized by ATs would yield various wheel wander patterns, which could even mimic the tire deviation pattern of HTs. Therefore, assuming a much narrower wheel wander may not always be accurate to describe the wheel wander pattern of ATs in the future.

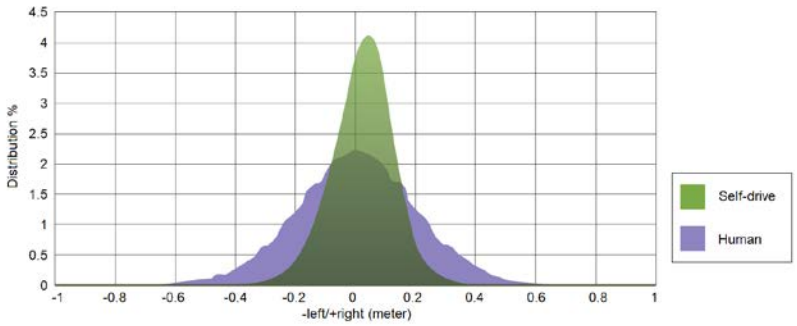

Figure 2.13 Tire deviation distributions of self-drive trucks and human-operated trucks (TuSimple 2023).

Summarily, the results of the current analysis may not precisely represent realistic scenarios in the future since the assumptions of ATs we made may be subject to many uncertainties mentioned above. These results, however, still provide rational insight into how AT operations may accelerate various types of distress in flexible pavement based on the current situation. Whenever more information on ATs implementation is available, one can easily utilize the same modeling procedure with the updated data for a more realistic evaluation.

2.5. Conclusions

Autonomous truck (AT) as a new category of vehicles has been making progressive steps towards commercially available. The expectation of ATs has shown exceptionally welcoming from the market perspective. Among many potential impacts, benefits, impediments, and technical aspects of ATs under extensive research, we focused on the potential impact of ATs on the performance of flexible pavement, more specifically, fatigue cracking and rutting performance. Since current infrastructure is designed to serve traditional traffic configurations, it is essential to study the impact of AT implementations on the long-term performance of existing pavement structures. The results of the analysis would benefit the future design of new pavements accommodating the coming AT.

Traffic variations for both ATs and HTs were elaborated. Loads of ATs are more concentrated in the center of wheel-path, which intuitionally leads to shorter pavement life, but the question is how to quantify the effect of ATs on distress development. Additionally, we adopted a hierarchical approach to characterize the normalized axle load distribution for each axle and vehicle type using historical WIM data. A new generalized framework was proposed that can evaluate the pavement response to ATs operation throughout its service life. The impact of AT was evaluated in a general way without employing any distress predictive models to avoid any bias induced by the choice of models. The impact indicator was introduced to quantify the AT impact. Twenty-two (22) Texas LTPP sections were chosen and analyzed. The findings are listed as follows:

(i) the AT impact on BUC is overall more significant than the ones for TDC.

(ii) the sections with higher traffic volume, higher reliability, and thicker AC layer are less vulnerable to AT implementation for both BUC and TDC.

(iii) the rutting impact indicators for the AC layer are higher than the ones in the base and subgrade.

(iv) Impact indicators of rutting in AC do not change much from section to section and no strong correlation was found between rutting impact indicators and any pavement features in the AC layer.

(v) for rutting in base and subgrade, the sections with higher AADTT are less affected by ATs due to that they are designed with higher reliability and a stronger AC layer.

A cross-comparison was presented to show the capacity of the present framework by running a full spectrum analysis covering different AT standard deviations and percentages of ATs. In addition, a parametric study was conducted to identify the sensitivity of the selected key parameters in response to AT implementation. The normalized error of AT impact of each parameter implied the sensitivity of certain parameters to AT loads:

For TDC,

(i) AC thickness has a significant influence on the AT impact for both low and high traffic sections;

(ii) for the high traffic volume section, the changes in base thickness and base stiffness caused much smaller variations of impact factor;

(iii) the parameters for the low traffic volume section are more sensitive to AT implementation;

(iv) for the low traffic volume section, the thickness of AC and base, the stiffness of base and subgrade are the highly influencing parameters that caused significant variation of performance impact.

For BUC,

(i) for the high-volume section, the thickness and modulus of AC are the top two influencing parameters;

(ii) for the low-volume section, the thickness of AC and base, and the stiffness of base are the significant influencing parameters on AT effect;

(iii) thick AC layers in the high-volume section generally insured higher performance under the impact of ATs and vice versa.

For rutting,

(i) for the high-volume section, rutting mainly occurs in the AC layer in pavement sections with thicker AC layers. All the parameters related to AC have a significant influence on rutting by AT, such as the thickness, dynamic modulus, air void, and effective asphalt binder content for the AC layer;

(ii) for a section with thin AC layers (or low traffic volume), rutting is most likely to occur in the underlying material. The thickness of the base layer, the modulus of the base and the subgrade layers can significantly affect the rutting behaviors in response to ATs.

Finally, since the narrative of ATs utilization remains unknown, our analysis may not precisely represent realistic scenarios in the future. The effect of intensified loading frequency induced by platooned-autonomous trucks was neglected in this work. We

described a few other facts of ATs that are to be determined. Nevertheless, the results provided some rational perception of how AT implementation may shorten the life of flexible pavement based on existing information. The same framework can be utilized for a better estimation when more data regarding AT is available.

3. A MECHANISTIC-EMPIRICAL MODEL FOR PREDICTING MOISTURE VARIATION IN SUBGRADE SOIL

3.1. Introduction

Moisture content of fined-grained subgrade soil is an important factor in pavement design because it directly affects the mechanical properties (i.e. resilient modulus), swell-shrink behavior of compacted subgrade soil (clay), and in turn the performance of pavements. Therefore, accurate prediction of moisture variation within subgrade soil is critical in pavement design.

Subgrade soil is compacted at optimal moisture content (OMC) under pavement construction to reach maximum dry density (MDD). Subgrade soil reaches moisture equilibrium condition several years after construction. The equilibrium moisture content at the depth of moisture active zone can be either larger or smaller than OMC depending on the suction potential in the subgrade soil at compaction (Bae and Stoffels 2019). After moisture equilibrium condition reaches, the moisture content above the depth of moisture active zone still fluctuates because of seasonal rainfall and evapotranspiration, while the moisture content below the active zone is barely affected by seasonal rainfall and evapotranspiration and keeps almost constant (McKeen and Johnson 1990). Previous studies show that the suction/moisture in subgrade soil is controlled by environmental factors (i.e. precipitation and evaporation) and material properties (Fredlund and Rahardjo 1993, Zapata *et al.* 2009, Bulut *et al.* 2014, Javid and Bulut 2019, Saha *et al.* 2019, Javid *et al.* 2022), while ground water has a minor effect unless the ground water table is close to the top of the subgrade layer (Bae and Stoffels 2019). Therefore, it is

necessary to consider both environmental factors and soil material properties to accurately predict moisture condition and suction distribution in subgrade soil, which is critical in predicting resilient modulus of subgrade soil in pavement design. Thornthwaite Moisture Index (TMI) is an indicator of local precipitation relative to the potential evapotranspiration. TMI has been correlated to equilibrium soil suction beneath pavements (Javid and Bulut 2019, Saha *et al.* 2019). There are many reported methods for calculating TMI since 1948. The first method of calculating TMI (TMI-1948) was empirically developed by Thornthwaite (Thornthwaite 1948) using limited climate data available during that period of time. In this method, TMI was defined as the annual moisture balance in a specified region based on precipitation, evaporation, water storage, deficit, and runoff. This method assumes that soil storage capacity is constant for all locations across the United States. The areas between isolines were interpolated. Thornthwaite and Mather (Thornthwaite and Mather 1955) revised the first method after they found that the implementation of the original method was difficult. This method is referred to as TMI-1955. There are only two parameters in the equation of TMI-1955, namely, annual precipitation and potential evapotranspiration of the site. Potential evapotranspiration is calculated using mean monthly temperature. Precipitation and air temperature data can be found from most weather stations around the world. Willmott and Feddema (Willmott and Feddema 1992) further revised TMI-1955 model by using a piecewise function in 1992. This method made a normalization of TMI-1955 model so that TMI ranges from -1 to +1, where -1 represents zero precipitation and +1 indicates zero potential evapotranspiration. Witczak (Witczak *et al.* 2006) found that the TMI-

1955 model provides TMI results significantly different from the results of TMI-1948, so he empirically adjusted TMI-1955 model so that the adjusted TMI-1955 (also called TMI-2006) closely matches TMI-1948 results. This method has been incorporated in the Enhanced Integrated Climate Model (EICM) for the Mechanistic-Empirical Pavement Design Guide (MEPDG) (ARA Inc. 2004). The input data for calculating TMIs across the United States can be found in the National Oceanic and Atmospheric Administration (NOAA) climate database.

As a component of the Mechanistic Empirical Pavement Design Guide (MEPDG), EICM is used to predict water and heat flow through pavement layers (Witczak *et al.* 2006). Groundwater table is the input for EICM in predicting moisture content and suction above the phreatic surface which could yield inaccurate predictions if the groundwater is far below the subgrade layer (Zapata *et al.* 2009). To accurately predict moisture condition and suction distribution in subgrade soil, Gay (Gay 1994) first established a functional relationship between TMI and the mean annual moisture depth. Saha et al. (Saha *et al.* 2019) adopted Gay's work and developed a mechanistic-empirical model to predict equilibrium suction for subgrade soil by considering both climate and soil properties. TMI-2006 (Witczak *et al.* 2006) was used to represent the climate effect in this model. However, Saha et al. model (Saha *et al.* 2019) is incapable of characterizing suction variation above the depth of moisture active zone due to the climate condition, soil drainage, and vegetation cover on site. Suction variations at any depths and time within the subgrade soil can be determined by solving Mitchell's one-dimensional diffusion equation (Mitchell 1979). Based on Mitchell's approach, McKeen

and Johnson (McKeen and Johnson 1990) proposed a model to determine the depth of moisture active zone and diffusion coefficient of subgrade soil given field suction measurements. Yue and Veenstra (Yue and Veenstra 2018) employed the McKeen and Johnson's model to estimate the diffusion coefficient and moisture active zone in Oklahoma using the data collected Oklahoma Mesonet (weather station). Javid et al. (Javid and Bulut 2019) collected field measured suction data from the same data source (Oklahoma Mesonet), and back-calculated equilibrium soil suction by fitting the field suction data into Mitchell's diffusion equation. A statistical model was established to estimate equilibrium suction as a function of relative humidity, clay content, and TMI. Such a statistical model was developed based on the data collected at a specific site in Oklahoma under a specific climate and soil conditions, which limits the usage in other regions with different field conditions. To avoid the limitations of statistical approach, a mechanistic-empirical approach is ideal to model moisture/suction variation within subgrade soil.

The objective of this study is to develop a mechanistic-empirical model to predict moisture variation in fine-grained subgrade soil based on a modified mechanistic-empirical equilibrium suction prediction model (Saha *et al.* 2019) and Mitchell's one-dimensional diffusion equation (Mitchell 1979). The modification to Saha's equilibrium suction model is the incorporation of a new TMI model. This paper is organized as follows. The next section describes the data collection and processing which will be used in model calibration and validation. Then a new Thornthwaite Moisture Index (TMI) prediction model is introduced and the predicted TMI is used to represent the climate

factor in the prediction of the equilibrium soil suction at the depth of moisture active zone as described in the following section. Next, the predicted equilibrium soil suction at the depth of moisture active zone is input into Mitchell's diffusion equation to predict the soil suction with time and depth within the subgrade layer of pavements. The last two sections conduct model validation and summarizes the significant findings of this study.

3.2. Data Collection and Processing

The data used in this paper were collected from two sources: MnROAD and LTPP databases (LTPP InfoPave 2020). MnROAD is a pavement test track operated by the Minnesota Department of Transportation. As shown in Figure 3.1, MnROAD consists of three main road segments: a 3.5 mile I-94 original Westbound, a 3.5 mile I-94 Mainline, and a 2.5 mile Low Volume Road (LVR), which are divided into over 50 sections with different materials and pavement types.

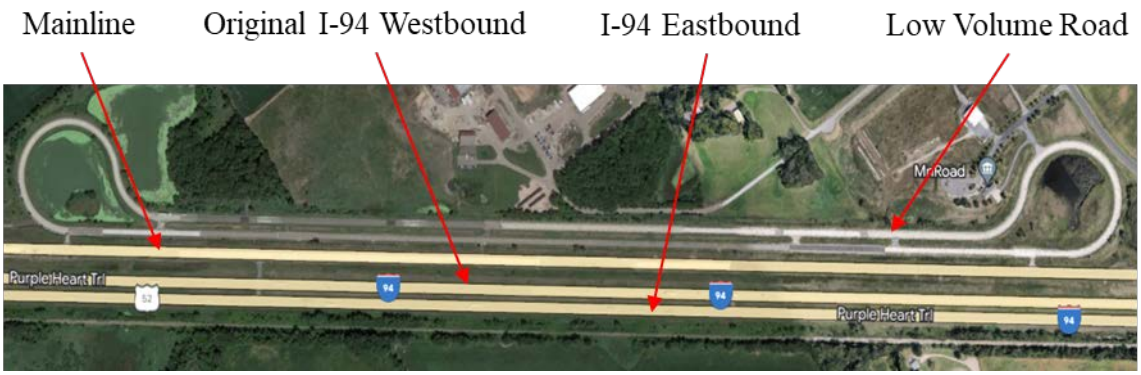

Figure 3.1 MnROAD map (map data: Google Earth).

More than 1000 electronic sensors have been installed at MnROAD test sections since 1993 to track the changes in pavement performance due to environmental change and dynamic loading.

Initially, the senor model used to monitor moisture variation in subsurface layers was time domain reflectometry (TDR) and then was replaced with Decagon EH_2O-TE (since 2007) and EH_2O-5TE (since 2008).

The moisture data collected by EH_2O-TE and EH_2O-5TE sensors were used in this paper. EH_2O-TE and EH_2O-5TE were installed in the base and subgrade layers at different depths and the output includes volumetric water content (VWC), electrical conductivity (EC), and temperature (T_c). Campbell Scientific data loggers (CR 1000) and multiplexors were used to automatically collect the sensors' measurements every 15 minutes. With a material specific calibration, a precision of ±2% can be achieved using the recommended calibration method provided by Decagon. MnROAD staff developed a calibration approach for the base/subbase and subgrade materials used at MnROAD based on the Decagon's method and the calibration functions are summarized in Table 3.1. The MnROAD materials are classified according to aggregate gradation (grain size distribution), as presented in Figure 3.2.

The collected raw data were converted to VWC using the calibration functions determined in the laboratory as shown below:

$$VWC\% = a \cdot EW + b \quad \textbf{(3.1)}$$

where *a* and *b* for different paving materials can be found in Table 3.1.

A data screening criteria developed in a previous study (Teshale *et al.* 2019) was employed here to ensure that high quality data were selected and used to validate the proposed model. The details of the screening criteria can be found in (Teshale *et al.* 2019). After the data screening, cell 17, 19 and 35 were selected and the VWC data for

the selected cells were further smoothed out using the exponential weighted moving average (EMA) with a span of seven days. An example of the comparison between VWC and its EMA can be found in Figure 3.8 and 3.10 in section 3.4 of this chapter. A LTPP pavement section (ALABAMA 01-0102) with measured moisture content within the subgrade layer was also selected with no data screening process because there was only one data point with the date and depth of the measurement. The pavement configurations, paving materials and sensor locations (only the sensors in subgrade layers are marked in red balls) for cell 17, 19, 35, and LTPP 01-0102 are presented in Figure 3.3. Cell 17 contains three sensors within the subgrade layer at the depths of 48, 60, and 72 inches from pavement surface. Cell 19 contains two sensors within the subgrade soil at the depths of 60 and 72 inches. Cell 35 contains six sensors within the subgrade soil at depths of 20.04, 24, 36, 48, 60, and 72 inches. LTPP 01-0102 contains only one sensor within the subgrade soil at 17.18 inches depth.

Table 3.1 Material properties and coefficients of the calibration function for TE and 5TE (Teshale et al. 2019).

Material	Proctor parameters		TE** sensor calibration coefficients		5TE** sensor calibration coefficients	
	MDD (g/cm^3)	OMC (%)	a	b	a	b
class3	2.05	9.4	0.0009	-0.5149	0.0004	-0.0481
class5	2.108	7.4	0.0007	-0.3524	0.0003	-0.0239
class6	2.062	6.8	0.0011	-0.6787	0.0006	-0.1438
SG*	2.111	7.8	0.0011	-0.6615	0.0005	-0.0908
clay	1.875	13.1	0.0009	-0.4693	0.0003	-0.0021

** Select Granular, crusher-run material meeting MnDOT requirements. ** Decagon ECH_2O sensors (two types: TE and 5TE)*

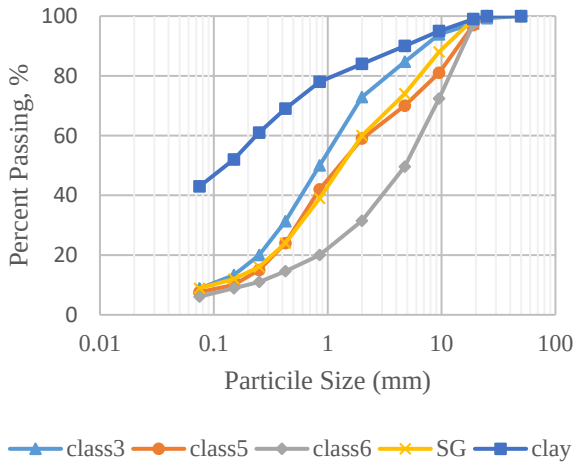

Figure 3.2 Classification of MnROAD materials.

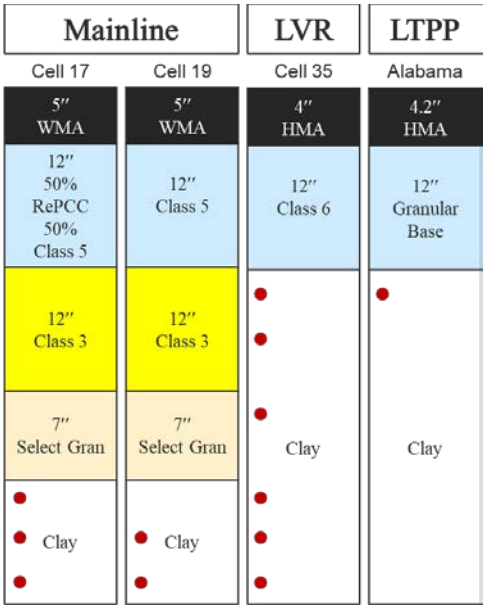

Figure 3.3 Schematic representation of pavement sections with sensor locations.

3.3. Model Development

3.3.1. Thornthwaite Moisture Index

Three TMI models were reviewed in the introduction of this paper. This study introduces a new TMI model developed by McKeen (unpublished) based on prior research (Mather 1974, McKeen and Johnson 1990). An average of at least 20 consecutive years' TMI is recommended to represent the long-term effect of climate on the soil moisture.

Below is the step-by-step procedure (Mather 1974, McKeen and Johnson 1990) to determine TMI.

Step 1. Collect input data including coordinates (Latitude and Longitude), monthly precipitation $p(i)$, and air temperature t_i.

Step 2. Determine soil initial moisture S_0 and maximum moisture storage S_{max} at the starting time of calculation. The default S_0 and S_{max} are set to be 0.48 and 20.32, respectively.

Step 3. Determine monthly heat index, $h(i)$, annual heat index for the year y, $H(y)$, and Thornthwaite's coefficient a ranging from 0 to 4.25 using Eqn. (3.2 - 3.4).

$$h(i) = \left[0.2 \cdot t(i)\right]^{1.514} \tag{3.2}$$

$$H(y) = \sum_{1}^{12} h(i) \tag{3.3}$$

$$a = H(y)^3 \cdot 6.75 \cdot 10^{-7} - H(y)^2 \cdot 7.71 \cdot 10^{-5} + H(y) \cdot 1.792 \cdot 10^{-2} + 0.49239 \tag{3.4}$$

Step 4. Determine the unadjusted monthly potential evaporation $e(i)$ using Eq. (3.5).

$$e(i) = 1.6 \cdot \left[\frac{10 \cdot t(i)}{H(y)}\right]^a \tag{3.5}$$

Step 5. Determine monthly adjusted potential evapotranspiration, $e'(i)$, by multiplying $e(i)$ by the day-length corrections $D(i)$ based on the latitude of the site that can be found in Table 3.2 ; determine the annual potential evapotranspiration, $PE(y)$, by summing the $e'(i)$ for a year.

$$e'(i) = \frac{e(i) \cdot D(i) \cdot N(i)}{30} \tag{3.6}$$

where $N(i)$ is number of days in each month.

$$PE(y) = \sum_{1}^{12} e'(i) \tag{3.7}$$

Table 3.2 Day Length correction factors (McKeen and Johnson 1990).

Degree North Lattitude / Month	0	5	10	15	20	25	26	27	28	30	31	32	33	34	35	36	37	38	39	40	41	42	43	44	45	46	47	48	49	50
Jan	1.04	1.02	1.00	0.97	0.95	0.93	0.92	0.92	0.91	0.91	0.90	0.90	0.89	0.88	0.88	0.87	0.86	0.85	0.85	0.84	0.83	0.82	0.81	0.81	0.80	0.79	0.77	0.76	0.75	0.74
Feb	0.94	0.93	0.91	0.91	0.90	0.89	0.88	0.88	0.88	0.87	0.87	0.87	0.86	0.86	0.85	0.85	0.84	0.84	0.84	0.83	0.83	0.83	0.82	0.82	0.81	0.81	0.80	0.80	0.79	0.78
Mar	1.04	1.03	1.03	1.03	1.03	1.03	1.03	1.03	1.03	1.03	1.03	1.03	1.03	1.03	1.03	1.03	1.03	1.03	1.03	1.03	1.03	1.03	1.02	1.02	1.02	1.02	1.02	1.02	1.02	1.02
Apr	1.01	1.02	1.03	1.04	1.05	1.06	1.06	1.07	1.07	1.07	1.08	1.08	1.08	1.09	1.09	1.10	1.10	1.10	1.11	1.11	1.11	1.12	1.12	1.13	1.13	1.13	1.14	1.14	1.14	1.15
May	1.04	1.06	1.08	1.11	1.13	1.15	1.15	1.16	1.16	1.17	1.18	1.18	1.19	1.19	1.20	1.21	1.22	1.23	1.23	1.24	1.25	1.26	1.26	1.27	1.28	1.29	1.30	1.31	1.32	1.33
Jun	1.01	1.03	1.06	1.08	1.11	1.14	1.15	1.15	1.16	1.16	1.17	1.18	1.19	1.20	1.20	1.22	1.23	1.24	1.24	1.25	1.26	1.27	1.28	1.29	1.29	1.31	1.32	1.33	1.34	1.36
Jul	1.04	1.06	1.08	1.12	1.14	1.17	1.17	1.18	1.18	1.19	1.20	1.20	1.21	1.22	1.22	1.24	1.25	1.25	1.26	1.27	1.27	1.28	1.29	1.30	1.31	1.32	1.33	1.34	1.35	1.37
Aug	1.04	1.05	1.07	1.08	1.11	1.12	1.12	1.13	1.13	1.13	1.14	1.14	1.15	1.15	1.16	1.16	1.17	1.17	1.18	1.18	1.19	1.19	1.20	1.20	1.21	1.22	1.22	1.23	1.24	1.25
Sep	1.01	1.01	1.02	1.02	1.02	1.02	1.02	1.02	1.02	1.03	1.03	1.03	1.03	1.03	1.03	1.03	1.03	1.04	1.04	1.04	1.04	1.04	1.04	1.04	1.04	1.04	1.04	1.05	1.05	1.06
Oct	1.04	1.03	1.02	1.01	1.00	0.99	0.99	0.99	0.98	0.98	0.98	0.98	0.98	0.97	0.97	0.97	0.97	0.96	0.96	0.96	0.96	0.95	0.95	0.95	0.94	0.94	0.93	0.93	0.93	0.92
Nov	1.01	0.99	0.98	0.95	0.93	0.91	0.91	0.90	0.90	0.90	0.89	0.89	0.88	0.88	0.87	0.86	0.85	0.84	0.84	0.83	0.82	0.82	0.81	0.80	0.79	0.79	0.78	0.77	0.76	0.73
Dec	1.04	1.02	0.99	0.97	0.94	0.91	0.91	0.90	0.90	0.89	0.88	0.88	0.87	0.86	0.86	0.84	0.83	0.83	0.82	0.81	0.80	0.79	0.77	0.76	0.75	0.74	0.73	0.72	0.71	0.70
Degree South Lattitude / Month	**0**	**5**	**10**	**15**	**20**	**25**	**26**	**27**	**28**	**30**	**31**	**32**	**33**	**34**	**35**	**36**	**37**	**38**	**39**	**40**	**41**	**42**	**43**	**44**	**45**	**46**	**47**	**48**	**49**	**50**
Jan		1.06	1.08	1.12	1.14	1.17				1.20					1.23					1.27		1.28		1.30		1.32		1.34		1.37
Feb		0.95	0.97	0.98	1.00	1.01				1.03					1.04					1.06		1.07		1.08		1.10		1.11		1.12
Mar		1.04	1.05	1.05	1.05	1.05				1.06					1.06					1.07		1.07		1.07		1.07		1.08		1.08
Apr		1.00	0.99	0.98	0.97	0.96				0.95					0.94					0.93		0.92		0.92		0.91		0.90		0.89
May		1.02	1.01	0.98	0.96	0.94				0.92					0.89					0.86		0.85		0.83		0.82		0.80		0.77
Jun		0.99	0.96	0.94	0.91	0.88				0.85					0.82					0.78		0.76		0.74		0.72		0.70		0.67
Jul		1.02	1.00	0.97	0.95	0.93				0.90					0.87					0.84		0.82		0.81		0.79		0.76		0.74
Aug		1.03	1.01	1.00	0.99	0.98				0.96					0.94					0.92		0.92		0.91		0.90		0.89		0.88
Sep		1.00	1.00	1.00	1.00	1.00				1.00					1.00					1.00		1.00		0.99		0.99		0.99		0.99
Oct		1.05	1.06	1.07	1.08	1.10				1.12					1.15					1.15		1.16		1.17		1.17		1.18		1.19
Nov		1.03	1.05	1.07	1.09	1.11				1.14					1.20					1.20		1.22		1.23		1.25		1.27		1.29
Dec		1.06	1.10	1.12	1.15	1.18				1.21					1.29					1.29		1.31		1.33		1.35		1.37		1.41

Step 6. Determine the monthly change of moisture, $\Delta m(i)$, initial amount of storage in each month, $Str(i)$, monthly change of storage, $\Delta Str(i)$, final storage at the end of each month, $STR(i)$, and the monthly change in deficit, $\Delta d(i)$ using Eqn. (3.8 – 3.12).

$$\Delta m(i) = p(i) - e'(i) \tag{3.8}$$

$$Str(i) = \begin{cases} S0 + \Delta m(1) & \text{if } i = 1 \\ STR(i-1) + \Delta m(i) & \text{if } i \geq 2 \end{cases} \tag{3.9}$$

$$\Delta Str(i) = \begin{cases} \{Str(i) & \text{if } Str(i) < S_{\max} \\ S_{\max} & \text{if } Str(i) \geq S_{\max} \end{cases} \tag{3.10}$$

$$STR(i) = \begin{cases} \Delta \text{Str(i)} & \text{if } \Delta Str(i) > 0 \\ 0 & \text{if } \Delta Str(i) \leq 0 \end{cases} \tag{3.11}$$

$$\Delta d(i) = \begin{cases} 0 & \text{if } \Delta m(i) > 0 \\ \Delta m(i) + STR(i) & \text{if } \Delta m(i) \leq 0 \end{cases} \tag{3.12}$$

Step 7. Compute monthly deficit, $DEF(i)$, and runoff, $RUN(i)$ using Eqn. (3.13 – 3.14).

$$DEF(i) = \begin{cases} 0 & \text{if } \Delta d(i) > 0 \\ -\Delta d(i) & \text{if } \Delta d(i) \leq 0 \end{cases} \tag{3.13}$$

$$RUN(i) = \begin{cases} Str(i) - S_{\max} & \text{if } Str(i) > S_{\max} \\ 0 & \text{if } Str(i) \le S_{\max} \end{cases} \quad \textbf{(3.14)}$$

Step 8. Compute annual deficit (sum of monthly deficit), *DEF*(*y*), and annual runoff (sum of monthly runoff), *RUN*(*y*) using Eqn. (3.15 – 3.16).

$$DEF(y) = \sum_{1}^{12} DEF(i) \quad \textbf{(3.15)}$$

$$RUN(y) = \sum_{1}^{12} RUN(i) \quad \textbf{(3.16)}$$

Step 9. Determine the Thornthwaite Moisture Index (TMI) for year *y* using Eqn. (3.17).

$$TMI = \frac{100 \cdot RUN(y) - 60 \cdot DEF(y)}{PE(y)} \quad \textbf{(3.17)}$$

Step 10. Repeat the procedure to calculate the TMIs for the next consecutive19 years. The moisture storage in the end of each year is used as the initial moisture storage in the beginning of the next year. The average of 20 years' TMI can be used as a climate factor in residential foundation design.

3.3.2. Equilibrium Soil Suction

This study employed Saha's model (Saha *et al.* 2019) to predict the equilibrium soil suction at the depth of moisture active zone with the TMI calculated using the procedure reported in section 3.3.1. The details are summarized in the following sub-sections including the calculations of depth of moisture active zone (Z_m), Maximum available annual moisture depth (d_{am}), diffusivity coefficient (α), mean annual moisture (d_m), and finally the equilibrium soil suction (u_e).

3.3.2.1. Depth of Moisture Active Zone (Z_m)

The depth of moisture active zone is defined as the least soil depth above which changes in water content and soil heave may occur because of change in environmental conditions after construction (Fattah and Salman 2006). The presence of vegetation significantly affects the depth of moisture active zone and surface suction. The average Z_m in non-vegetation and full vegetation areas were estimated to be 9.39 ft. (286.2 cm) and 21 ft. (640.1 cm), respectively according to Lytton (Lytton 1997) and FPA (FPA 2017). Therefore, to calculate Z_m, the fraction of vegetation cover (F_r) is first calculated using Brunsell and Gillies' method (Brunsell and Gillies 2003) as expressed in Eqn. (3.18). Then, the Z_m is determined by interpolation between 286.2 cm and 640.1 cm corresponding to bare soil and soil with full vegetation as shown in Eqn. (3.19).

$$F_r = \left(\frac{NDVI - NDVI_0}{NDVI_{max} - NDVI_0} \right)^2 \quad \textbf{(3.18)}$$

$$Z_m = 286.2 + (640.1 - 286.2) \cdot F_r \quad \textbf{(3.19)}$$

where $NDVI_0$ and $NDVI_{max}$ are set to be -2000 and 10000 to represent bare and full vegetation soils, respectively; Normalized Difference Vegetation Index (NDVI) data covering the United States can be downloaded from NOAA Climate Data Records (CDR).

3.3.2.2. Maximum Available Annual Moisture Depth (d_{am})

The maximum available annual moisture depth is defined as the moisture lost during the transition from wet to dry state of soil above the depth of moisture active zone. As

shown in Figure 3.4, d_{am} can be expressed as the area between the moisture profiles under wet and dry conditions.

$$d_{am} = \int_0^{Z_m} \left[\theta_{wet}(z) - \theta_{dry}(z) \right]$$

$$d_{am} = \frac{\theta_{wet} - \theta_{dry}}{\sqrt{\frac{n\pi}{\alpha}}} \left(e^{-\sqrt{\frac{n\pi}{\alpha}} Z_m} - 1 \right) \quad \textbf{(3.20)}$$

where θ_{wet} and θ_{dry} are the volumetric water contents at top surface under wet (suction is assumed to be 4.5 or 5.7 pF) and dry conditions (suction is assumed to be3 pF), respectively according to Saha et al. (Saha *et al.* 2019); θ'_{wet} and θ'_{dry} are the volumetric water contents at the depth of moisture active zone under wet and dry conditions, respectively; θ'_{dry} is calculated from u'_{dry} using the SWCC ANN model (Saha *et al.* 2018a); u'_{dry} is the suction at the depth of moisture active zone under dry condition calculated using Eqn. (3.21) when equilibrium suction (u_e) is assumed to be 3; n is the number of cycles of wetting and drying during a year; α is unsaturated diffusivity of subgrade soil which will be explained in the next section.

$$u(z) = u_e + u_0 \cdot \exp(-\sqrt{\frac{n\pi}{\alpha}} z) \quad \textbf{(3.21)}$$

where $u(z)$ is the suction at the depth z; u_e is equilibrium suction; u_0 is suction profile amplitude.

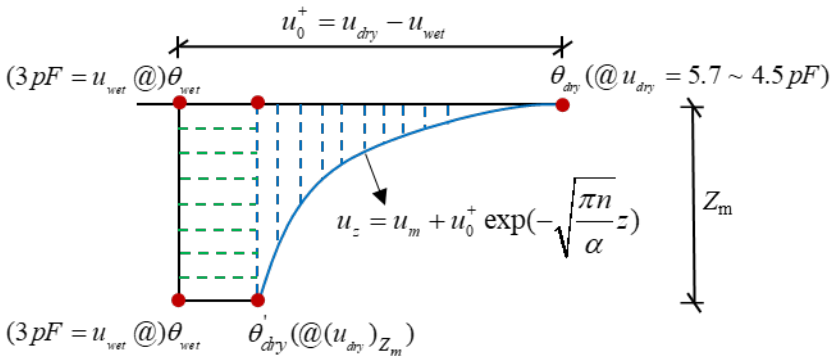

Figure 3.4 Schematic of maximum available annual moisture depth (d_{am}) (Saha et al. 2019).

To obtain the moisture profile under dry state, a one-dimensional diffusion equation proposed by Mitchell (Mitchell 1979) is used to predict the suction profile with depth. Then the calculated suction profile is converted into moisture profile using a previously developed SWCC artificial neural network (ANN) model (Saha *et al.* 2018a). Mitchell's diffusion equation model will be introduced in the next section. The Fredlund-Xing SWCC model (Fredlund and Xing 1994) as shown in Eqn. (3. 22 - 3.23) is used to correlate soil moisture content and suction. The SWCC ANN model is used to predict the coefficients of the Fredlund-Xing SWCC model.

$$\theta_w = C(h) \cdot \left[\frac{\theta_{sat}}{\left\{ \ln\left[e + \left(\frac{h}{c_f} \right)^{b_f} \right] \right\}^{c_f}} \right] \quad \textbf{(3.22)}$$

$$C(h) = 1 - \frac{\ln(1+\frac{h}{h_r})}{\ln\left[1+\frac{1.021\times10^{7}}{h_r}\right]} \quad \textbf{(3.23)}$$

where h is soil matric suction; a_f, b_f, c_f and h_r are model parameters predicted by the SWCC ANN model.

3.3.2.3. Diffusivity coefficient

Diffusivity coefficient (α) controls how fast the surface moisture infiltrates into soil mass. Diffusivity coefficient can be measured in either the laboratory, or calibrated using Mitchell's diffusion equation with field suction measurements, or estimated using empirical models. The most accurate way of determining diffusivity coefficient that represents the field condition is by monitoring the suction variation at the surface and depth over which moisture changes seasonally; then use Mitchell's diffusion equation to fit the field data to backcalculate field diffusivity coefficient. McKeen and Johnson (McKeen and Johnson 1990) reported that the backcalculated diffusivity coefficients for Dallas/Fort Worth (FDW) region using Mitchell's diffusion equation were much larger than the laboratory values which implies that laboratory values might not be representative to the field condition. However, field suction data is not always available. The slope of the SWCC reflects the soil response to suction changes and it was believed this parameter is correlated with diffusion coefficient (McKeen and Johnson 1990). Lytton (Lytton 1994) proposed an equation that correlated the slope of SWCC with diffusion coefficient as shown in Eqn. (3.24).

$$\alpha = |S|\, p\gamma_w / \gamma_d \quad \textbf{(3.24)}$$

where $|S|$ is slope of the SWCC at 80% of saturated volumetric water content; γ_d is dry unit weight of soil; γ_w is unit weight of water; p is unsaturated permeability and $p = |h_0| k_0 / 0.434$; k_0 is saturated permeability of soil that was collected from the Natural Resource Conservation Service (NRCS) database; h_0 is the soil suction at which the soil saturates.

3.3.2.4. Mean Annual Moisture Depth (d_m)

The mean annual moisture depth (d_m) is defined as the moisture depth (volume) under equilibrium condition. The mean annual moisture depth is dependent on both soil properties and climate factors. TMI is representative to climate factors because it is an indicator of annual moisture balance by considering precipitation and potential evapotranspiration. Saha et al. (Saha *et al.* 2019) adopted Gay' approach (Gay 1994) to estimate the mean annual moisture depth as a function of TMI (= T - 65) and the maximum available annual moisture depth, which is expressed as:

$$d_m = \frac{d_{am}}{[1 + \frac{d_{am} - d_1}{d_1 (\frac{T}{T_1})^{\gamma}}]} \quad \textbf{(3.25)}$$

$$\gamma = 0.0369 * d_{am} \quad \textbf{(3.26)}$$

$$d_1 = 0.269 * d_{am} \quad \textbf{(3.27)}$$

$$T_1 = 0.8418 * d_{am} \quad \textbf{(3.28)}$$

By replacing d_{am} and θ_e with d_m and θ_{wet}, respectively in Eqn. (3.20), the equilibrium moisture content (θ_e) at the depth of moisture active zone is calculated using Eqn.

(3.29). A schematic illustration of mean annual moisture depth (d_m) is shown in Figure 3.5.

$$d_m = \frac{\theta_e - \theta_{dry}}{\sqrt{\frac{n\pi}{\alpha}}}\left(e^{-\sqrt{\frac{n\pi}{\alpha}}Z_m} - 1\right) \quad \textbf{(3.29)}$$

The equilibrium moisture content (θ_e) at the depth of moisture active zone is converted into equilibrium soil suction by using the developed SWCC ANN model (Saha *et al.* 2018a).

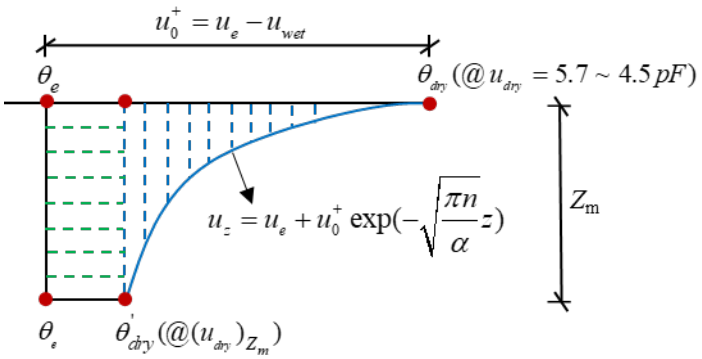

Figure 3.5. Schematic of mean annual moisture depth (d_m) (Saha et al. 2019).

3.3.3. Prediction of Subgrade Soil Moisture Variation with Time and Depth

Soil moisture varies at the surface due to climate, drainage and vegetation cover (Mitchell 1979). According to Mitchell (Mitchell 1979, Javid and Bulut 2019), the effect of climate variation on the moisture flow and then the seasonal movement of clayey subgrade can be characterized by solving a diffusion equation (Eqn. (3.30)) and boundary conditions (Eqns. (3.31 – 3.32)) given below:

$$\frac{\partial u}{\partial t} = \alpha \frac{\partial^2 u}{\partial z^2} \quad \textbf{(3.30)}$$

$$u(0,t) = \frac{U_0}{2} + U_1 \cdot \cos(n2\pi t) + U_2 \cdot \cos(2n2\pi t) + ...etc \quad \textbf{(3.31)}$$

$$u(z,t) \to 0 \text{ as } z \to \infty \quad \textbf{(3.32)}$$

where $u(0,t)$ is an arbitrary state of surface suction according to the site specific climate (precipitation and evapotranspiration); *z* is depth; *t* is time; α is diffusivity coefficient; *n* is the number of cycles of wetting and drying during a year; U0/2 is equilibrium soil suction in pF; and U_i is Fourier Series coefficients.

The solution of the diffusion equation is:

$$\begin{aligned} u(z,t) = \frac{U_0}{2} + U_1 \cdot \exp(-z\sqrt{\frac{n\pi}{\alpha}}) \cdot cos(n2\pi t - z\sqrt{\frac{n\pi}{\alpha}}) + \\ U_2 \cdot \exp(-z\sqrt{\frac{2n\pi}{\alpha}}) \cdot \cos(2n2\pi t - z\sqrt{\frac{2n\pi}{\alpha}}) + ...etc \end{aligned} \quad \textbf{(3.33)}$$

where the Fourier Coefficients U_i is determined by

$$U_i = \frac{2}{P}\int_0^P u(0,t) \cdot \cos(\frac{i\pi t}{P})dt, \; i = 0,1,2,... \quad \textbf{(3.34)}$$

where P=1/2n.

When the surface suction is averaged every month and expressed as S1, S2, …, S12, the Fourier coefficients of Eqn. (3.34) can be rewritten as

$$U_i = \frac{2}{12}\left[\int_0^1 S_1 \cdot \cos(\frac{i\pi t}{12})dt + \int_1^2 S_2 \cdot \cos(\frac{i\pi t}{12})dt + ... + \int_{11}^{12} S_{12} \cdot \cos(\frac{i\pi t}{12})dt\right] \quad \textbf{(3.35)}$$

Figure 3.6 shows the flow chart for predicting soil suction within subgrade soil using the proposed framework.

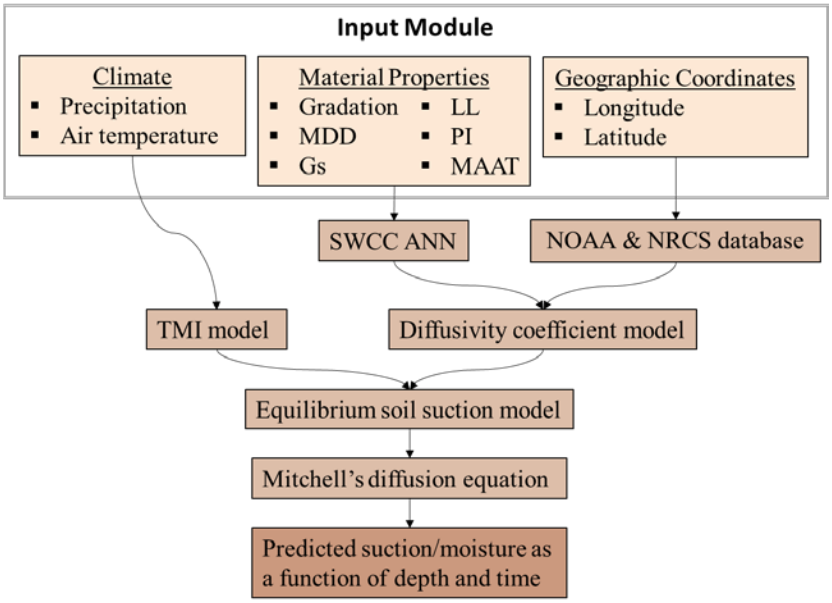

Figure 3.6 Flow chart for predicting soil suction (moisture) within subgrade soil.

3.4. Model Validation

3.4.1. Validation of New TMI Model

In this study, the modification to Saha's equilibrium suction model (Saha *et al.* 2019) is the incorporation of a new TMI model (Mather 1974, McKeen and Johnson 1990). To validate the new TMI model, this section compares the new TMI model with TMI-2006 model using the precipitation and air temperature data collected from 5852 weather stations across the United States (Saha *et al.* 2019). As shown in Figure 3.7, the predicted TMIs using the new TMI model are in good agreement with the predictions of TMI-2006 model with R^2 value of 0.93.

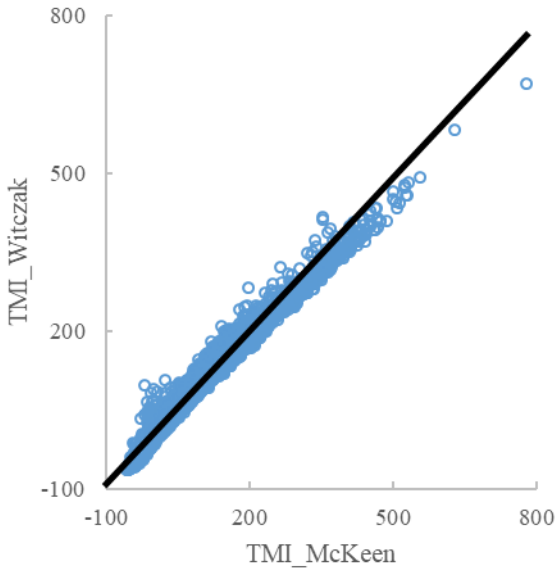

Figure 3.7 Comparison between TMI-2006 model (Witczak et al. 2006) and new TMI model.

3.4.2. Validation of Modified Equilibrium Soil Suction Model

This section validates the updated equilibrium soil suction model by comparing predicted equilibrium soil suction with field measurements. The VWC data along with pavement configuration and paving material properties from 3 MnROAD sections and 1 LTPP section (Figure 3.3) were collected to calibrate and validate the proposed framework. Since each section has multiple sensors installed within the subgrade layer, only one sensor from each section is used in model calibration and the rest of them are used in model validation. Specifically, the raw moisture data collected from MnROAD database is first converted into volumetric water content (VWC) using the calibration functions shown in Table 3.1. The converted VWC data is then smoothed out using the exponential weighted moving average (EMA) with a span of seven days, which are used to calculate suction in pF through the previously developed SWCC artificial neural

network (ANN) model (Saha *et al.* 2018a). Finally, the equilibrium soil suction and diffusivity coefficient are calibrated by fitting the calculated suction data into Mitchell's diffusion equation (Mitchell 1979, Javid and Bulut 2019).

As shown in Figure 3.3, Cell 17 has 3 sensors installed in the subgrade layer, cell 19 has two, cell 35 has 6, and LTTP 0102 has 1. The selected sensors for calibration are C17-207, C19-208, C35-204, and S-LTPP for cell 17, 19, 35, and LTPP 0102, respectively. Figure 3.8 compares the measured and predicted VWC using Mitchell's diffusion equation using calibrated equilibrium soil suction and diffusivity coefficient for each section. The time limit of measured VWC data is different from sensor to sensor because some sensors failed prematurely or the data collected were of poor quality. Notice that the VWC predictions repeat each year whereas the measured VWC are different to some degree in each year. This is because we assumed the precipitation and evaporation variation the same each year to simplify the computation complexity and the first year's climate data were used as input in predicting VWC, while the actual precipitation and evaporation varies slightly from year to year. This explains why the model predictions agree well with the field measurements in the first year, while it is not always the case when the weather conditions change significantly in the subsequent years.

The equilibrium soil suction in each pavement section was determined after we calibrated Mitchell's diffusion equation. Figure 3.9 compares the calibrated and predicted equilibrium soil suctions for four pavement sections with the average deviation of 0.1 pF.

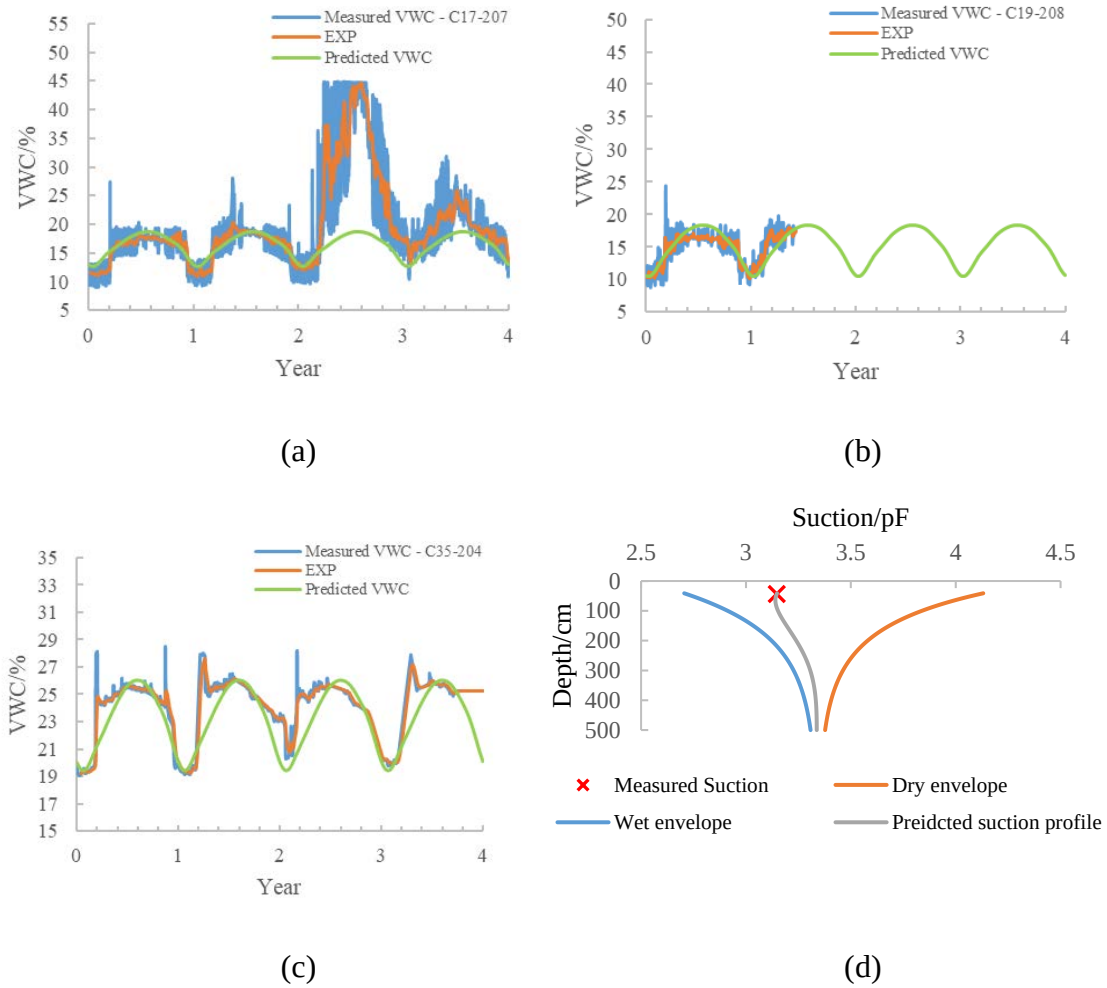

Figure 3.8 Comparison between measured and predicted VWC using calibrated model parameters (a) Cell 17 (b) Cell 19 (c) Cell 35 (d) LTPP-0102.

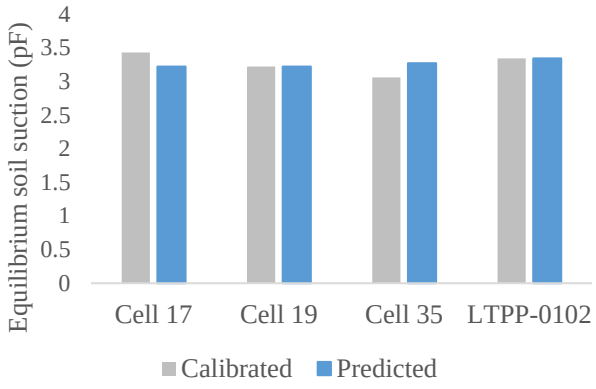

Figure 3.9 Comparison between predicted and calibrated equilibrium soil suction.

3.4.3. Validation of Mitchell's Diffusion Equation

The previous section determined equilibrium soil suction and diffusivity coefficient using the data collected by 1 selected sensor at a specific depth within the subgrade layer in each pavement section. In this section, the rest of sensors are used to evaluate the performance of Mitchell's diffusion equation using the calibrated equilibrium soil suctions and diffusivity coefficients.

Figure 3.10 (a-b) compares the model predictions with the field measured VWC at depths of 48 (sensor C17-206) and 72 (sensor C17-208) inches, respectively, for Cell 17. The calibrated model parameters were determined through sensor C17-207. Figure 3.10 (c) compares the model predictions with the field measured VWC at depths of 60 (sensor C19-207) inches for Cell 19. The calibrated model parameters were determined through sensor C19-208. Figure 3.10 (d-h) compares the model predictions with the field measured VWC at depths of 20.04 (sensor C35-203), 36 (sensor C35-205), 48 (sensor C35-206), 60 (sensor C35-207), and 72 (sensor C35-208) inches, respectively, for Cell 35. The calibrated model parameters were determined through sensor C35-204. The LTPP section is not presented here because only 1 sensor was installed in the subgrade layer.

A reasonable agreement was found between model predictions and field measurements. In Figure 3.10 (d), the under-prediction of the moisture variation near the top of the subgrade layer (sensor C35-203) could possibly be due to the existence of micro cracks that changed the soil water characteristic curve for the upper subgrade soil so that this region is able to retain more water than the lower region in the subgrade soil. The

oscillation of measured VWC in Figure 3.10 (h) is very significant possibly due to sensor malfunctioning but the averages of measured and predicted VWC are close to each other (23.1% vs. 21.5%). As mentioned before, Decagon EH2O-TE and EH2O-5TE measure VWC with a precision of ±2% if a material specific calibration is performed. Therefore, a possible reason that caused the error is from the field measurements. What's more, the diffusivity coefficient plays an important role in suction and moisture prediction as shown in Eqn. (3.33). The diffusivity coefficient changes with depth and has a positive correlation with the volumetric water content in the soil (Bai et al. 2007). Therefore, incorporation of the diffusivity coefficient as a function of depth and volumetric content in the Mitchell's diffusivity equation should be considered in further studies.

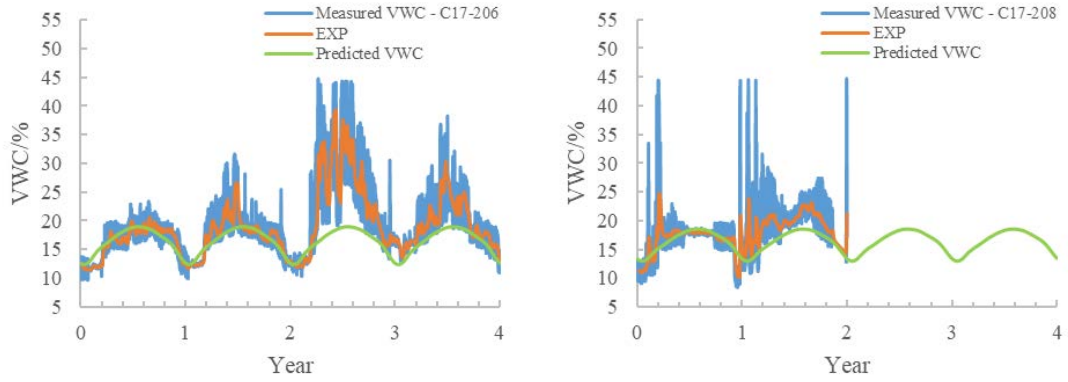

(a) (b)

Figure 3.10 Comparison between measured and predicted VWC using calibrated model parameters for other sensors.

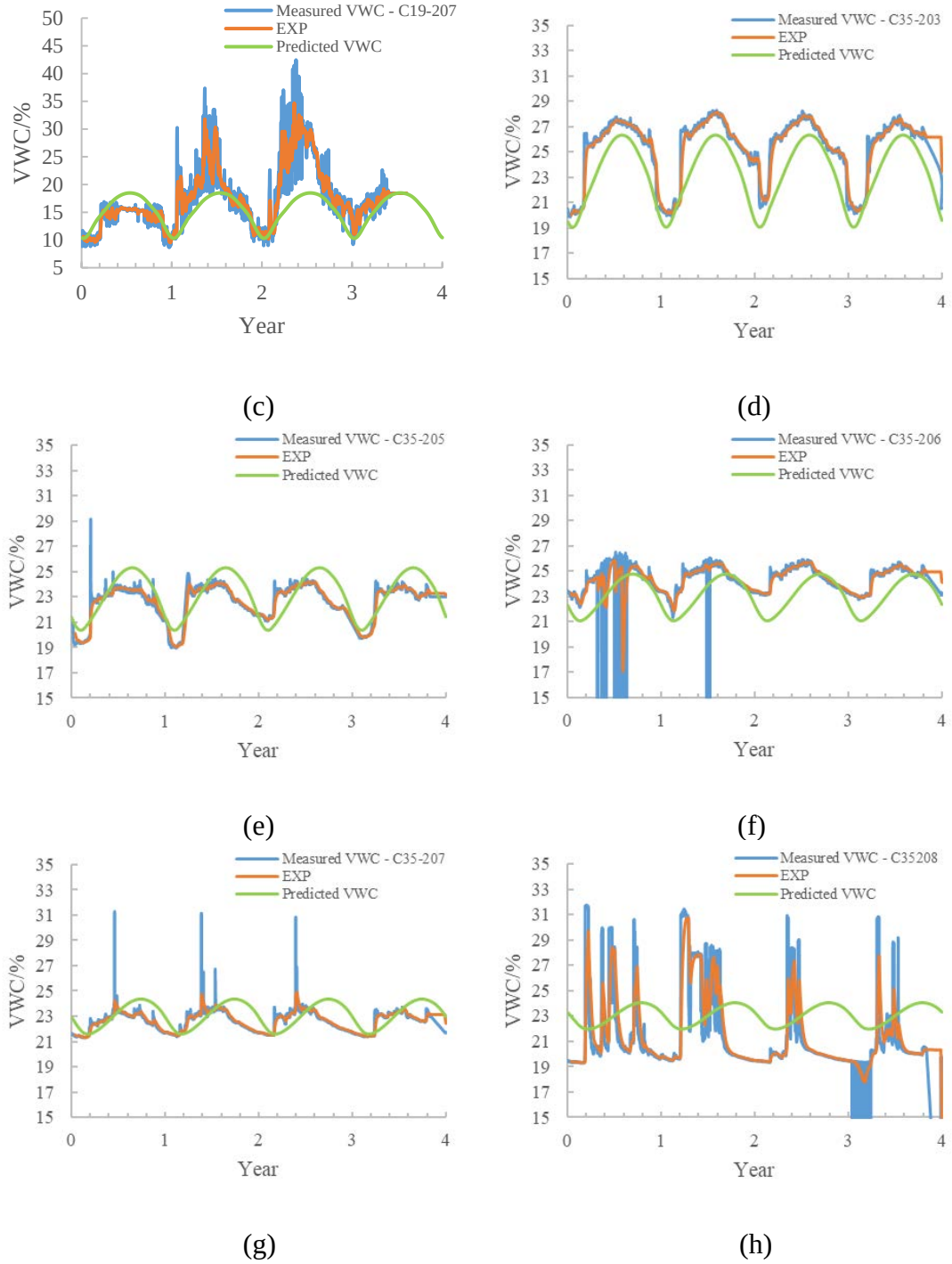

Figure 3.10 Comparison between measured and predicted VWC using calibrated model parameters for other sensors (cont'd).

According to Figure 3.11, the proposed framework is capable of characterizing a clear seasonal pattern in VWC due to the climate factors including precipitation, evaporation and runoff. What's more, both the predicted and measured amplitude of moisture variation decrease as depth goes deeper in the subgrade layer (Figure 3.12). The same phenomenon was also found in Yue's study (Yue and Veenstra 2018).

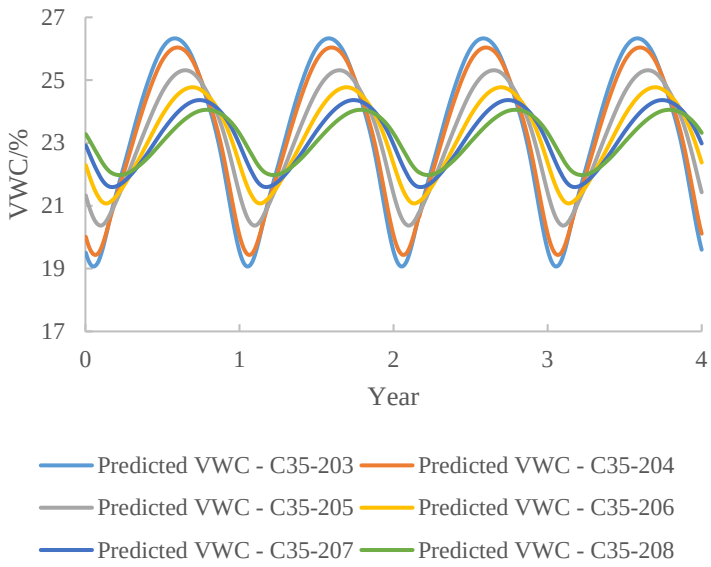

Figure 3.11 Comparisons of predicted volumetric water content (VWC) at different depths in the subgrade soil in cell 35.

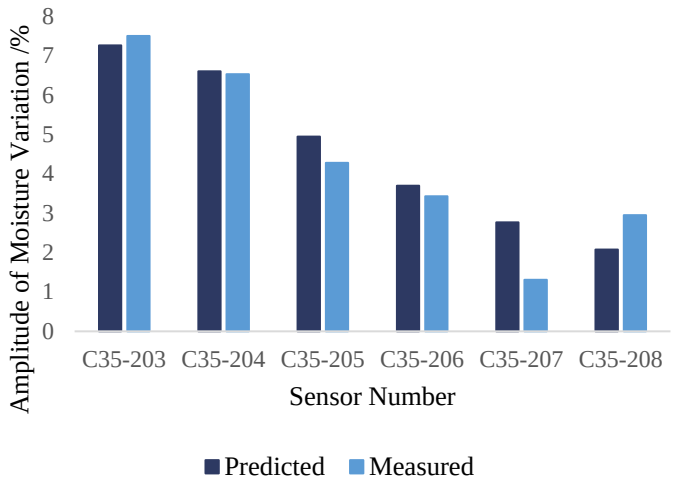

Figure 3.12 Comparison between predicted and measured amplitude of volumetric water content (VWC) in cell 35.

3.5. Conclusion

Subgrade soil under pavement structure is usually unsaturated, and moisture content in subgrade soil directly affect material properties (i.e. resilient modulus) and thereby pavement performance. Therefore, this study proposed a mechanistic-empirical model for predicting moisture variation in subgrade Soil by coupling a modified ME-based equilibrium soil suction model and Mitchell's diffusion equation. The major findings and conclusions are as follows.

- A new TMI model was introduced and validated by comparing with TMI-2006 using the climate data collected from 5852 weather stations across the United States. A statistical analysis was performed and it was found that the predicted TMI using the proposed TMI model matches well with the predicted results using TMI-2006 model with coefficient of determination of 0.93.

- A previously developed equilibrium soil suction model was improved by incorporating with a new TMI model. The modified equilibrium soil suction model was validated using the moisture data from 3 MnROAD pavement sections and 1 LTPP section. It was found that the average deviation of predicted equilibrium soil suction from calibrated counterparts was 0.1 pF.
- We finally proposed a ME-based soil moisture prediction model by coupling the modified equilibrium soil suction model to Mitchell's diffusion equation. The proposed moisture prediction model was validated using the moisture data collected by 9 sensors at different depths in the subgrade soil.
- The proposed moisture prediction model is capable of characterizing a clear seasonal pattern in VWC due to climate factors including precipitation, evaporation and runoff.
- Both the measured and predicted moisture wave amplitude decreased as depth gets closer to the depth of moisture active zone, which is consistent with Yue's study (Yue and Veenstra 2018).
- In future studies, diffusivity coefficient should be considered as a function of depth and volumetric water content in Mitchell's diffusivity equation. What's more, the actual precipitation and evaporation data for each year will be used instead of assuming the same pattern each year to better reflect the climate effect on moisture condition in subgrade soil.
- The accurate prediction of the resilient moduli of unbound base and subgrade soil is crucial in pavement design. It is believed that the resilient moduli of unbound base

and subgrade soil are the stress and moisture dependent. The next paper will focus on the prediction of resilient modulus profile within subgrade soil with consideration of stress dependency and moisture sensitivity.

4. BACKCALCULATION OF RESILIENT MODULUS OF FINE-GRAINED SUBGRADE SOIL FROM FALLING WEIGHT DEFLECTIONS

4.1. Introduction

Fine-grained subgrade soil, used as the foundation of asphalt pavements, directly contributes to the overall stiffness and performance of pavement system. Fatigue cracking and rutting in asphalt pavements are associated with resilient strain and permanent deformation within the subgrade layer (Brown and Selig 1991, Brown 1996, Puppala *et al.* 1999). Therefore, stiffness of subgrade soil is important in pavement design and analysis.

The response of unbound aggregate base and fine-grained subgrade soil tend to shake down to be resilient (elastic) under repeated traffic load. Resilient modulus (M_R), defined as the ratio of deviator stress to axial resilient strain (Seed *et al.* 1962), is commonly used to represent stiffness of unbound base and subgrade soil in pavement design. Previous studies have shown that the resilient response of both unbound aggregate base and fine-grained subgrade soil exhibits nonlinear stress-dependency (Seed *et al.* 1967, Thompson and Robnett 1979, Moossazadeh and Witczak 1981, Witczak and Uzan 1988, ARA Inc. 2004, Peng *et al.* 2020) and moisture-dependency (Lytton 1996, Drumm *et al.* 1997, ARA Inc. 2004, Khoury and Zaman 2004, Liang *et al.* 2008, Salour and Erlingsson 2013, Peng *et al.* 2020) under repeated traffic loads. Therefore, the resilient modulus distribution within unbound aggregate base and fine-grained subgrade layers should be a function of stress state and moisture content, which is different from a single value used in layered linear elastic solution. Some studies also showed that resilient

modulus of subgrade soil was affected by relative compaction (Zhang *et al.* 2021) and soil physical properties (i.e. passing the #200 sieve, maximum dry density, optimum moisture content, Atterberg limits) (George 2004).

Repeated load triaxial test (RLT) is commonly used to determine the resilient modulus of unbound base and subgrade soil, and evaluate the risk of shear force induced premature rutting of asphalt pavements. In RLT, fifteen combinations of varying confining and deviator stresses are imposed on soil specimens, and resilient modulus is measured for each load condition. However, the RLT data are not always available for the studied pavement sections, and performing RLT is time consuming and requires well-trained personnel.

In order to predict M_R instead of performing RLT, numerous resilient modulus models have been proposed to capture the stress- and/or moisture dependent behavior of unbound base and subgrade soil. NCHRP 1-53 summarized 28 resilient modulus models for unbound base and subgrade materials which can be categorized into stress-dependent model, stress-moisture-dependent model, stress-moisture-dependent and cross-anisotropic model, and empirical regression model.

General-purpose finite-element programs have been used for decades to analyze the layered pavement system with user-defined geo-material models for characterizing the nonlinearity of unbound base and/or fine-grained subgrade soil. ILLI-PAVE (Raad and Figueroa 1980) and GT-PAVE (Tutumluer 1995) are two famous FE-based programs that take into account the stress-dependent resilient modulus of unbound base and subgrade soil. In ILLI-PAVE, K-θ model (Seed *et al.* 1967) was used in unbound

granular base material to characterize its stress hardening behavior, and bilinear model (Thompson and Robnett 1979) was used in fine-grain subgrade soil to characterize its stress softening behavior. The failure of base and subgrade soil was governed by Mohr-Coulomb theory. Uzan model (Uzan 1985) and UT-Austin model (Pezo 1993) are available in GT-PAVE to characterize the stress dependent behavior of unbound granular base material. However, both of the aforementioned programs didn't consider moisture effect on the resilient modulus distribution in unbound materials.

More recently, more and more general-purpose FE programs are available to be used in pavement response analysis (i.e. ABAQUS, ADINA, ANASYS, and COMSOL Multiphysics). Kim et al. (Kim *et al.* 2009) programmed three stress-dependent resilient modulus models including Uzan model (Uzan 1985), universal octahedral shear stress model (Witczak and Uzan 1988) and bilinear model (Thompson and Robnett 1979) in a user material subroutine (UMAT) in the FM program ABAQUS to characterize stress-hardening behavior of unbound granular materials (the first two models) and stress-softening behavior of fine-grained subgrade soil (the last model). Erlingsson and Ahmed (Erlingsson and Ahmed 2013) proposed an elastic response program for layered asphalt pavements based on Burmister MLET theory. The universal constitutive model (extended K-θ model) (ARA 2004), currently used by MEPDG was incorporated into the program to characterize the stress dependency of unbound materials. The drawback of Uzan model (Uzan 1985), universal octahedral shear stress model (Witczak and Uzan 1988) and bilinear model (Thompson and Robnett 1979), and extended K-θ model

(ARA 2004) is that the moisture effect was not considered which is very important in determining the resilient modulus of unbound material.

Gu et al. (Gu *et al.* 2016) implemented Lytton model (Lytton 1996) into ABAQUS by developing a new user defined material subroutine (UMAT) in ABAQUS to characterize the stress and moisture dependency of resilient modulus in unbound granular base material. Cross-anisotropy was also considered in unbound base material. Later on, Zhang et al. (Zhang *et al.* 2018) developed a coupled nonlinear cross-anisotropic elastoplastic (NAEP) constitutive model for unbound granular base layer of pavement. The model was implemented into COMSOL Program by using weak form partial differential equation (PDE) module. However, all of the material models used in above FE analysis were calibrated through RLT or regression models which might not be able to capture the in-situ conditions (Karasahin *et al.* 1993). This is because compaction variability of the soil specimen in the field and lab might change the inherent soil structure.

To reflect the field condition, field-based data (i.e. FWD data) should be used in the determination of model parameters. Growing efforts (Hoffman and Thompson 1982, Ceylan *et al.* 2005, Ahmed *et al.* 2016, Varma and Emin Kutay 2016, Li and Wang 2019) have been made to backcalculate nonlinear material properties of unbound base and fine-grained subgrade soil using deflection basin data measured by falling weight deflector (FWD). So far, the material models for unbound base and fine-grained subgrade soil that have been considered in current backcalculation programs are linear elastic, nonlinear elastic (stress dependent). Taking account of the moisture effect on

unbound granular base and/or fine-grained subgrade soil has not been reported in currently available backcalculation programs yet. The authors developed a mechanistic-empirical model to predict moisture variation within subgrade soil by coupling a mechanistic-empirical based equilibrium suction prediction model (Saha *et al.* 2019) to Mitchell's diffusion equation (Mitchell 1979), which has the potential to be incorporated into a backcalculation program.

The objective of this study was to develop a FWD-based backcalculation program that considers moisture- and stress-dependent resilient modulus for fine-grained subgrade soil. To achieve this objective, a new moisture prediction model was incorporated into a forward pavement response program developed in COMSOL Multphysics to simulate the pavement response of FWD dropping weight. Bound Optimization by Quadratic Approximation (BOBYQA) method (Powell 2009) was used in the backcalculation procedure to backcalculate material properties. The developed backcalculation program was verified using the field FWD data collected from Long-term Pavement Performance (LTPP) database. Finally, the effects of pavement temperature, magnitude of dropping weight in FWD test on the backcalculated material properties, and effects of moisture and k-values on resilient modulus distribution within the subgrade soil were investigated.

4.2. Characterization of Moisture Distribution within Fine-grained Subgrade Soil

Fine-grained subgrade soil is the in situ unsaturated material upon which the pavement structure is built. The existence of moisture within the subgrade soil directly affects its resilient modulus, swell-shrink behavior, and thereby the overall stiffness and

performance of asphalt pavements (i.e. fatigue cracking and rutting). Therefore, accurate prediction of moisture variation within the subgrade soil is crucial in pavement design. Gay (Gay 1994) developed a functional relationship between mean annual moisture depth and Thornthwaite moisture index (TMI) by applying Juarex-Badillo's approach (Juárez-Badillo 1975) based on the climatic data collected from 12 sites in Texas, USA. Based on Gay's work, Saha et al. (Saha *et al.* 2019) proposed a prediction model of equilibrium soil suction for fine-grained subgrade soil by considering both TMI and soil properties. The authors then developed a mechanistic-empirical model to predict moisture variation within subgrade soil by coupling Saha's equilibrium soil suction model with Mitchell's diffusion equation (Mitchell 1979). A new TMI prediction model was used in the prediction of soil equilibrium suction of subgrade soil at the depth of moisture active zone. The predicted soil suction was converted into volumetric water content through Fredlund-Xing SWCC equation (Fredlund and Xing 1994). The fitting parameters of the Fredlund-Xing SWCC equation were predicted by a previous developed artificial neural network (ANN) (Saha *et al.* 2018a).

The detailed description of the equilibrium soil suction and TMI models can be found in chapter 3 of this dissertation and will not be discussed herein for brevity. The predicted equilibrium soil suction at the depth of moisture active zone was used as a parameter in Mitchell's diffusion equation.

Moisture content at soil surface is affected by climate, drainage and vegetation cover (Mitchell 1979). According to Mitchell, the effect of climate on the moisture flow and seasonal movement of subgrade can be captured by imposing an arbitrary state of

suction according to local climatic condition (precipitation and evapotranspiration) at the soil surface. The arbitrary state of suction is set to be a function of time and used as a boundary condition in solving the diffusion equation.

The Mitchell diffusion equation and the boundary condition are given as:

$$\frac{\partial u}{\partial t} = \alpha \frac{\partial^2 u}{\partial z^2} \tag{4.1}$$

$$u(0,t) = \frac{U_0}{2} + U_1 \cdot \cos(n2\pi t) + U_2 \cdot \cos(2n2\pi t) + ...etc \tag{4.2}$$

$$u(z,t) \to 0 \text{ as } z \to \infty \tag{4.3}$$

where $u(0,t)$ is an arbitrary state of surface suction according to the site specific climate (precipitation and evapotranspiration); *z* is depth; *t* is time; α is diffusivity coefficient; *n* is the number of cycles of wetting and drying during a year; U0/2 is equilibrium soil suction in pF which is predicted from Saha's equilibrium soil suction model (Saha *et al.* 2019); and U_i is Fourier Series coefficients.

The solution of the diffusion equation is:

$$\begin{aligned} u(z,t) = \frac{U_0}{2} + U_1 \cdot \exp(-z\sqrt{\frac{n\pi}{\alpha}}) \cdot cos(n2\pi t - z\sqrt{\frac{n\pi}{\alpha}}) + \\ U_2 \cdot \exp(-z\sqrt{\frac{2n\pi}{\alpha}}) \cdot \cos(2n2\pi t - z\sqrt{\frac{2n\pi}{\alpha}}) + ...etc \end{aligned} \tag{4.4}$$

where the Fourier Coefficients U_i is determined by

$$U_i = \frac{2}{P}\int_0^P u(0,t) \cdot \cos(\frac{i\pi t}{P})dt,\ i = 0,1,2,... \tag{4.5}$$

where P=1/2n.

The moisture prediction model was calibrated using the field moisture content at the depth of 43.64 cm within the subgrade layer of LTPP pavement section 01-0102 collected on 10/15/1996. The calibrated diffusivity coefficient α for the subgrade soil was 0.0032 cm^2/sec. The details of data collection and model calibration can be found in chapter 3 of this dissertation. Figure 4.1 shows the predicted volumetric water content (VWC) profiles within the subgrade layer of pavement section 01-0102 on 05/20/1996 (left) and 08/23/1996 (right), which represent the typical VWC profiles in dry and wet seasons, respectively.

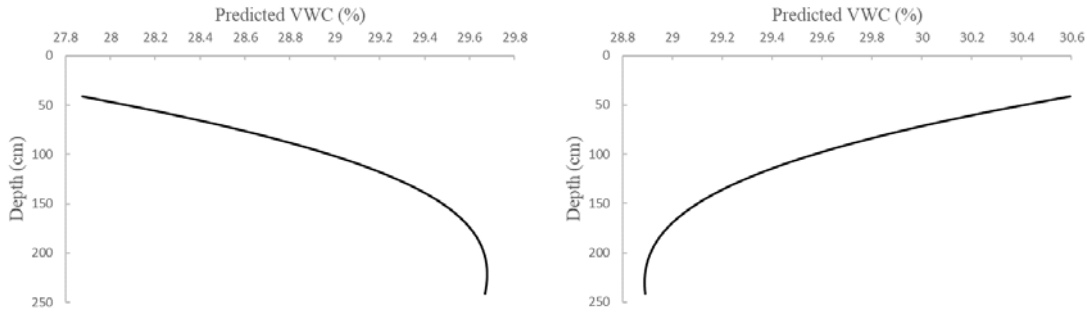

Figure 4.1 Predicted volumetric water content vs. depth on 05/20/1996 (left) and 08/23/1996 (right).

4.3. Resilient Modulus Model for Fine-grained Subgrade Soil

Resilient modulus is a measure of stiffness for unbound materials (i.e. unbound aggregate base and fine-grained subgrade soil). It was first introduced in AASHTO 1986 and defined as the applied stress to recoverable strain.

Seed et al. (Seed *et al.* 1967) first proposed a resilient modulus model (also called *K-θ* model) that emphasizes the stress hardening behavior of unbound granular material:

$$M_R = k_1 \left(\frac{\theta}{P_a} \right)^{k_2} \quad \textbf{(4.6)}$$

where M_R is resilient modulus; P_a is atmospheric pressure; θ is bulk stress ($\sigma_1 + \sigma_2 + \sigma_3$); and σ_1, σ_2, and σ_3 are three principal stresses.

Moossazadeh and Witczak (Moossazadeh and Witczak 1981) proposed a model by replacing bulk stress with deviator stress in *K*-θ model in order to capture the stress softening behavior of fine-grained (cohesive) subgrade soil:

$$M_R = k_1 \left(\frac{\sigma_d}{P_a} \right)^{k_2} \quad \textbf{(4.7)}$$

Where σ_d is deviator stress ($\sigma_1 - \sigma_3$).

Similarly, by considering deviator stress, Thompson and Robnett (Thompson and Robnett 1979) proposed bilinear model which has been the most commonly used resilient modulus model for fine-grained subgrade.

Later on, Witczak and Uzan (Witczak and Uzan 1988) proposed the universal model that was the first model that considers both stress hardening and softening effect of unbound base and cohesive subgrade soil, as presented in Eqn. (4.8):

$$M_R = k_1 P_a \left(\frac{\theta}{P_a} \right)^{k_2} \left(\frac{\tau_{oct}}{P_a} \right)^{k_3} \quad \textbf{(4.8)}$$

where $\tau_{oct} = \frac{1}{3}\left[(\sigma_1 - \sigma_2)^2 + (\sigma_1 - \sigma_3)^2 + (\sigma_2 - \sigma_3)^2 \right]$.

As shown in Eqn. (4.9), the generalized model was developed based on the universal model with a slight modification, which is currently being used by AASHTOWare-ME (ARA 2004).

$$M_R = k_1 P_a \left(\frac{\theta}{P_a} \right)^{k_2} \left(\frac{\tau_{oct}}{P_a} + 1 \right)^{k_3} \quad \textbf{(4.9)}$$

Lytton (Lytton 1996) proposed a new resilient modulus model (also called Lytton model) by incorporating the moisture and suction term into the universal model, as presented in Eqn. (4.10). It can be seen from Eqn. (4.10) that the existence of moisture (in unsaturated condition) in the soil induces an additional inter-particle normal force and thus stiffen the soil structure. In order to characterize the stress-dependency and moisture sensitivity in the subgrade soil, Lytton model was used in this study.

$$M_R = k_1 P_a \left(\frac{I_1 - 3\theta f h}{P_a} \right)^{k_2} \left(\frac{\tau_{oct}}{P_a} + 1 \right)^{k_3} \quad \textbf{(4.10)}$$

where I_1 is the first invariant of the stress tensor in kPa; P_a is atmospheric pressure in kPa; θ is volumetric water content; h is matric suction in kPa; f is saturation factor, $1 \le f \le \frac{1}{\theta}$; τ_{oct} is octahedral shear stress in kPa; and k_1, k_2, and k_3 are fitting coefficients where k_1 is in kPa and k_2 and k_3 are dimensionless.

f is a saturation factor which is multiplied by volumetric water content and soil suction to represent the stress exerted on the soil skeleton due to the existence of water. The expression of the saturation factor is given as

$$f = 1 + \frac{S - 85}{15}\left(\frac{1}{\theta} - 1\right) \quad \textbf{(4.11)}$$

where S is degree of saturation in percent; and θ is volumetric water content in decimal.

4.4. Nonlinear Forward Calculation Procedure

Modelling fine-grained subgrade soil with stress- and moisture-dependent resilient modulus involves iterative calculation among modulus, stress and deformation. Unlike Abaqus, the coefficient-form partial differential equation (PDE)-based technique in COMSOL Multiphysics, a FEM software, has proved to be capable of solving the above coupling problem (Zhang *et al.* 2016, 2018) without developing a user-defined subroutine. The *coefficient form PDE* in COMSOL Multiphysics is a strong form PDE and is automatically converted into a weak form PDE when solving the user-defined PDE. Therefore, the *coefficient form PDE module* in COMSOL Multiphysics was used in this study to model the stress- and moisture-dependent behavior of subgrade soil. The following steps were followed to model the fine-grained subgrade soil in COMSOL Multiphysics.

Step 1. Define the material properties and pavement thicknesses as input in the *Parameters Module*. Table 4.1 presents the structure of the pavement section (ALABAMA 01-0102) to be modelled including layer thicknesses, material types, constitutive models, and model parameters.

Step 2. Develop a 2D-axisymmetric structure as shown in Figure 4.2 to model the pavement section ALABAMA 01-0102 in COMSOL Multiphysics with the asphalt layer of 10.7 cm, an unbound granular base layer of 30.5 cm, and a subgrade layer of 200 cm.

A ramp load with 6 incremental loading steps was applied in order to obtain a converged solution of the iterative calculation. An 'Extremely fine' type of element size was selected to generate the mesh of the pavement structure.

Step 3. Create a new physics from *'Coefficient Form PDE' module* to define two *Dependent Variables* u11 and u12 with a unit of N/m^2.

Step 4. Define the two *Dependent Variables* which are used in calculating the stress- and moisture-dependent resilient modulus of the subgrade layer. The two *Dependent Variables* are given by

$$Solid2.I1s \tag{4.12}$$

$$sqrt(abs(solid2.II2s)*2/3) \tag{4.13}$$

where $Solid2.I1s$ is the first invariant of the stress tensor; $sqrt(abs(solid2.II2s)*2/3)$ is the second invariant of the deviator stress tensor.

Step 5. Import a predefined function 'VWCS_Pa' which was defined as the multiplication of soil suction and volumetric water content. The procedure of predicting 'VWCS_Pa' can be found in section 4.2 of this dissertation.

$$VWCS\_Pa = \theta fh \tag{4.14}$$

Step 6. Define the stress- and moisture-dependent resilient modulus as a variable using the two predefined *Dependent Variables* in Eqns. (4.12 – 4.13) as presented below.

$$E_{sg} = k_1 * P_a \left(abs\left(u11\right)/P_a + 3*VWCS\_Pa/P_a\right)\wedge k_2 * \left(u12/P_a + 1\right)\wedge k_3 \tag{4.15}$$

Table 4.1. Pavement Structures, Material Models, Parameters used in the forward calculation Program.

Pavement layers (thickness)	Material	Constitutive Model	Model Parameters
Layer 1 (10.7 cm)	Asphalt concrete	Linear elastic	Elastic modulus, Poisson's ratio
Layer 2 (30.5 cm)	Unbound granular base	Linear elastic	Elastic modulus, Poisson's ratio
Layer 3 (200 cm)	Fine-grained subgrade	(a) Linear elastic (b) Nonlinear elastic	(a) Elastic modulus, Poisson's ratio (b) k_1, k_2, k_3, Poisson's ratio

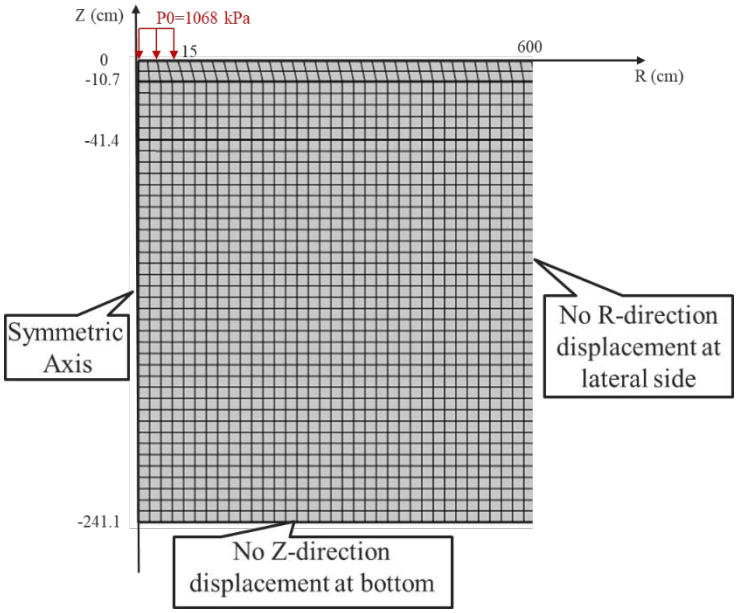

Figure 4.2 Axisymmetric finite element model of pavement section ALABAMA 01-0102.

4.5. Nonlinear Backcalculation Procedure

The Optimization Module can be used in COMSOL Multiphysics to solve the problems that is to determine the model parameters that provides the simulated data which best matches the measured counterparts. In this study, the problem is to best match the

simulated surface deflection basin with the field FWD measurements by optimizing the material properties including moduli of asphalt and base layer, and k-values for the subgrade layer.

There are several optimization algorithms available in COMSOL Multiphysics, which can be divided into gradient-based and gradient-free algorithms. Among them, *Bound Optimization by Quadratic Approximation* (BOBYQA) (Powell 2009) is a gradient-free algorithm which was employed in this study. BOBYQA is an iterative algorithm that minimizes the value of objective function, subject to bounds on the variables. A quadratic model is used to approximate the objective function in each iteration, and is updated by minimizing the Frobenius norm of the difference in the Hessians of the two consecutive quadratic approximations.

The objective function was defined as the relative difference between the simulated and measured surface deflection basins as presented below.

$$Objective\ funtion = \sum_{i=1}^{7}\left(\frac{D_s(i) - D_m(i)}{D_m(i)}\right)^2 \qquad \textbf{(4.16)}$$

where $D_s(i)$ is the simulated surface deflection for the i^{th} sensor; $D_m(i)$ is the field measured surface deflection for the i^{th} sensor.

Due to the iterative nature of the nonlinearity in the forward calculation procedure, it might take a relatively long time to back-calculate all the parameters (Elastic moduli of asphalt and base layers, and k_1, k_2, and k_3 for the subgrade layer). To improve the computation efficiency of the backcalculation program, a two-step backcalculation procedure was employed.

Step one: as shown in Figure 4.3, all the layers are assumed to be linear elastic. Lytton model can be simplified to be elastic model by setting k_2 and k_3 to be zero. Therefore, the parameters to be calculated in this step include: elastic moduli of the asphalt and base layers, and k_1 for the subgrade layer.

Step two: as shown in Figure 4.4, stress- and moisture- dependency of the subgrade layer is considered. The parameters to be backcalculated include Elastic moduli of asphalt and base layers, and k_1, k_2, and k_3 for the subgrade layer. The backcalculated parameters in step 1 are used as the seed values in step 2. A good seed values for k_2 and k_3 are obtained by fitting the Lytton model into the resilient modulus test data that contains the 15 lab measured resilient moduli under various combinations of axial and confining pressures.

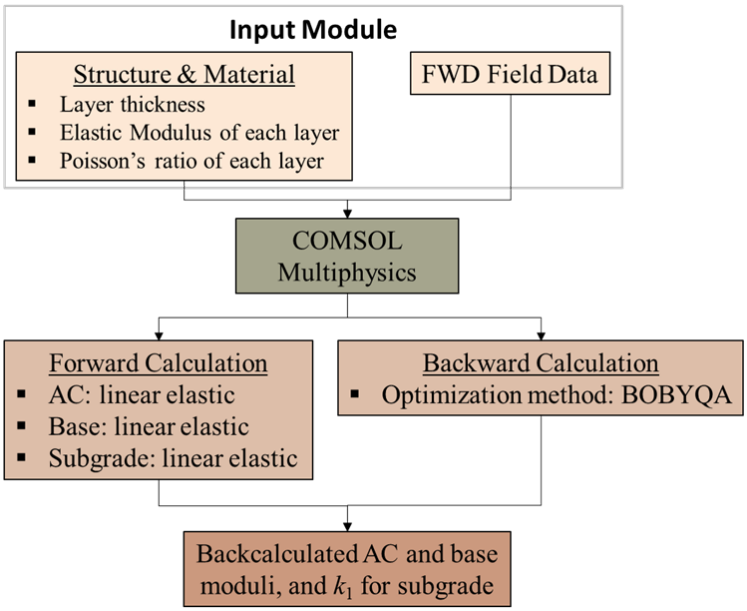

Figure 4.3 Step one of developed backcalculation procedure.

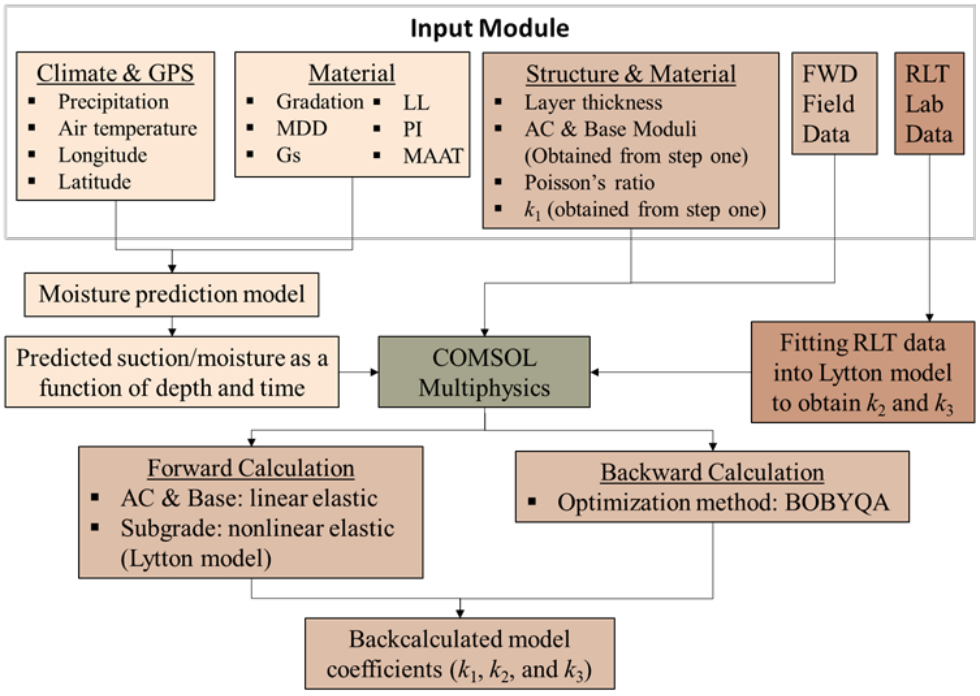

Figure 4.4 Step two of developed backcalculation procedure.

4.6. Verification of Nonlinear Backcalculation Module

This section verifies the proposed backcalculation algorithm using the field FWD data collected at Long-term Pavement Performance (LTPP) section ALABAMA 01-0102. The moisture and suction profiles on a specified day within the subgrade layer of the pavement were first predicted by the previously developed model described in section 4.2. They were then imported into the backcalculation algorithm as an input function. The input data can be divided into two categories, namely, the input for the moisture prediction model and the input for the backcalculation algorithm.

The input for predicting moisture variation within the subgrade layer is presented in Table 4.2 and Figure 4.5. The pavement structure (thickness of each layer) and surface deflection data with the corresponding dropping weights measured in the field by falling

weight deflector (FWD) are the input data for the backcalculation algorithm. Specifically, the measured FWD data were collected 91.4 m away from the start of the LTPP section 01-0102 mid lane on 04/17/1996. The drop load is 1068 kPa with load radius of 0.15 m.

Table 4.2 Input for the moisture prediction model

Latitude	32.6357°	Liquid Limit	41
Longitude	85.29572°	Plastic Index	16.5
MAAT* (°C)	17.97	Tested Moisture Content (%)	15.60%
Specific Gravity	2.74	Depth of Moisture Measurement (cm)	43.64
Dry Density (pcf)	101.78	Date of Moisture Measurement	10/15/1996
MDD** (pcf)	112.6		

* Mean Annual Air Temperature. ** Maximum Dry Density.

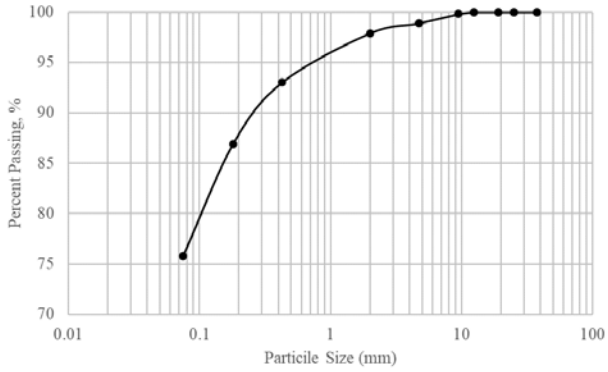

Figure 4.5 Aggregate gradation of the subgrade in LTPP ALABAMA 01-0102

In step one of the backcalculation procedure, all the pavement layers were assumed linear elastic. Figure 4.6 compares the measured and predicted surface deflection basins after the optimization process. It can be seen that the predicted surface deflection matches well with the field measurements. The backcalculated moduli were compared with the backcalculation results provided by LTPP as presented in Figure 4.7. It can be

seen that the backcalculated moduli of the asphalt and subgrade layers from LTPP are almost double the moduli backcalculated using the proposed algorithm, while the LTPP backcalculated base modulus is around one third of the counterpart backcalculated by the proposed algorithm. Due to the fact that unbound granular base normally has much larger modulus than the modulus of fine-grained subgrade soil, the authors believe that the backcalculated moduli from the proposed backcalculation algorithm are more reasonable.

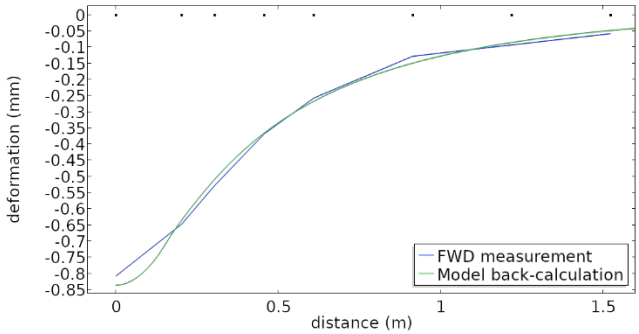

Figure 4.6 Comparison between measured and predicted deflection basins obtained in step one.

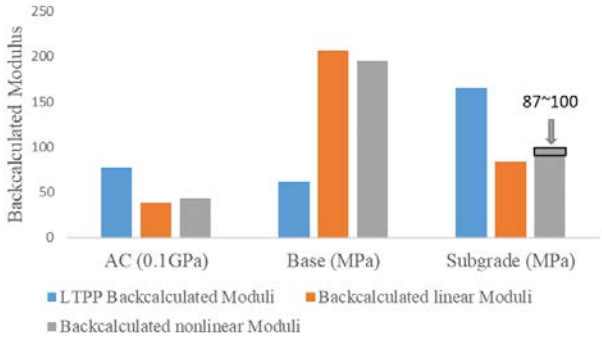

Figure 4.7 Comparison of backcalculated moduli by LTPP, linear backcalculation and nonlinear backcalculation algorithms.

In step two, Lytton model was used in the subgrade layer, and asphalt and base layers were assumed to be linear elastic. As mentioned before, the purpose of step one was to obtain good estimates of moduli of asphalt and base layer, and k_1 for the subgrade layer used as seed values in the nonlinear backcalculation procedure (step two). The backcalculated moduli of asphalt and base layer, and k_1 for the subgrade layer from step one were 3842.33 MPa, 206.78 MPa, and 827.88 kPa. The corresponding backcalculated modulus of the subgrade layer was 83.86 MPa which can be calculated using Lytton model with k_1 of 827.88 kPa and k_2 and k_3 of zero.

The seed values of k_2 and k_3 were obtained by fitting the Lytton model into the resilient modulus test data for the subgrade soil of pavement section ALABAMA 01-0102 that contains the 15 lab measured resilient moduli under various combinations of axial and confining pressures. Figure 4.8 shows the comparison between the measured and predicted resilient moduli using the fitted k-values with R-SQUARED of 0.96. The fitted k_1, k_2, and k_3 were 301.09 Pa, 1.28, and -1.00, respectively.

According to Lytton (Lytton 1996), the term $3\theta fh$ in Lytton model was to represent the stress exerted on the soil skeleton due to the existence of water, which contribute to the increase of the resilient modulus of the subgrade soil. Therefore, the moisture and suction profiles on the date when the FWD test was conducted were predicted using the previously developed moisture prediction model (chapter 3). The predicted volumetric content and suction profiles are shown in Figure 4.9. Note that the only Figure 4.9(b) were imported into the backcalculation algorithm.

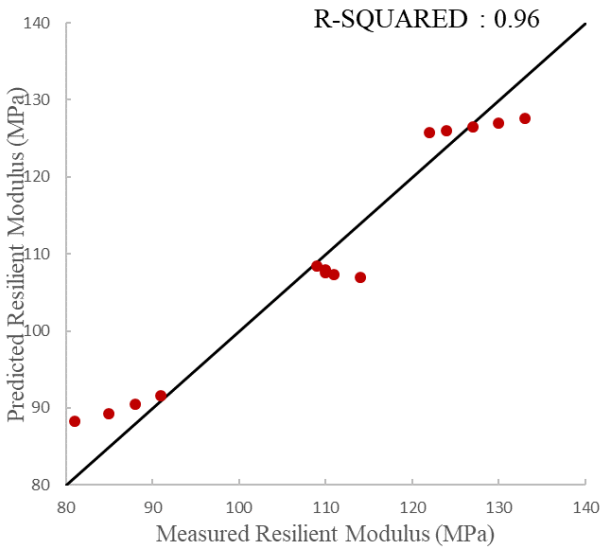

Figure 4.8 Comparison between measured and predicted resilient moduli using the fitted k-values

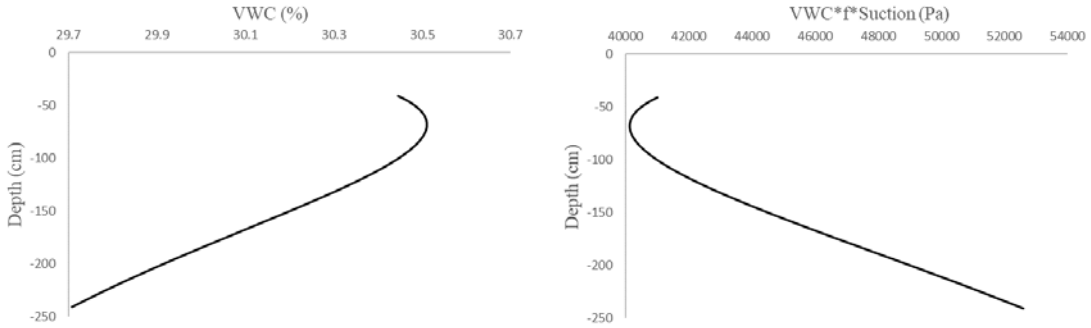

(a) (b)

Figure 4.9 Predicted (a) volumetric water content profile and (b) multiplication of volumetric water content, saturation factor, and suction within the subgrade layer on 04/17/1996 for LTPP pavement section ALABAMA 01-0102.

A *Time Dependent Study* was created in COMSOL Multiphysics with a 6-level incremental loading applied in 0.05s in order to obtain converged solution when coupling the *optimization module* with *Coefficient Form PDE*. Figure 4.10 compares the measured deflection basin and predicted counterpart using the optimized material properties which shows that the predicted deflection basin matches well with the field

measurement. The backcalculated moduli of asphalt and base, k_1, k_2, and k_3 were 4454.03 MPa, 200.56 MPa, 598.16 Pa, 1.29, and -0.96, respectively.

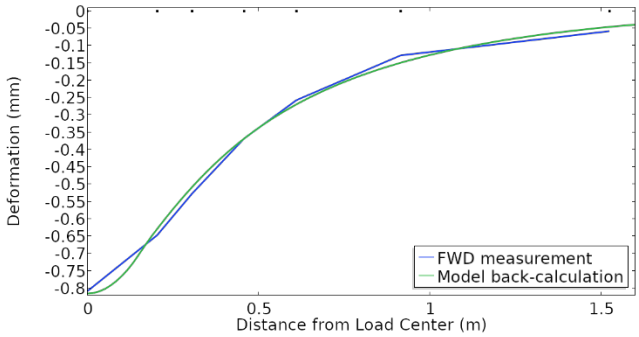

Figure 4.10 Comparison between measured and predicted deflection basins obtained in step two.

Figure 4.11 presents the stress- and moisture-dependent resilient modulus distribution within the subgrade layer after convergence. The convergence here means that the resilient modulus at each location within the subgrade layer is infinitely close to the calculated value using Lytton model with optimized k-values, local stress state, and imported moisture function. It can be seen that moisture distribution which was represented as $3\theta fh$ is predominant in determining the resilient modulus distribution because the location of maximum resilient modulus occurred at the bottom of the subgrade course where $3\theta fh$ reached the maximum. The location of the maximum resilient modulus occurred at the left bottom instead of somewhere else at the bottom because the bottom left part was under the loading area and has larger first invariant of the stress tensor compared with the area on the right, as presented in Figure 4.12. It implies that the stress state also takes some effect but it is not as important as the

moisture condition within the subgrade soil. Zhang et al. (Zhang *et al.* 2018) considered stress dependency when modelling resilient behavior of unbound base course, and it was found that the maximum resilient modulus occurred at the top left corner within the base course where the first invariant of the stress tensor reached the maximum. This means that when the stress state is predominant in determining the resilient modulus distribution such as within the unbound base course, the maximum resilient modulus can be observed at the top left corner under the loading area. To Summarize, moisture condition is predominant in fine-grained subgrade soil in determining the resilient modulus, whereas the stress state is predominant in the unbound aggregate base course (stress hardening) of asphalt pavements. The same pattern was also found in previous studies (Ceylan *et al.* 2005, Al-Qadi *et al.* 2010, Ahmed *et al.* 2016).

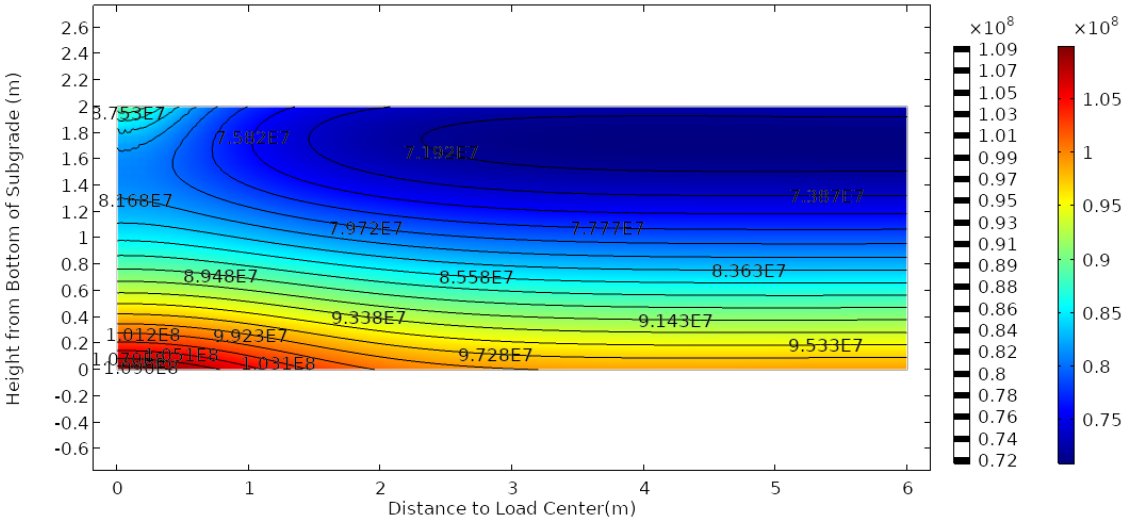

Figure 4.11 Contour of stress- and moisture-dependent modulus (MPa) in subgrade course at a load level of 1068 kPa for pavement section ALABAMA 01-0102.

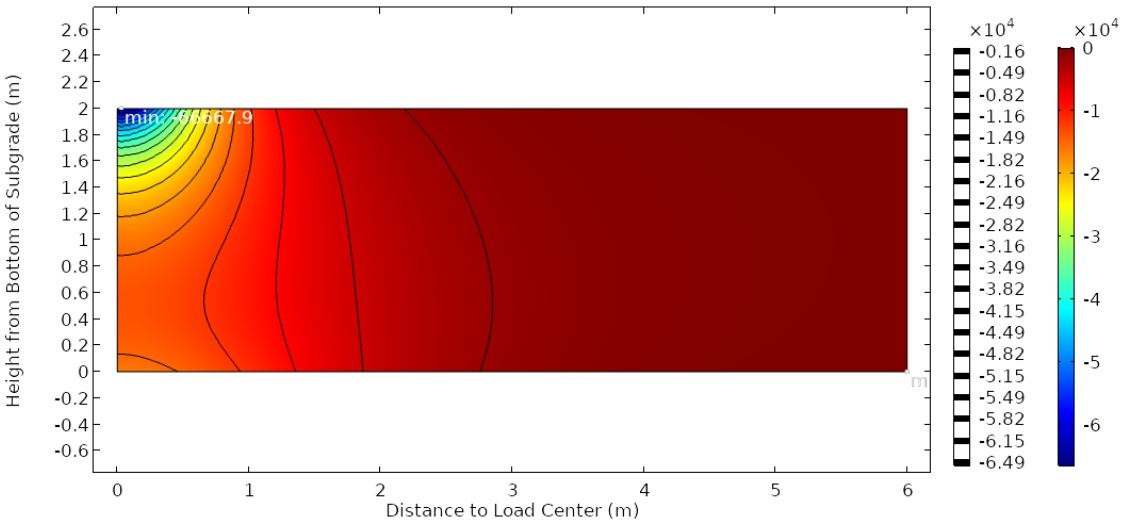

Figure 4.12 Contour of first invariant of stress tensor (MPa) in subgrade course at a load level of 1068 kPa for pavement section ALABAMA 01-0102.

Coefficient k_1 is positively related to Young's modulus so that k_1 should always be positive since the resilient modulus is always positive. Coefficient k_2 is the exponent of the bulk stress and moisture stress (defined as $3\theta fh$) in Lytton model, and increasing the bulk stress and moisture stress produce an increase or stiffening of the subgrade soil (i.e. larger resilient modulus). Thus, Coefficient k_2 should always be positive as well. Coefficient k_3 is the exponent of the octahedral shear stress, and k_3 should always be negative since the increase of the octahedral shear stress produces the softening of the subgrade soil (i.e. smaller resilient modulus).

Figure 4.13 compares the *k*-values obtained by fitting Lytton model into the resilient modulus test data and by the FWD backcalculation algorithm, respectively. It was found that coefficients k_2 and k_3 backcalculated through different methods were close to each other with 4% and 1% of the relative difference, while the FWD backcalculated k_1 was almost double the lab-fitted k_1 with the relative difference of 88%. Previous studies

showed that a soil specimen re-compacted to the same dry density from different initial water content could produce different inherent soil structure (Lambe 1958, Mancuso *et al.* 2002, Ng *et al.* 2013). The coring in the field and/or the re-compaction of the soil specimens in lab could possibly change its inherent structure, and therefore lead to different k_1 values. Therefore, to reflect the resilient response of the subgrade soil in the field, coefficient k_1 should be backcalculated using field performance data (i.e. FWD data) instead of lab resilient modulus test data.

Figure 4.13 Comparison of k-values backcalculated using FWD and lab resilient modulus test data, respectively.

4.7. Temperature Effect on Backcalculated Material Properties

This section studied temperature effect on the material properties backcalculated using the proposed backcalculation algorithm. The field FWD data for LTPP pavement section 01-0102 measured at different times in 1996 with the corresponding pavement temperatures measured at different depths within the asphalt layer were collected to study the temperature effect. The temperature sensors were installed in the asphalt layer of the pavement section at 25 mm, 51 mm, and 76 mm below the pavement surface. The temperature of the asphalt layer was represented by the average of the three sensor

measurements as shown in Figure 4.14. It was assumed that the temperature of the base and subgrade layers of the pavement were not affected by local climate condition. Figure 4.15 shows the deflection basins measured in 1996. The effect of drop loads were ignored because the target drop load for all of the selected FWD data were 71kN. The final drop loads are given in Figure 4.16. It can be seen that the measured surface deflections under the load center increase as temperature goes up and vice versa. The effect of moisture variation within the subgrade course due to local climatic condition was also taken into account. As shown in Figure 4.17, the moisture content and suction profiles for the days when the FWD test were conducted were predicted using the moisture prediction model described in section 4.2. The details of the moisture prediction model and the used input data can be found in chapter 3 of this dissertation.

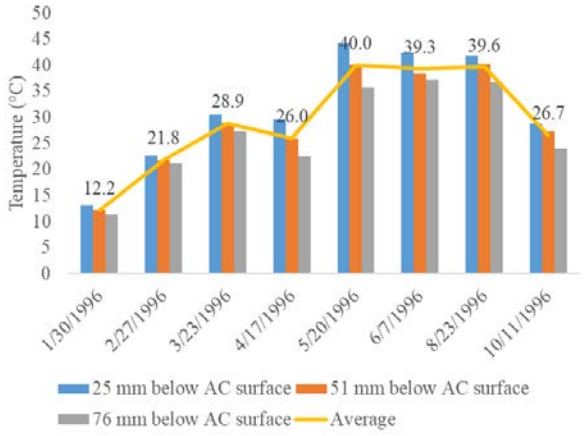

Figure 4.14 Measured temperatures at depths of 25, 51, and 76mm below pavement surface within asphalt layer in 1996 for LTPP section 01-0102.

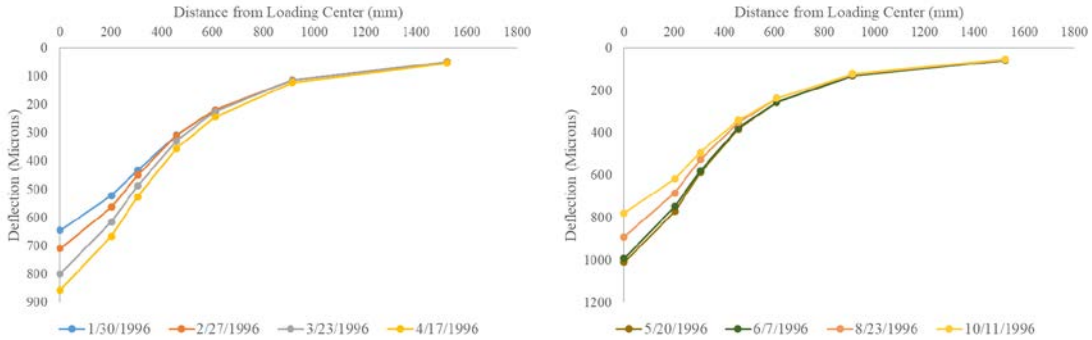

Figure 4.15 Deflection basins measured at different dates in 1996 for LTPP 01-0102.

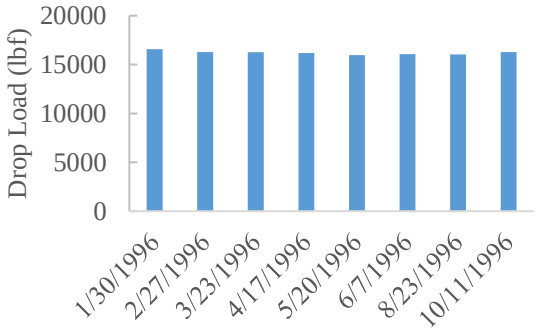

Figure 4.16 Drop load of the FWD tests conducted on different days in 1996 for LTPP 01-0102.

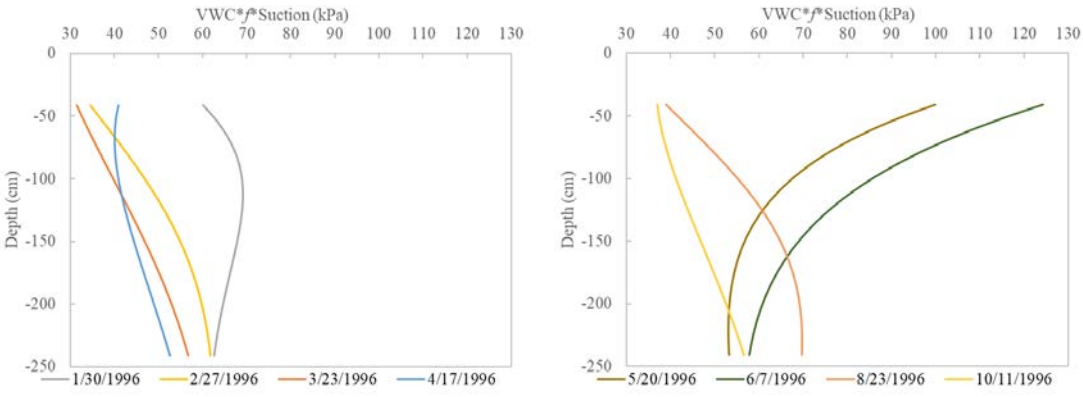

(a) (b)

Figure 4.17 Predcited volumetric water content and suction profiles within subgrade layer at different dates in 1996 for LTPP 01-0102.

When running the backcalculation algorithm, what's changed in the input data includes surface deflection, the corresponding dropping load, and the moisture and suction profiles, while the rest parameters kept constant. The studied material properties include elastic moduli of the asphalt and base layers, and k-values (k_1, k_2 and k_3) for the subgrade layer.

The backcalculated modulus of the asphalt layer are given in Figure 4.18(a). The asphalt layer were assumed not to be affected by the moisture content underneath so that pavement temperature was the only factor that influences surface modulus. As expected, the backcalculated modulus of the asphalt layer decreases with the increase of the averaged temperature within the asphalt layer and vice versa, which implies that the proposed backcalculation algorithm is capable of capturing the temperature effect on the asphalt mixture.

Figure 4.18(b) presents the backcalculated base moduli under different temperatures. No clear correlation between the base modulus and temperature was observed.

Figure 4.18(c) shows the backcalculated coefficient k_1 used in Lytton model for the subgrade course. According to the first four months' results, it is clear that there is a strong positive correlation between temperature and k_1, while no clear correlation can be observed in later four months. According to Figure 4.17, the moisture condition during the first four months are relatively close while the reversed pattern occurs in later months which could possibly explain why no clear correlation was observed in later four months. What's more, the change of moduli on top of the subgrade layer affect the stress distribution within the pavement structure. Specifically, stiffer asphalt layer is able to

spread the stress in a larger region underneath the surface layer to reduce the damage in the weaker layers underneath. That's why a negative correlation between modulus of asphalt layer and k_1 was observed in the first four months. Notice that the above correlation does not mean that temperature directly affects the stiffness of the subgrade soil.

According to Figure 4.18(d) and 4.18(e), the backcalculated k_2 ranges from 1.22 to 1.34, and the backcalculated k_3 ranges from -1.03 to -0.95. It can be concluded that k_2 and k_3 are not affected by temperature in the asphalt layer.

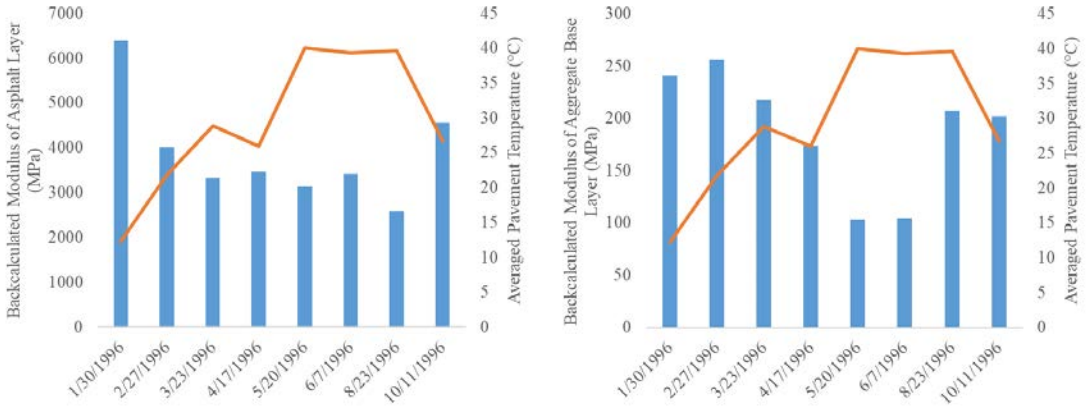

(a) (b)

Figure 4.18 Backcalculated material properties with different temperature and moisture conditions (a) AC modulus; (b) base modulus; (c) k_1 for subgrade layer; (d) k_2 for subgrade layer; (e) k_3 for subgrade layer.

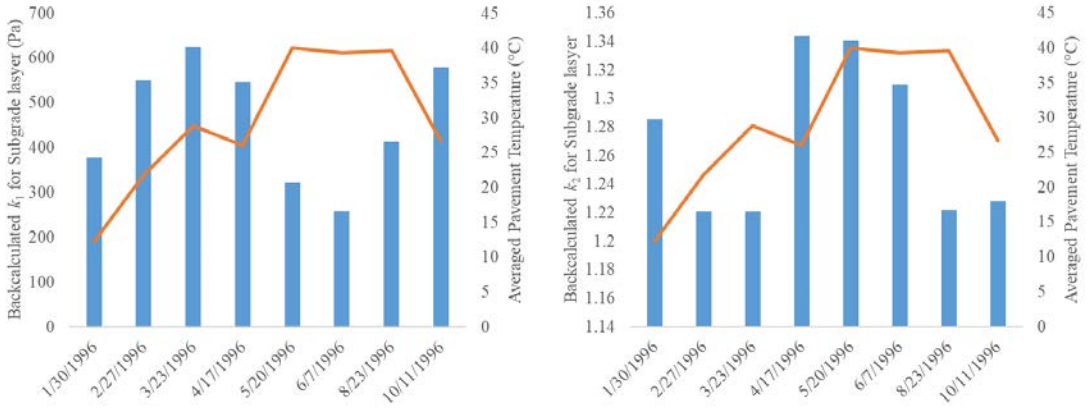

(c)

(d)

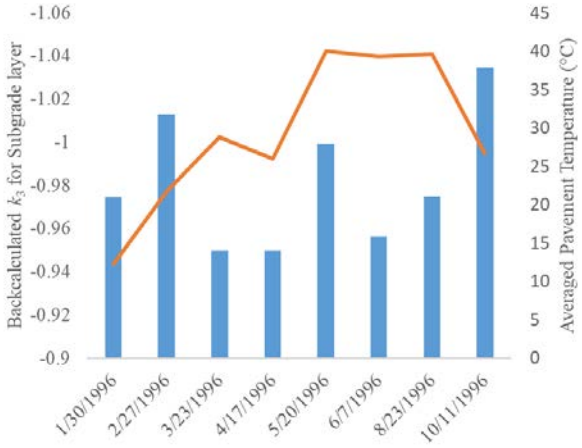

(e)

Figure 4.18 Backcalculated material properties with different temperature and moisture conditions (a) AC modulus; (b) base modulus; (c) k_1 for subgrade layer; (d) k_2 for subgrade layer; (e) k_3 for subgrade layer (cont'd).

4.8. Effect of Drop Load of FWD Test on Backcalculated Material Properties

This section studied the effect of drop load on the backcalculated material. As shown in Figure 4.19, the field FWD data were collected at 91.4m away from the start of the LTPP pavement section 01-0102 mid lane at 7:23AM on 04/17/1996 with different drop loads. As expected, the surface deflection measured under the load center increases with the increase of the drop loads.

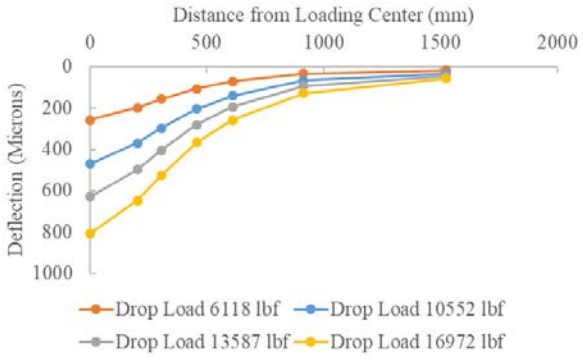

Figure 4.19 FWD deflection basins measured at 91.4m away from start of LTPP pavement section 01-0102 mid lane at 7:23AM on 04/17/1996 with different drop loads.

The backcalculated moduli of asphalt and base layers are presented in Figure 4.20(a). It can be seen that the backcalculated modulus of the asphalt layer increases with the increase of the drop load except when the drop load changes from 13587 lbf to 16972 lbf, while the opposite correlation was observed in the case of the backcalculated base modulus. This is because higher drop height is needed to produce larger drop load in FWD test; higher drop height produces higher drop load frequency; and the dynamic modulus of asphalt mixture is frequency dependent so that larger modulus was obtained with larger drop load through backcalculation. What's more, the stiffer surface layer dissipates more stress induced by the traffic load and spread the stress in a larger region within the base course so that the stress-dependent base modulus is reduced (even though the stress dependence was not considered in the base course in this study). Coefficient k_1 is proportional to the elastic modulus of the subgrade course and this explains the decrease of coefficient k_1 with the increase of the drop load (Figure 4.20 (b)). The maximum differences among the backcalculated k_1, k_2 and k_3 are 0.18, 0.06 and

0.07, respectively. Therefore, it can be concluded that k_2 and k_3 are independent of drop loads.

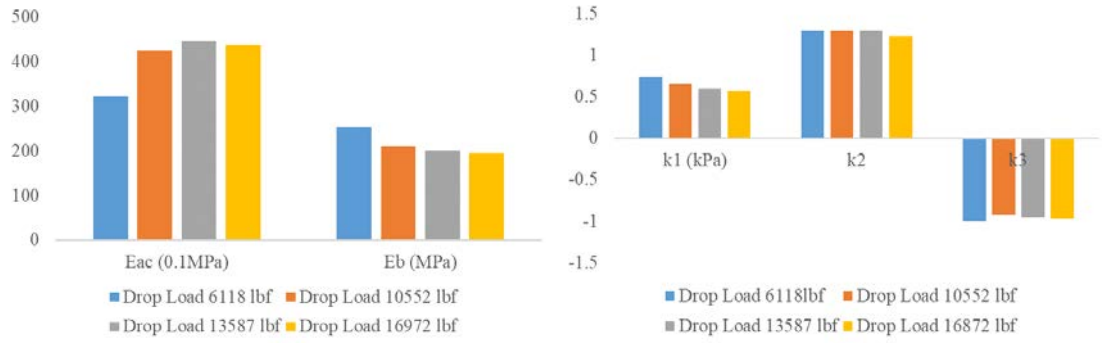

(a) (b)

Figure 4.20 Backcalculated material properties by different drop loads.

4.9. Effect of Moisture and k-values on Resilient Modulus Distribution within Subgrade soil

Previous studies have shown that increasing moisture content or decreasing matric suction within the soil specimens causes the decrease of the resilient modulus (Seed *et al.* 1967, Fredlund *et al.* 1977, Yang *et al.* 2005). However, the effect of lab-based and field-based k-values on the resilient modulus distribution within the subgrade soil has not been reported yet.

In this section, different combinations of moisture conditions and k-values were used as input of the forward algorithm to study their effect on the resilient modulus distribution within the subgrade course of asphalt pavements. Specifically, as for the moisture condition within the subgrade course, zero moisture content and field moisture condition predicted by the moisture prediction model were considered; as for the k-values, lab and FWD backcalculated k-values were considered.

Figure 4.21 compares the resilient modulus profile within the subgrade layer predicted using different combinations of moisture conditions and k-values as input. After zero moisture content was employed, there was no stress- or moisture-dependency observed in the predicted subgrade resilient modulus profile no matter what type of k-values were used. The predicted resilient modulus within the subgrade layer was 35 MPa which is the minimum value that is allowable in the forward solution. This implies that the moisture effect on the resilient modulus profile is predominant in the subgrade course. Compared with the resilient modulus profile predicted through the FWD backcalculated k-values and field moisture condition, the k-values obtained through resilient modulus test result underestimate the resilient modulus of the subgrade.

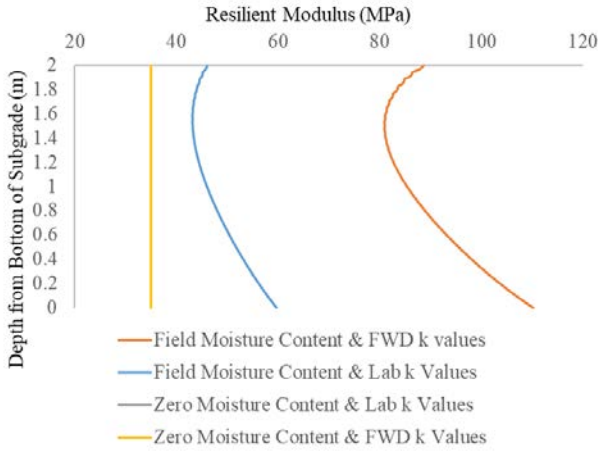

Figure 4.21 Resilient modulus profile within subgrade layer predicted using different combinations of mositure condition and k-values

4.10. Conclusion

In this study, a FWD-based backcalculation program that considers moisture- and stress-dependent resilient modulus for fine-grained subgrade soil was developed using

COMSOL Multiphysics. In the forward calculation algorithm, we used Lytton model to characterize the stress-dependent and moisture-sensitive behavior in fine-grained subgrade soil by using coefficient form PDE module in COMSOL Multiphysics. A new moisture prediction model was incorporated into the forward calculation algorithm to predict the moisture and suction profile at any day and any depth within the subgrade layer. Bound Optimization by Quadratic Approximation (BOBYQA) method was used in the backcalculation procedure to back-calculate material properties including elastic moduli of asphalt and base layers, and k-values for the subgrade layer. A two-step backcalculation procedure was provided to improve the computation efficiency and accuracy. The backcalculation algorithm was verified using the FWD data collected from LTPP database. Investigations were also conducted including the effects of pavement temperature, magnitude of dropping weight in FWD test on the backcalculated material properties, and effects of moisture and k-values on resilient modulus distribution within the subgrade soil.

The following conclusions were made:

- The moisture condition is predominant in fine-grained subgrade soil in determining the resilient modulus, while the stress state is predominant in the unbound aggregate base course.
- By comparing the k-values obtained by fitting Lytton model into the resilient modulus test data with the k-values backcalculated through the proposed FWD backcalculation algorithm, we found that the FWD backcalculated coefficient k_1 was almost double the lab-fitted k_1 with the relative difference of 88%. However, there is

no significant difference in the coefficients k_2 and k_3 backcalculated through different methods. This is because the coring in the field and/or the re-compaction of the soil specimens in lab could possibly change its inherent structure, and therefore lead to different k_1 values backcalculated using lab and field data, respectively. Therefore, it is recommended to use field data (i.e. FWD) instead of RLT data to back-calculate material properties of subgrade soil (i.e. k_1).

- The backcalculated modulus of the asphalt layer decreased with the increase of the averaged temperature within the asphalt layer, which implies that the proposed backcalculation algorithm is capable of capturing the temperature effect on the asphalt mixture. There was no clear correlation between the base modulus and AC temperature observed. A strong positive correlation between AC temperature and backcalculated k_1 during the first four months of the studied year. This is because stiffer asphalt layer dissipates more stress and spread the stress in a larger region in the underlying layers so that the stress-dependent base and subgrade layers react with smaller resilient modulus that is reflected as smaller backcalculated k_1. Coefficient k_2 and k_3 were found not to be affected by AC temperature.
- We studied the drop load effect on the backcalculated material properties. It was found that increasing drop loads produced larger backcalculated AC modulus, smaller base modulus, and smaller backcalculated k_1, which means that stiffer surface layer dissipates more stress induced by the traffic load and spread the stress in a larger region within the base and subgrade courses so that the stress-dependent base and subgrade moduli are reduced. Note that k_1 is proportional to the elastic

modulus of the subgrade course so that the change of k_1 can be used to represent the change of subgrade stiffness. Similar to the conclusion from the study of the temperature effect, the backcalculated k_2 and k_3 are independent of drop loads.

- The resilient modulus of the subgrade soil did not show either stress or moisture dependency after using zero moisture content in Lytton model. Compared with the resilient modulus profile predicted through the FWD backcalculated k-values and field moisture condition, the k-values obtained through resilient modulus test result underestimate the resilient modulus of the subgrade layer.
- In future studies, we will consider cross-anisotropy in modelling resilient response of unbound base and subgrade soil. Empirical relationships between lab-based and FWD based coefficient k_1 will be established.

5. A UNIFIED MECHANICS-BASED FRAMEWORK FOR TOP-DOWN CRACK INITIATION AND PROPAGATION IN ASPHALT PAVEMENTS

5.1. Introduction

Top-down fatigue cracking (TDC) is a common distress type in flexible pavements throughout the world. In Florida, 90 percent of pavements scheduled for rehabilitation have deficient crack ratings, and almost all of the deficient pavement sections have experienced TDC (Roque *et al.* 2004). TDC initiates at the surface or near the surface of asphalt pavements due to the critical tensile or shear stresses at the edge or within the wheel paths (Ozer *et al.* 2011, Wang *et al.* 2013, Ling *et al.* 2017), while bottom-up cracking (BUC) initiates at the bottom of the asphalt layer due to its bending effect caused by tire loads. There are two phases in TDC, namely, crack initiation and then crack propagation. TDC initiation phase generally starts from size of an air void in asphalt layer and ends when crack depth reaches 7.5 mm according to Lytton et al. (Lytton *et al.* 1993, 2018). As a crack depth grows to between 16 mm and 22 mm, the developed longitudinal crack would generally intersect with transverse crack and transition into medium severity alligator cracking which is similar to the cracking pattern caused by BUC (Ling *et al.* 2019, Canestrari and Ingrassia 2020).

Several factors that affect top-down crack initiation and growth have been identified by researchers. These factors include traffic loads, pavement structure, modulus gradient of asphalt layer, asphalt mixture properties, thermal effects, and construction quality (Ling *et al.* 2019, 2020, Canestrari and Ingrassia 2020, Huang *et al.* 2021). Traffic loads is generally believed to be the most important factor that contributes to TDC initiation and

propagation. For medium and thick asphalt pavements, TDC initiates and propagates at the edge or near the edge of tires due to a localized tire loads. It was observed that the tire-pavement contact stress is non-uniform and can be decomposed into longitudinal, vertical (shear) and transverse (tensile) stresses in a non-circular tire patch area (De Beer *et al.* 1997). The contact stresses in three directions correspond to three different fracture modes: sliding mode under vertical stress, opening or tensile mode under transverse stress and tearing mode under longitudinal stress (Luo *et al.* 2018). For thin asphalt pavements, TDC initiates at a distance away from the wheel-path due to the bending stress where it has the maximum tensile stress at the pavement surface (Roque *et al.* 2010). Modulus gradient in asphalt layer is another factor that contributes to TDC due to aging and climatic conditions. Long-term aging starts after pavement lay-down, and the top part of the asphalt layer ages faster than the bottom part due to excessive exposure to air and sunlight. As a result, the asphalt in the top becomes stiffer than the asphalt near the bottom. Finally, the aged asphalt layer becomes more and more brittle and more prone to cracking (Pellinen *et al.* 2004, Roque *et al.* 2010). The temperature gradient in the asphalt layer in high air temperature areas causes the modulus to increase with depth and induces very high tensile strains at the surface of asphalt pavements with low stiffness (Archilla 2015, Ling *et al.* 2017). One study found that the thermal effect on TDC is negligible compared with the traffic effect under intermediate temperatures (Ling *et al.* 2019), while under harsh climates, thermal effect on TDC is predominant (Roque *et al.* 2010). National Center for Asphalt Technology (NCAT) conducted an experiment in 2015 to study the effect of material properties on TDC. It was found that

the asphalt with high reclaimed asphalt content is more likely to crack prematurely (Chen 2020). In addition, larger air void content, lower percentage of fine aggregate, and lower binder content contribute to faster TDC initiation and propagation (Canestrari and Ingrassia 2020).

The major factors affecting TDC (paving material properties, pavement structure, traffic, and local climate condition) identified above should be considered to accurately model TDC in asphalt pavements. The commonly used TDC models reported in literature can be categorized into four groups based on the fundamental principles adopted: (i) empirical model (ARA Inc. 2004), (ii) Hot-Mix-Asphalt fracture mechanics (HMA-FM) model (Zhang *et al.* 2001, Roque *et al.* 2002, Birgisson *et al.* 2003, Dinegdae *et al.* 2015, Huang *et al.* 2021), (iii) viscoelastic continuum damage (VECD) model (Kutay and Lanotte 2018, Canestrari and Ingrassia 2020), and (iv) Paris' Law model(Luo *et al.* 2016, Ling *et al.* 2017, 2019, 2020, Lytton *et al.* 2018).

The advantage of the empirical model is its simplicity and low computation cost. A mechanistic-empirical (ME) approach was adopted by the NCHRP project 1-37A (ARA Inc. 2004) to model traffic-induced fatigue cracking (BUC and TDC) of asphalt pavements. In this ME model, pavement response is translated into damage by using the enhanced Asphalt Institute's MS-1 fatigue life function that defines the number of traffic load repetitions allowable until failure of asphalt pavements. Pavement performance (length of longitudinal surface crack per mile for TDC and percent of alligator cracking area of total lane area for BUC) is empirically correlated with the calculated accumulative damage by a sigmoidal-shaped transfer function.

HMA-FM was developed by University of Florida research team to study the top-down crack initiation and propagation in asphalt pavements (Zhang *et al.* 2001, Roque *et al.* 2002, Birgisson *et al.* 2003). According to HMA-FM, there is a threshold of dissipated creep strain energy (DCSE) limit for asphalt mixture. The load-induced micro-crack is completely healable if induced DCSE is lower than the threshold, while macro-crack forms if the induced DCSE exceeds the threshold. Dinegdae et al. (Dinegdae *et al.* 2015) developed a mechanics-based top-down crack initiation prediction framework for asphalt pavements based on the enhancement of HMA-FM. The fracture resistance and healing potential of asphalt mixture was characterized by incorporating a morphological parameter (Das *et al.* 2015). Huang et al. (Huang *et al.* 2021) recalibrated Dinegdae's TDC model by a failure curve-based calibration methodology after considering the wheel wander effect of traffic loads.

The viscoelastic continuum damage (VECD) theory is another approach developed to characterize the fatigue cracking potential of asphalt mixture in the last two to three decades. The VECD theory is primarily based on 'elastic-viscoelastic correspondence (E-VC) principle', work potential theory (Schapery 1984), and time-temperature superposition (TTS) principle. The VECD theory assumes material continuous and homogeneous. The damage caused by the formation and development of micro crack is characterized by internal state variables. Therefore, this method is able to identify crack initiation and its location, but not able to characterize the crack propagation process rigorously. Kutay (Kutay and Lanotte 2018) presented a brief history and introduced some commonly used VECD models in the application of fatigue cracking susceptibility

analysis of asphalt mixtures. Roque et al. (Roque *et al.* 2010) integrated VECD and HMA-FM approaches into a unified framework for complete TDC initiation and propagation predictions.

Paris' Law has been widely used to characterize crack growth in fracture mechanics. In fracture mechanics, the J-integral is defined as the strain energy release rate or work per unit fracture surface area, which can be used in Paris' Law for elastic-plastic material. Using J-integral in Paris' Law can appropriately characterize of crack growth in asphalt mixture because it is a visco-elastic-plastic material. To separate viscoelastic energy dissipation from the cracking process, J-integral is replaced with pseudo J-integral in Paris' Law in predicting top-down crack propagation of asphalt pavements (Luo *et al.* 2016). Ling et al. (Ling *et al.* 2020) developed a TDC initiation prediction model using pseudo J-integral based Paris' Law. An empirical regression model was developed using LTPP database to predict crack initiation time based on material properties and pavement structure. Ling et al. (Ling *et al.* 2017, 2019) proposed a traffic-induced TDC propagation model for asphalt pavements using pseudo J-integral-based Paris' Law (Luo *et al.* 2016). The predicted crack depths was empirically correlated with the longitudinal crack length (parallel to the traffic direction) by a sigmoidal-shaped function with two unknown parameters. The above crack initiation and crack growth models were assembled into an unified framework (NCHRP 1-52 model) in NCHRP 1-52 (Lytton *et al.* 2018). However, the authors found that NCHRP 1-52 model underestimated the TDC initiation times in pavement sections with high traffic volume, while over-estimated the TDC initiation times in pavement sections with medium and low traffic volume. To

accurately predict the whole process of TDC initiation and propagation, the initiation model should be adequately rigorous to insure the consequent propagation model to work properly.

The purpose of this paper is to propose a more robust unified mechanics-based framework for TDC initiation and propagation. Our framework improves the robustness of NCHRP 1-52 model by replacing their empirical crack initiation model with a HMA-FM-based crack initiation model. The adopted crack initiation model has been implemented in the new mechanics-based Swedish flexible pavement design (Dinegdae *et al.* 2015, Onifade *et al.* 2017). A modified version of Paris's law-based TDC growth model developed in NCHRP 1-52 (Lytton *et al.* 2018) was adopted to improve the subsequent crack growth prediction. The primary modification to the NCHRP 1-52 model includes the coupling of the HMA-FM-based crack initiation model, and the incorporation of a novel aging model for asphalt mixture.

The rest of the paper is organized as follows. Section 5.2 presents the unified mechanics-based framework for TDC and defines all the sub-models in the framework. Section 5.3 shows the collection of performance data and pavement material properties for the following analysis. Section 5.4 evaluates the performance of the crack initiation model developed in NCHRP 1-52 to indicate the motivation of our framework. We validate the proposed framework in section 5.5. A case study is conducted in section 5.5 to describe the step-by-step procedure for applying the proposed framework. We validate the proposed framework in section 5.6. Finally, we wrap up with a summary and conclusions in section 5.7.

5.2. Development of A Unified Mechanics-based TDC Predictive Framework

5.2.1. General Flow Chart of Developed Framework

A generalized flowchart is presented in Figure 5.1 to illustrate the process and interdependencies of each module in our unified TDC framework for both crack initiation and propagation. The input module and material module contribute to both TDC initiation and propagation sub-frameworks. These modules cover different pavement sections with wide variations in many key factors like dynamic modulus of asphalt concrete layers, resilience modulus of unbound layers, geographical information, climate conditions, and etc. Robust input and material properties modules feed and predict more accurate inputs for the consequent predictive frameworks. The crack initiation time predicted by TDC initiation framework will be passed to TDC propagation framework to indicate when and where the initial macro-crack appears. The TDC propagation framework based on the modified Paris' law predicts the crack depth and pavement failure time when crack growth reaches certain depth. The following subsections present all the models in different modules and predictive frameworks.

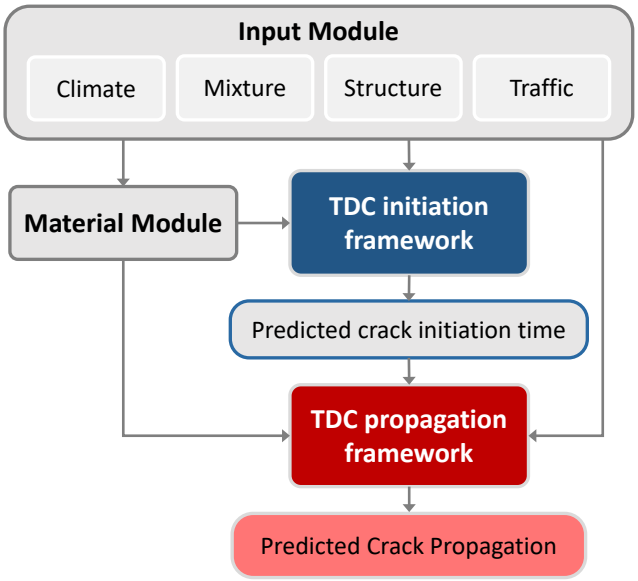

Figure 5.1 Illustration of the process and interdependencies of each module in our unified TDC framework.

5.2.2. Input Module

The input parameters required for the unified framework are divided into four general categories that are mixture, traffic, climate, and pavement structure inputs. These input parameters can be obtained through direct measurements of the associated properties, obtained from an existing database, or predicted using previously developed material prediction models. They are:

- Mixture Inputs: The mixture inputs include the full gradation of aggregates, volumetric properties of the mixture, and the PG-grade of the binder. The mixture input properties are used to calculate the following properties of the asphalt concrete mixture, including the binder G* and phase angle, dynamic modulus of asphalt mixture, asphalt stiffness aging model, the mastic coating thickness, the Dissipated

Creep Strain Energy limit (DCSE_limit), the Healing potential of the asphalt mixture, and the creep strain rate of the asphalt mixture.

- Climate Inputs: The climate inputs are required to predict the temporal and seasonal variations in temperature profiles in the pavement structure. The typical climate inputs include the annual hourly air temperature and the mean annual air temperature (MAAT). The climate inputs are used to predict the hourly temperature variations at different depths in the asphalt concrete layer using a temperature prediction model (Han *et al.* 2011). The hourly variation in pavement temperature profile is used in the material module to predict the changes in the mixture properties, e.g., dynamic modulus and dissipated creep strain energy.
- Pavement Structural Inputs: Pavement structural information is required to accurately represent the pavement structure and the boundary conditions to simulate the actual traffic conditions. The structural information required for the analysis includes the layer thicknesses, Poisson's ratio, modulus of unbound layers, and modulus of the asphalt concrete mixture determined from the material module. The structural information is used in the pavement response module to compute the pavement response due to the application of traffic load. Within the framework, the pavement response, including the stress, strain, and deformation fields in the pavement layers, can be calculated using the Layered Elastic Theory (LET), an open-source Finite Element Method (FEM) algorithm implemented in Python, and a multiphysics simulation software (COMSOL), respectively.

- Traffic Inputs: The traffic inputs are required to account for the influence of the traffic on the long-term performance of the pavement. Two different types of traffic inputs are integrated in our framework that are the hourly traffic volume in equivalent single axle loads (ESALs) and full traffic load spectra. The model can also consider wheel wander of traffic load for more precise characterization of the traffic, when available.

The traffic load spectra model is elaborated since traffic load plays a significant role in TDC initiation and propagation in asphalt pavements. Higher traffic level would increase the rate of accumulation of micro-damage, and therefore, reduce crack initiation time and increase the crack propagation rate (Ling *et al.* 2019). Axle load distribution or axle load spectra is defined as the percentage of axle load repetitions for each type of axle (single, tandem, tridem and quad) within each load interval for each vehicle class (VC). The authors initially employed ESALs as the traffic input in the framework. The prediction results show that the crack propagation module is not sensitive to ESALs, which is consistent with Zhao et al. (Zhao *et al.* 2012) who found that TDC is more sensitive to changes of traffic axle load spectra than BUC and rutting. Therefore, in this study, traffic load spectra is employed instead of ESALs in TDC propagation predictions.

The traffic load spectra model by (Lytton *et al.* 2010, Ling *et al.* 2019, 2020) was developed to characterize the percentage of axle load repetitions for each type of axle (single, tandem, tridem and quad) within each load interval (38 load levels) for each vehicle class (class 4-13). The traffic loads are classified as eight categories based on

vehicle classes (class 4-13), axle types (single, tandem, tridem and quad) and tire configurations (single tire and dual tire). The WIM data, AADTT, or ESALs were collected for each of the studied pavement section, but not all types of traffic data were available for each section. Therefore, two levels of traffic data were defined based on the traffic data availability. WIM data is regarded as the most accurate traffic data and defined as level one, and when WIM data is not available, AADTT or ESALs (defined as level two traffic data) is used.

It should be noted that either AADTT or ESALs cannot be used directly as traffic input. Instead, they should be converted to the same format as WIM data by using default axle load distribution for each load category (Figure 5.2), vehicle class distribution (Table 5.1), and axle configuration for each vehicle class (Table 5.2) (USDOT 2016). For Texas and Swedish sections, AADTT data are available so that they can be converted directly using the default distributions shown in Table 5.1 – 5.3 and Figure 5.2. ESALs were provided for Florida sections; therefore, a linear relationship between AADTT and ESALs was derived using the default traffic distribution before conversion. The tire load is finally converted to tire patch length that is used as one of inputs in TDC propagation sub-framework (Lytton *et al.* 2010, Ling *et al.* 2019, 2020):

$$\text{Tire Lengh } (in.) = \frac{\text{Tire Load } (lb)}{\text{Tire Pressure } (psi) \times \text{Tire Width } (in.)} \quad \textbf{(5.1)}$$

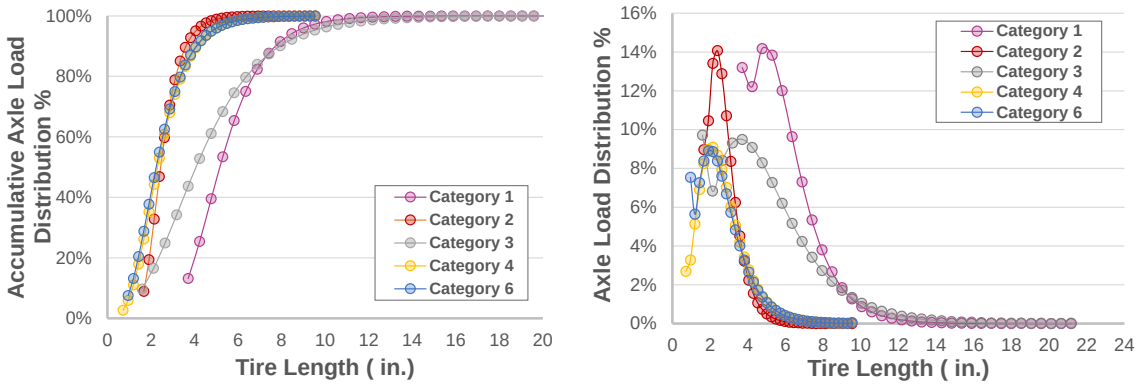

(a) (b)

Figure 5.2 Default (a) axle load distribution and (b) accumulative axle load distribution.

(Only category 1, 2, 3, 4 and 6 are presented because there are no quadrem axle for vehicle class 4-13 and no tridem axle for vehicle class 4-5 according to Table 5.3)

Table 5.1 Distribution of vehicle classes (USDOT 2016).

Vehicle Class	Distribution Factor (%)	Vehicle Class	Distribution Factor (%)
4	1.8	9	31.3
5	24.6	10	9.8
6	7.6	11	0.8
7	0.5	12	3.3
8	5	13	15.3

Table 5.2 Average number of axle for each vehicle class (USDOT 2016).

Vehicle Class	Single Axle	Tandem Axle	Tridem Axle	Quadrem Axle
4	1.62	0.39	0	0
5	2	0	0	0
6	1.02	0.99	0	0
7	1	0.26	0.83	0
8	2.38	0.67	0	0
9	1.13	1.93	0	0
10	1.19	1.09	0.89	0
11	4.29	0.26	0.06	0
12	3.52	1.14	0.06	0
13	2.15	2.13	0.35	0

Table 5.3 Categories of traffic load (Lytton *et al.* 2010).

Vehicle Class	Single Axle	Tandem Axle	Tridem Axle	Quad Axle
4	1	3	5	7
5				
6		4	6	8
7				
8	2			
9				
10				
11				
12				
13				

(Shaded areas are axles using single tire; unshaded areas are axles using dual tires)

5.2.3. Material Module

5.2.3.1. Predictions of Asphalt Aging

Accurate characterization of the aging of asphalt mixtures is important for predicting the changes in the short-term and long-term stiffness of asphalt mixtures. As shown in Figure 5.3, asphalt binder aging can generally be divided into two stages: short-term aging and long-term aging. Short-term aging occurs during asphalt mixing, transportation, and pavement laydown and involves volatilization and oxidation processes, while long-term aging is due to oxidation after pavement laydown during the entire service life of asphalt pavements. As the asphalt binder ages, it becomes stiffer and more brittle due to the change of chemical composition (Sirin *et al.* 2018), which causes asphalt pavement more prone to cracking-related distresses such as TDC and BUC.

Zhang. et al. (Zhang *et al.* 2019a, 2019b) developed aging models for characterizing short-term and long-term aging of asphalt mixture. The rheological activation energy

was used to capture binder resistance to viscous flow in the short-term aging model. The kinetics-based approach was employed to capture the oxidation process and temperature sensitivity in the long-term aging model. In addition, the primary structure coating thickness (Lira *et al.* 2013, Yideti *et al.* 2013, Dinegdae *et al.* 2015, Onifade *et al.* 2017), which quantifies the asphalt mastic coating thickness around the load-bearing structure of asphalt mixture, was incorporated into the long-term aging model to capture the effect of mixture morphology on the oxidation process.

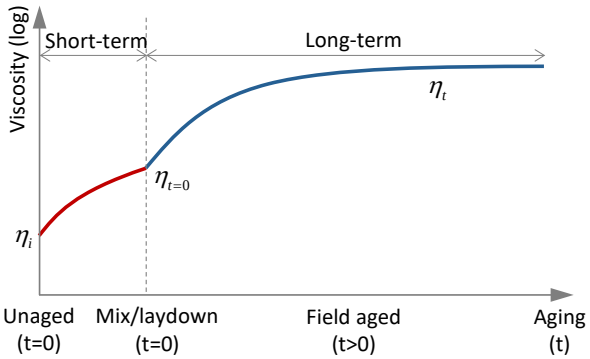

Figure 5.3 Entire aging evolution of asphalt pavement in terms of binder viscosity (Zhang *et al.* 2019a).

Formulation of the short-term aging model (Zhang *et al.* 2019a) is given by:

$$\ln \eta_{t=0} = \ln \eta_i + a_s E_{ar(i)} + b_s + \frac{k_s E_{ar(i)} + t_s}{RT_R} \quad \textbf{(5.2)}$$

where $\eta_{t=0}$ is short-term aged viscosity corresponding to laydown condition; η_i is unaged viscosity; $E_{ar(i)}$ is rheological activation energy of unaged asphalt binder; T_R is test temperature at which the viscosity is measured; R is the universal gas constant; a_s, b_s, k_s,

and t_s are four model coefficients, which are 0.011327, -2.94272, -0.035330, and 11.009737, respectively.

The long-term aging model (Zhang *et al.* 2019b) is expressed as a sum of short-term aged viscosity and an age-hardening increment in a nature logarithm form:

$$\ln \eta_{aged} = \ln \eta_{t=0} + \Delta \ln \eta_l (t) \quad \textbf{(5.3)}$$

where $\Delta \ln \eta_l (t)$ is hardening increment due to long-term aging as a function of aging time *t*; subscript "*l*" stands for long-term aging.

The hardening increment term is used to characterize the field oxidative aging and includes three components representing the aging evolution, temperature sensitivity and morphology dependency, respectively. The long-term aging model can then be finalized as follows:

$$\ln \eta_{aged} = \ln \eta_{t=0} + \left[a_l + b_l \left(t_p \right)^{c_l} \right] \cdot \left[\ln A_{ar(s)} + \frac{E_{ar(s)}}{RT_R} \right] \cdot \left[k_l \left(\frac{E_{ac}}{E_{af}} \right)^{m_l} \left(1 - e^{-k_{af} t} \right) + k_{ac} t \right], \quad b_l < 0 \quad \textbf{(5.4)}$$

where η_{aged} is long-term aged viscosity; $k_{af} = A_{af} e^{-\frac{E_{af}}{RT_a}}$; $k_{ac} = A_{ac} e^{-\frac{E_{ac}}{RT_a}}$; $A_{ar(s)}, E_{ar(s)}$ are the pre-exponential factor and rheological activation energy of short-term aged binder, respectively; t_p is PS coating thickness;; a_l, b_l, c_l, k_l, m_l are model coefficients; and *t* is aging time.

The dataset used for verifying the short-term and long-term aging model coefficients included 420 and 408 pavement sections from the USA and Canada in LTPP (Long Term Pavement Performance) database (Zhang et al., 2019a, 2019b).

5.2.3.2. Predictions of Dynamic Modulus and Phase Angle of Asphalt Binder

The Onifade and Birgisson Model (Onifade and Birgisson 2020) was used in this study to predict asphalt binder dynamic shear modulus, and phase angle from conventional steady-state viscosity for unaged and aged conditions. A suitable form of the generalized logistic function was employed in the model to capture the asymptotic behavior of asphalt binders under a wide range of temperature conditions. 7120 data points, including unmodified and modified binders, were used in the model development and verification. In the development of this model, the dynamic shear modulus and phase angle predictive model were developed for unmodified and modified binders separately. The dynamic shear modulus model for unmodified/modified binders (Onifade and Birgisson 2020) is expressed as:

$$\log\left|G_b^*\right| = \left[a_1 + \frac{a_2}{1 + a_3 \cdot e^{\left(a_4 \cdot \log(\eta \cdot \omega)\right)}}\right] \cdot \left(-VTS\right)^{0.58} \quad \textbf{(5.5)}$$

where $\left|G_b^*\right|$ is the dynamic shear modulus (psi); η is the steady-state viscosity in (MegaPoise); *VTS* is the regression slope of the Viscosity Temperature Susceptibility plot; ω is the angular frequency in (rad/sec) and 62.8 rad/sec was used in this study to similate the tire load with highway traffic speed; a_1-a_4 are model coefficients and the nonlinearly optimized results are presented in (Onifade and Birgisson 2020).

The phase angle model for unmodified/modified binder (Onifade and Birgisson 2020) is given by

$$\delta_b = \frac{\log\left|G_b^*\right|_{ref}}{b_1 \cdot e^{\left(b_2 \cdot \log\left(\eta \cdot \omega^{0.7}\right)\right)} + b_3 \cdot e^{\left(b_4 \cdot \log\left(\eta \cdot \omega^{0.7}\right)\right)}} \quad \textbf{(5.6)}$$

where δ_b is the phase angle; $\left|G_b^*\right|_{ref}$ is the reference dynamic shear modulus (evaluated using Eqn. 5.5 at a reference temperature of -96 ^{o}C), and the single-valued viscosity shift factor is set to be 0.7; b_1-b_4 are model coefficients and the nonlinearly optimized results are presented in (Onifade and Birgisson 2020).

The predicted dynamic modulus and phase angle of asphalt binder will be used as the input parameters in the prediction of dynamic modulus of HMA using Witczak 2006 model (Bari 2005) detailed in the next section.

5.2.3.3. Prediction of Dynamic Modulus of Hot Mix Asphalt (HMA)

The most widely used dynamic modulus models for asphalt mixture are Witczak 1999 model and Witczak 2006 model (Witczak and Fonseca 1996, Bari 2005). Compared with Witczak 1999 model (Witczak and Fonseca 1996), the advantage of Witczak 2006 model (Bari 2005) is the adoption of the binder dynamic shear modulus and phase angle, thereby directly accounting for the frequency-dependent behavior of asphalt binders. Therefore, Witczaks's 2006 dynamic modulus model was adopted in this study.

Figure 5.4 presents the workflow of HMA dynamic moduli prediction using the Witczak 2006 model, combined with the short-term and long-term aging models, and the dynamic shear modulus and phase angle models of asphalt binder obtained from the Onifade and Birgisson model. The output will be input into the crack initiation and propagation models detailed in the next two sections.

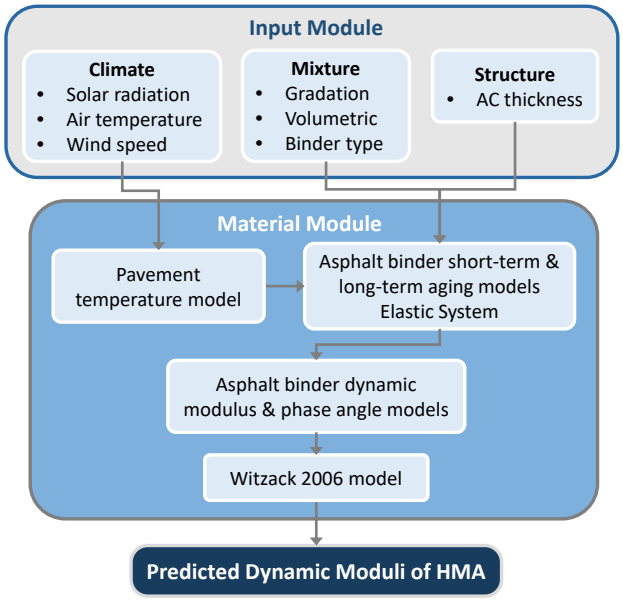

Figure 5.4 Workflow of HMA dynamic modulus prediction.

5.2.3.4. DCSE Limit and Accumulated DCSE

The framework considers the effect of oxidative aging on the predicted properties of the asphalt mixtures and the effects of healing on micro-damage recovery. It also considers the effect of different climatic regions on pavement performance by introducing a new temperature prediction model (Han *et al.* 2011). The changes in all key material properties due to aging, pavement temperature gradient, and varying temperature profiles (Zhang *et al.* 2019a, 2019b) are considered. The prediction of asphalt aging without adequate consideration of the mixture morphology might lead to erroneous conclusions (Das *et al.* 2015). Therefore, in this study, an asphalt mixture morphology model (Das *et al.* 2015) was employed to relate the asphalt mixture aging to the key material properties (i.e. aggregate packing, air void, porosity and level of compaction). The Dissipated Creep Strain Energy Limit (*DCSE*_lim) is a threshold derived from the HMA-FM that determines the upper limit for macro-crack initiation in asphalt mixtures.

The *DCSE*_lim is related to PS coating thickness (t_p) and age according to experimental observations on a variety of asphalt mixtures using the SuperPave indirect tension tests (Das *et al.* 2015, Dinegdae *et al.* 2015). The *DCSE*_lim of unaged and aged asphalt mixture are given as:

$$DCSE\_\lim_t = k_1 * (\frac{1}{t_p})^{k_2} * (\frac{\ln \eta_i}{\ln \eta_{aged}}) \quad \textbf{(5.7)}$$

where *i* and *t* stand for 'initial' and aging time, respectively; η_{aged} and η_i are aged steady-state viscosity at time *t* (in years) and initial unaged steady-state viscosity of asphalt binder under reference temperature (25°C), respectively; t_p is PS coating thickness; k_1 and k_2 are material-specific parameters given as k_1 = 15.5 and k_2 = 3.35. The healing potential (Dinegdae *et al.* 2015) of the asphalt mixture based on the asphalt mixture morphology is given as:

$$h_{ym}(t) = 1 - ([\exp(\frac{t_p}{t})^{-DCSE_i}]_{norm})^{k} \quad \textbf{(5.8)}$$

where t_p is PS coating thickness; *k* is a factor depending on the traffic volume; *t* is time in years. As can be seen from Eqn. 5.8, asphalt mixtures with higher PS coating thickness exhibit more capacity to heal and recover induced damage.

The accumulated damage induced per loading cycle ($ACSE_L$/cycle) is computed by considering maximum surface tensile stress, creep strain rate, and hourly traffic expressed as (Dinegdae *et al.* 2015):

$$ACSE_L/cycle = \int_0^{0.1} \sigma_{AVE} * \sin(10\pi t) * \dot{\varepsilon}_{p\max} * \sin(10\pi t)\,dt \quad \textbf{(5.9)}$$

where σ_{AVE} is the averaged stress within the zone being analyzed and $\dot{\varepsilon}_{p\max}$ is creep strain rate.

Taking into account of healing, the accumulated creep strain energy that is not healed is expressed as (Dinegdae *et al.* 2015):

$$ACSE_{remain}(t) = ACSE_{accum}(t) * (1 - h_{ym}(t)) \quad \textbf{(5.10)}$$

5.2.4. TDC Initiation Framework

The mechanics-based crack-initiation analysis framework predicts the initiation of fatigue cracking in asphalt pavements, including both top-down and bottom-up cracking initiation (Dinegdae *et al.* 2015). In this study, the crack-initiation analysis framework was coupled with the crack growth model developed under NCHRP 1-52 (Lytton *et al.* 2018). Specifically, the first part of the framework was implemented for calculating the initiation of top-down cracking of flexible pavements, and then the predicted crack initiation time was used as an input in the modified NCHRP 1-52 top-down crack growth model. The outline of the TDC initiation framework is summarized in Figure 5.5. The underlying criterion for the initiation of top-down cracking is based on an extension of HMA-FM (Zhang *et al.* 2001, Roque *et al.* 2002, Birgisson *et al.* 2003). The HMA-FM identifies an energy threshold representing the resistance of asphalt mixtures to the initiation of fracture. Below the energy threshold, induced damage due to micro-cracking and micro-void formation are healable. Above the threshold, damage is non-healable and result in macro-crack formation, propagation, and eventually failure of pavement.

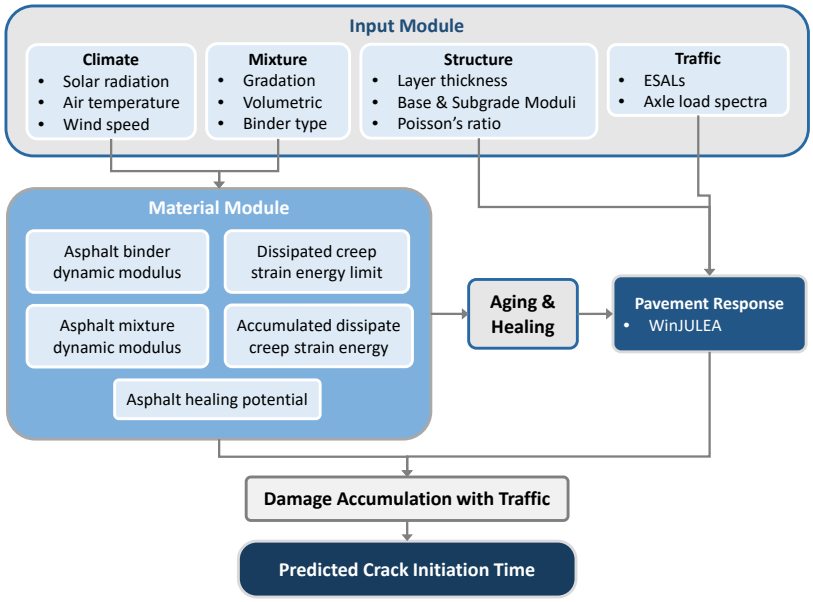

Figure 5.5 Flowchart of TDC initiation framework.

The limiting condition for crack initiation is assessed through continuous evaluation of the remaining Accumulated Creep Strain Energy (*ACSE*) and the Dissipated Creep Strain Energy (*DCSE*) densities limit of the material. When the remaining *ACSE* exceeds the *DCSE*_lim, a macro-crack initiates. The critical condition for macro-crack initiation is expressed as (Dinegdae *et al.* 2015):

$$CI(t) = ACSE_{remain}(t) - DCSE_{\lim}(t) \quad \textbf{(5.11)}$$

where *CI* is the crack initiation, and *t* designates the evolution of the energy densities with time.

5.2.5. TDC Propagation Framework

A modified version of Paris's law-based TDC growth model developed in NCHRP 1-52 (Lytton *et al.* 2018) was adopted to improve the subsequent crack growth prediction. The primary modification to the original crack growth model developed in NCHRP 1-52

project is the incorporation of a novel aging model for asphalt mixture. The pseudo J-integral-based Paris' Law is expressed as:

$$\frac{dc}{dN} = A'(\Delta J)^{n'} \tag{5.12}$$

Where ΔJ is the J-integral computed by an Artificial Neural Network (ANN) model (Ling *et al.* 2017), A' and n' are the fracture parameters obtained a regression model from (Luo *et al.* 2016). The developed ANN model considers modulus gradient of the asphalt layer, moduli of base/subbase and subgrade layers, pavement structure, non-uniform tire load pattern (De Beer *et al.* 1997, Ling *et al.* 2017), and load locations. The flowchart of the TDC propagation framework is shown in Figure 5.6.

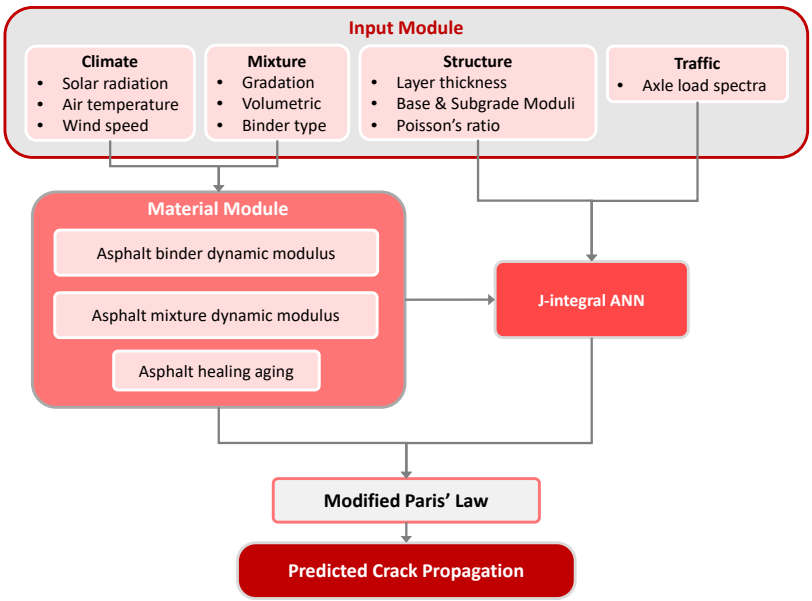

Figure 5.6 Flowchart of TDC propagation framework.

The truck tire-pavement contact stress is non-uniformly distributed along three directions, namely, longitudinal, vertical and transverse directions. The contact stresses

in three directions correspond to three different fracture modes, including sliding mode under vertical stress, opening or tensile mode under transverse stress and tearing mode under longitudinal stress (Luo *et al.* 2018). The tire load considered in the ANN model includes three components: vertical stress, transverse stress, and longitudinal stress. The distribution of each stress component follows Beer's work (De Beer *et al.* 1997). The shape of the tire contact area is simplified to be rectangular (Lytton *et al.* 1993). The input variables of the ANN model includes the thickness of each pavement layer, crack depth, surface modulus gradient (*n*, *k*), modulus of each pavement layer.

Luo et al. (Luo *et al.* 2016) developed a regression model for predicting fracture coefficients (A' and n') through performance-related material properties. The dynamic uniaxial tensile test data, controlled-strain RDT test data, and overlay test data collected from different sources were used in the multiple regression analysis. The parameters n' and A' are expressed as:

$$n' = -16.052 + 0.135AV\% + 6.500\ln\left(AB\%\right) + 8.147\psi + 5.512\frac{1}{m} - 81.515\left(\frac{1}{E_1}\right)^m \quad \textbf{(5.13)}$$

$$A' = 10^{-(1.246n'+3.615)} \quad \textbf{(5.14)}$$

where *AV*% is air void content, in %; *AB*% is asphalt binder content by weight of the mixture, in %; ψ is the aggregate gradation shape parameter; E_1 and *m* are relaxation modulus parameters, in MPa. Relaxation modulus is affected by oxidative aging so that the fracture parameters (A' and n') is also aging dependent. The power function of the relaxation model is (Luo *et al.* 2016):

$$E(t) = E_1 t^{-m} \quad \textbf{(5.15)}$$

where $E(t)$ is the relaxation modulus of asphalt mixtures, and E_1 and m are relaxation modulus parameters used to calculate the fracture coefficient n'.

As we mentioned, dynamic modulus gradient of asphalt mixture plays an important role in top-down crack propagation. The equations below are used to model dynamic modulus gradient (Ling *et al.* 2017):

$$E(z) = E_d + (E_0 - E_d)\left(\frac{d-z}{d}\right)^N; \quad K = \frac{E_0}{E_d} \tag{5.16}$$

where $E(z)$ is modulus at depth z; E_0 and E_d are moduli at surface and bottom of the asphalt layer, respectively; d is the thickness of asphalt layer; N and K are model parameters used as input of the J-integral ANN model. Table 5.4 provides the input variables for the TDC propagation framework.

Table 5.4 Summary of Input Variables for the Top-down Crack Propagation Framework.

Category	Name
J-integral ANN	Asphalt layer thickness (in.)
	Base layer thickness (in.)
	Subgrade layer thickness (in.)
	Crack depth (mm)
	Surface modulus gradient (n, k)
	Surface modulus (ksi)
	Base modulus (ksi)
	Subgrade modulus (ksi)
Traffic	Yearly ESALs
Environment	Mean Annual Average Temperature (C°)
Dynamic modulus model	Aggregate gradation
	Percent of air void (%)
	Effective binder content (%)
	Void in Mineral aggregate (%)
	Binder content (%)
	A
	VTS
	Primary structure coating thickness (mm)
Crack initiation prediction model	Crack initiation time (yrs)

5.3. Data Collection

To evaluate the performance of the proposed unified framework, eighteen field test sections were investigated as a part of this study. These include eleven pavement sections from the State of Florida, three Long Term Pavement Performance Sections (LTPP) sections from the State of Texas, and four pavement sections from Sweden (Dinegdae *et al.* 2015, Göransson 2020, LTPP InfoPave 2020). The binder types, mix design procedures, mix volumetrics, traffic, climate, and overall pavement design varied across these sections.

The performance history (i.e. crack initiation and propagation) of the field sections are necessary to evaluate and validate the prediction accuracy of the proposed framework.

The observed crack initiation and failure times of Florida sections were converted from crack rating (CR) ranging from 0 to 10 (Dinegdae *et al.* 2015). A CR of 10 indicates that the pavement is intact with no cracks, and a reduction in CR implies the presence of microcracks or propagation of macro cracks depending on the level of the CR. Specifically, the CR values of 8 and 6.4 indicate TDC initiation and failure, respectively (Roque *et al.* 2010). The longitudinal wheel-path crack length is recorded with three severity levels (i.e. low, medium and high) according to the crack width in LTPP database. The longitudinal crack data with Medium and high severity levels are barely recorded because once the medium severity level reaches, the longitudinal cracks would possibly intersect with transverse cracks and therefore be reported as alligator cracking. Crack initiation and failure times for the LTPP sections were converted from the field measured longitudinal wheel-path crack length at the first appearances of low and medium severity level cracks, respectively. On the other hand, crack index is used to evaluate the cracking severity level for Sweden sections. A crack index of 150 is defined as crack initiation. The measurement of crack index stopped when failure occurs to the pavements (Göransson 2020).

In addition to the performance history data, the laboratory characterizations (i.e. aggregate gradation, binder properties, volumetrics, and mechanical properties of the mixtures) are also available for each of these sections. The input data used to predict TDC initiation and propagation of the proposed framework are summarized in the appendix A.

5.4. Evaluation of NCHRP 1-52 Model

This section evaluates the performance of the crack initiation model developed in NCHRP 1-52. Figure 5.7 compares the measured with the predicted crack initiation time using NCHRP 1-52 model. In Figure 5.7(a), NCHRP 1-52 model generally over-predicted TDC initiation time in the sections with medium to low traffic volume, while under-predicted TDC initiation time in the sections with high traffic volume. The average deviations of the predicted results from the field measurements are 19.29 years and 4.37 years for medium-to-low traffic sections and high-traffic sections, respectively. Therefore, significant high relative error shown in Figure 5.7(b) indicates that developing a more reliable TDC initiation model is urgently needed to improve the performance of the consequent NCHRP 1-52 crack propagation model.

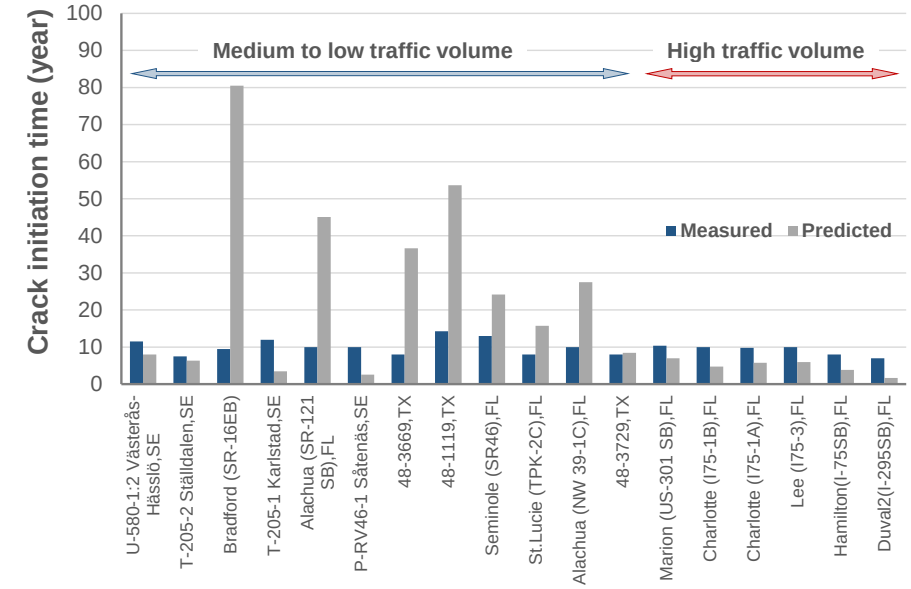

(a)

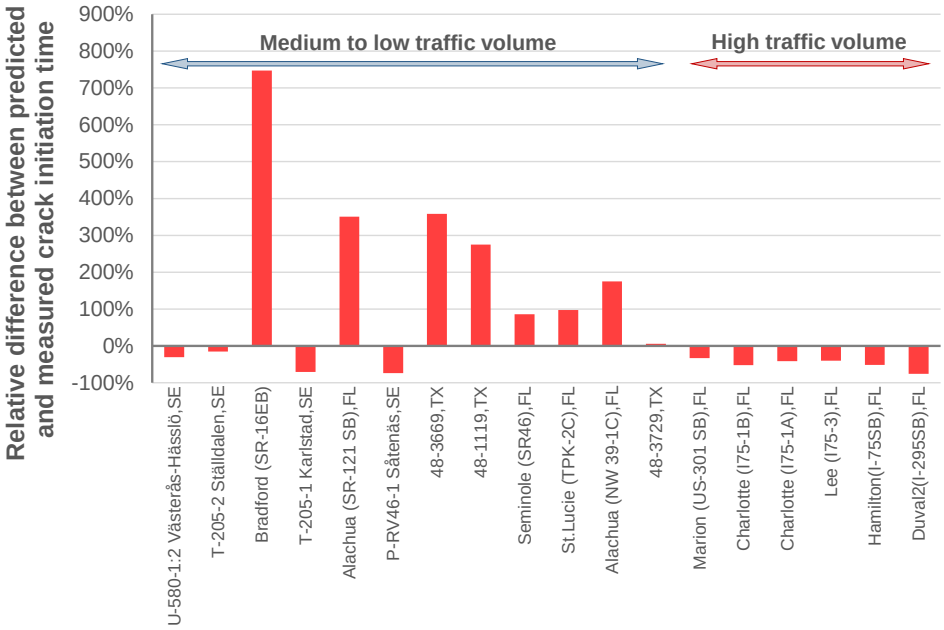

(b)

Figure 5.7 Comparison between observed and predicted crack initiation times using NCHRP 1-52 model: (a) measured and predicted initiation time; (b) relative difference between measured data and predicted results (positive values indicate over-predicted and negative values under-predicted).

5.5. A Case Study

A step by step procedure of applying the proposed framework to the prediction of crack initiation and failure times of flexible pavements is summarized in this section using the input data for Florida section St.Lucie (TPK-2C) as an example.

Step 1: Collect the input data.

The input data required can be divided into seven categories including traffic, pavement structure, environment asphalt mixture gradation and volumetrics, asphalt binder information, and asphalt mixture fracture energy parameter, as shown in Table 5.5 and Figure 5.8.

Table 5.5 Input data of Florida pavement section St.Lucie (TPK-2C).

Category	Name	Value
Traffic	ESALs_yearly	166000
	Coring year	10
	Percent Truck	0.123
	Track factor	1.03
Pavement Structural Information	Depth of AC layer (in.)	6.1
	Depth of Base layer (in.)	12
	Depth of Subbase Layer (in.)	12
	Base Modulus (ksi)	34
	Subbase Modulus (ksi)	19
	Subgrade Modulus (ksi)	24
Environment	MAAT (°F)	75
	Reference temperature (°F)	50
Volumetrics	Aggregate Gradation	Figure 5.8
	Air-void content (Va)	4.55
	Effective binder content (Vbe)	10.71
	Void in Mineral Agg. (VMA)	15.26
	Binder content (Pb)	5.23
Asphalt Binder	Binder type	PG 67-22
	A	10.6316
	VTS	-3.548
Fracture Energy Parameter	Primary Structure coating thickness (mm)	0.956

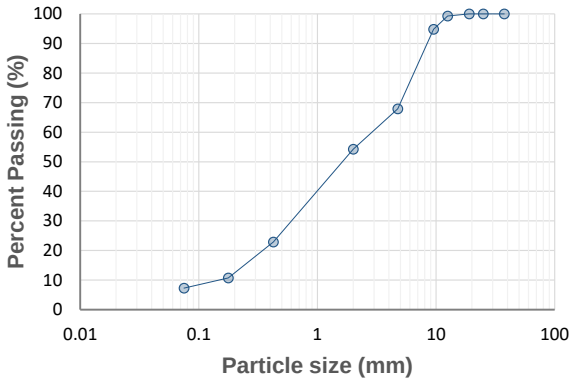

Figure 5.8 Aggregate gradation of asphalt mixture for Florida pavement section St.Lucie (TPK-2C).

Step 2: Determine dynamic modulus of asphalt mixture at different depths in asphalt layer(s).

Pavement temperature at different depths is first predicted by a new temperature model (Han *et al.* 2011) in order to capture the climate effect on pavement performance, as shown in Figure 5.9. It is assumed that the temperature variation keeps the same pattern each year. Then the aforementioned short-term and long-term aging model (Zhang *et al.* 2019b, 2019b) (Eqn. (5.2 – 5.4)) is employed to predict the aged viscosity of asphalt binder, which is then used in Onifade and Birgisson Model (Onifade and Birgisson 2020) (Eqn. (5.5 – 5.6)) to predict dynamic modulus and phase angle of asphalt binder. Finally, hourly dynamic modulus of HMA at four different depths in the asphalt layer are predicted by Witczak 2006 model (Bari 2005), as shown in Figure 5.10.

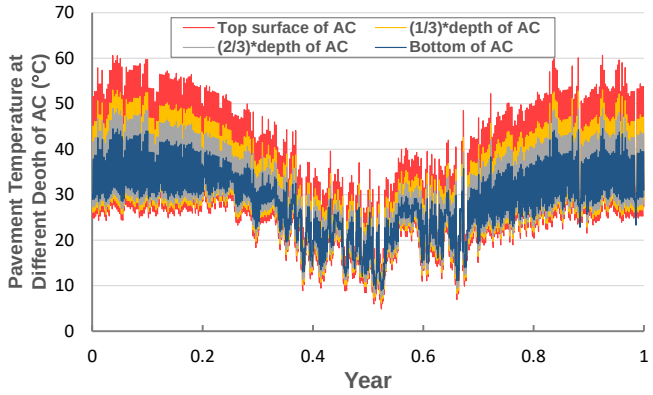

Figure 5.9 Predicted hourly pavement temperature at different depths of AC in a year for Florida section St.Lucie (TPK-2C).

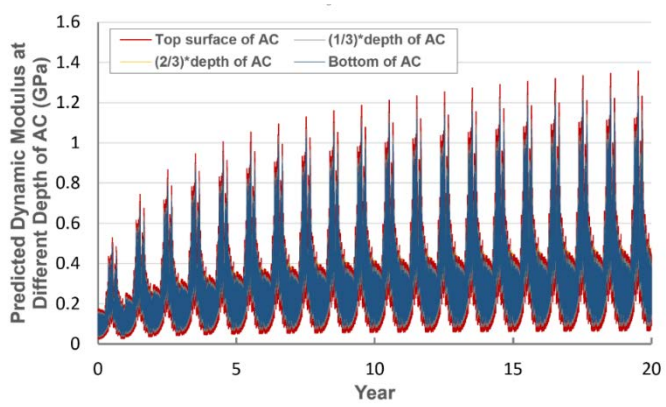

Figure 5.10 Predicted dynamic modulus of AC at different depths in asphalt layer for Florida section St.Lucie (TPK-2C).

Step 3: Predict top-down crack initiation time of asphalt pavement.

The PS coating thickness (t_p) is first determined by a morphology model (Das *et al.* 2015) which is correlated with *DCSE*_lim that determines the initiation of maro-cracks of asphalt mixture. Then Eqn. (5.7 – 5.11) can be used to calculate top-down crack initiation time. Top-down crack initiates when Accumulated Creep Strain Energy (*ACSE*) is equal to *DCSE*_lim. As shown in Figure 5.11, the predicted crack initiation year is 9.2.

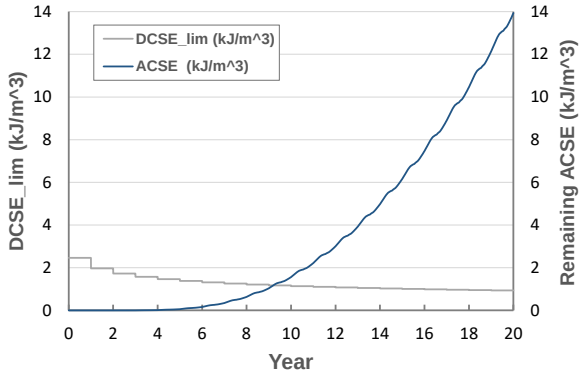

Figure 5.11 Predicted remaining *ACSE* and *DCSE_lim* with time for Florida section St.Lucie (TPK-2C).

Step 4: Determine dynamic modulus master curve of asphalt mixture.

The dynamic modulus of asphalt mixture are predicted at different temperatures and frequencies to obtain dynamic modulus master curve. To simplify the calculation, the aging condition at crack initiation time is used in generating the input data for constructing dynamic modulus master curve of asphalt mixture. The constructed dynamic modulus master curve (Figure 5.12 (a)) is then converted to relaxation modulus using 11-term Prony Series. The obtained relaxation modulus curve is fitted by power function to determine the multiplier and exponent of 1360.4 MPa and -0.205, respectively.

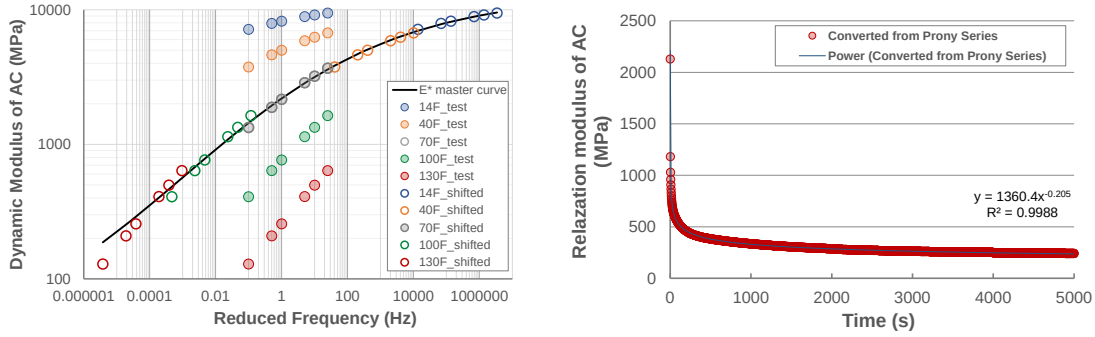

(a) (b)

Figure 5.12 (a) Predicted dynamic modulus master curve and (b) converted relaxation modulus of asphalt mixture for Florida section St.Lucie (TPK-2C).

Step 5: Determine aggregate gradation characteristic parameters for asphalt mixture.

The aggregate gradation data is also fitted by power function to obtain the aggregate gradation shape factor ψ, which is 0.2944 as shown in Figure 5.13.

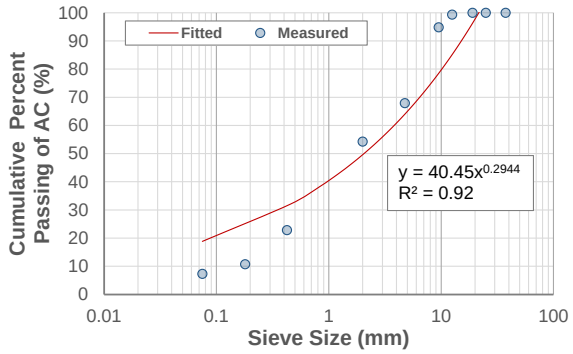

Figure 5.13 Fitting result of aggregate gradation of asphalt mixture for Florida section St.Lucie (TPK-2C).

Step 6: Determine fracture coefficients.

The fracture coefficients (A' and n') can be calculated using the regression model (Eqn. (5.13 – 5.14)) developed by Xue et al. (Luo *et al.* 2016) based on the parameters calculated in step 4 and 5. The calculated A' and n' are 6.03 and 7.42e-12, respectively.

Step 7: Determine dynamic modulus gradient parameters (*N* and *K*).

Eqn. (5.16) is used to fit the predicted hourly dynamic modulus of asphalt mixture at different depths, and the fitted model parameters *N* and *K* are plotted in Figure 5.14.

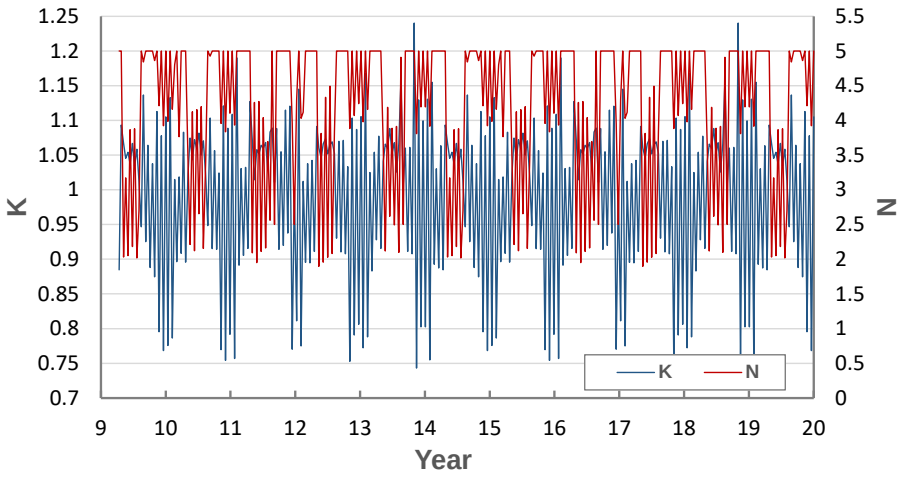

Figure 5.14 Predicted dynamic modulus gradient parameters (*N* and *K*) with time for Florida section St.Lucie (TPK-2C).

Step 8: Determine traffic loads using the presented load spectra model.

Since the traffic data provided for Florida sections are ESALs, it should be converted to the same format as WIM data by using the default axle load distribution (Figure 5.2), vehicle class distribution (Table 5.1), and axle configuration for each vehicle class (Table 5.2) before being used in the prediction of top-down crack propagation. Tire length is calculated using Eqn. (5.1) which is used as one of eight inputs for J-ANN model for predicting J-integral.

Step 9: Determine J-integrals at the crack tip in asphalt layers.

The J-integral is computed by the ANN model developed by Ling et al. (Ling *et al.* 2017). The inputs of the ANN model are dynamic modulus of asphalt layers, moduli of base and subgrade, thicknesses of AC and base, dynamic modulus gradient parameters (*N* and *K*), and crack depth updated at each time step. The outputs of the ANN model are a total of six J-integrals under single tires with tire lengths of 64 mm, 305 mm, and 406 mm, and dual tires with the tire lengths of 64 mm, 127 mm, and 229 mm. Since the load spectra is used in the top-down cracking predictions, the J-integrals caused by the tire loads other than the predicted six should be acquired by interpolation. The calculation of J-integral is started after crack initiation predicted by the TDC initiation framework. The crack depth at the time of crack initiation is set to be 7.5 mm. The ANN predicted J-integral under current crack depth, current modulus of each layer under a specific tire load level is used in Paris' Law (Eqn. (5.12)) to calculate the crack depth increment. The calculated crack depth increment under each tire load in the current time step is added to the total crack depth obtained in the last time step. The J-integrals are updated every four hours to enhance the efficiency without the loss in accuracy. Figure 5.15 (a) shows the ANN predicted J-integrals under six different tire loads for 20 years. The predicted crack growth is plotted in Figure 5.15 (b). For Florida section St.Lucie (TPK-2C), the predicted failure time is 14.2 years with the defined failure threshold of 16 mm.

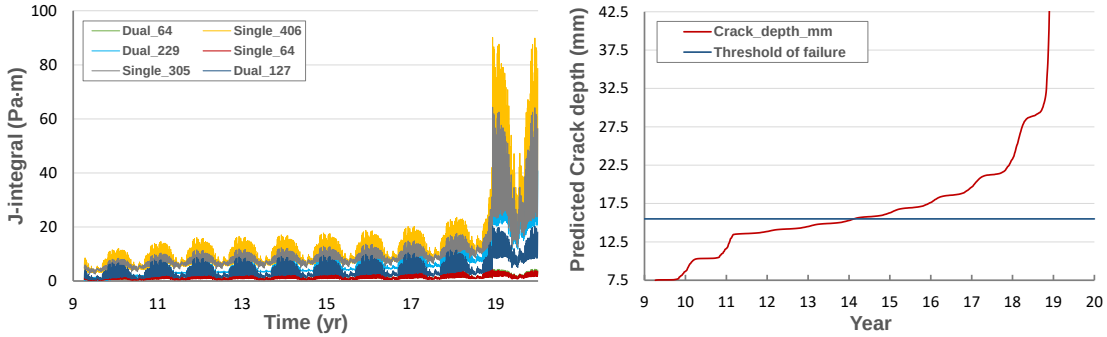

(a) (b)

Figure 5.15 (a) ANN predicted J-integrals due to different tire loads for single and dual tires and (b) Predicted crack growth for Florida section St.Lucie (TPK-2C).

Step 10: Compare the modelling results with field measurements.

Figure 16 shows the CR history of the Florida pavement section St.Lucie (TPK-2C). Recall that CR values of 8 and 6.4 were defined as the indicators of top-down crack initiation and failure, respectively (Roque *et al.* 2010). Thus, the measured crack initiation and failure times for section St.Lucie (TPK-2C) are 8 and 13 years, respectively. According to the results presented in Figures 5.11 and 5.15(b), the predicted crack initiation and failure time are 9.2 and 14.2 years respectively. For the St.Lucie (TPK-2C) section, the predicted results are in good agreement with the field observation.

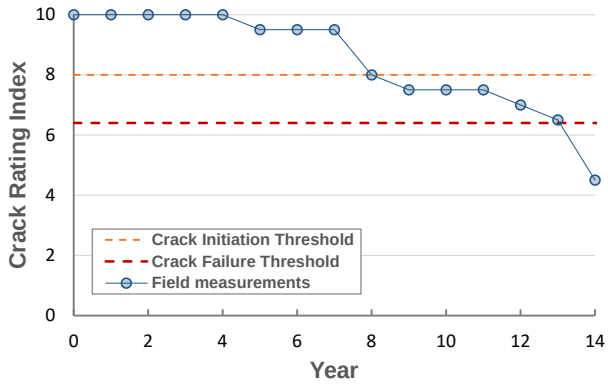

Figure 5.16 CR history of Florida section St.Lucie (TPK-2C).

5.6. Long-term TDC Prediction

This section presents the predictions by our unified framework for crack initiation and propagation using the same dataset mentioned in the previous section. These results and comparisons with the measured data validates the proposed framework. Figure 5.17 shows the observed and predicted crack initiation times using HMA-FM-based crack initiation model. The average deviation of the predicted results from the field measurements is 1.36 years with the minimum and maximum deviations of 0.25 and 3.56 years. The HMA-FM-based crack initiation model outperforms the NCHRP 1-52 model by achieving much smaller deviations from the field measurements. The predicted crack initiation times were then adopted as the starting point of crack propagation prediction. The crack depth at crack initiation time was set to be 7.5 mm according to Lytton et al. (Lytton *et al.* 1993, 2018). Table 5.6 presents all the calculated fracture coefficients and performance-related material properties for the selected pavement sections. A' and n' were calculated using the regression function in Eqns. (5.13 – 5.14). E_1 and m were calculated using Eqn. (5.15), and the aggregate gradation shape factor ψ is calculated by fitting aggregate gradation data with power function.

Table 5.6 Fracture Coefficients and Performance-related Material Properties.

Section Name	Fracture Coefficients		Performance-Related Material Properties		
	A'	n'	E_1 (MPa)	m	ψ
Florida source					
Charlotte (I75-1A),FL	2.32E-13	7.24	1389.55	0.21	0.28
Charlotte (I75-1B),FL	3.60E-14	7.89	1525.28	0.21	0.28
Lee (I75-3),FL	5.03E-14	7.77	1286.78	0.21	0.30
Hamilton(I-75SB),FL	3.78E-12	6.27	958.38	0.20	0.33
Marion (US-301 SB),FL	3.82E-13	7.06	1196.48	0.21	0.29
Duval2(I-295SB),FL	2.46E-15	8.82	1817.62	0.21	0.31
St.Lucie (TPK-2C),FL	7.42E-12	6.03	1360.41	0.20	0.29
Alachua (NW 39-1C),FL	1.23E-11	5.86	995.42	0.21	0.32
Seminole (SR46),FL	3.10E-13	7.14	1478.92	0.22	0.27
Alachua (SR-121 SB),FL	7.90E-14	7.61	1500.58	0.21	0.29
Bradford (SR-16EB),FL	3.12E-13	7.14	1189.80	0.21	0.30
Sweden source					
T-205-1 Karlstad,SE	6.89E-07	2.04	565.04	0.18	0.43
U-580-1:2 Västerås-Hässlö,SE	5.08E-07	2.15	578.56	0.18	0.43
P-RV46-1 Såtenäs,SE	5.77E-07	2.11	572.94	0.18	0.43
T-205-2 Ställdalen,SE	7.12E-07	2.03	563.55	0.18	0.43
LTPP source					
48-3669,TX	1.06E-10	5.10	935.01	0.19	0.25
48-1119,TX	4.87E-11	5.38	847.35	0.20	0.34
48-3729,TX	6.68E-11	5.26	850.35	0.19	0.31

Figure 5.18 shows a comparison of the observed and predicted failure times for the 18 pavement sections. The failure was set as when the crack depth reaches 16 mm. Similarly, the average deviation of predicted pavement failure from the field measured results are 1.19 years with the minimum and maximum deviations of 0 and 3 years. The maximum deviation can be observed in Bradford (SR-16EB), FL with measured and predicted failure times of 13 and 16 years, respectively. The field measurement of crack rating index ended at year 11 with CR value of 7 which is larger than the threshold of failure (6.4). Since the actual failure time cannot be obtained through direct field

observation, the failure time used for the Bradford (SR-16EB), FL section was extrapolated and determined to be 13 years.

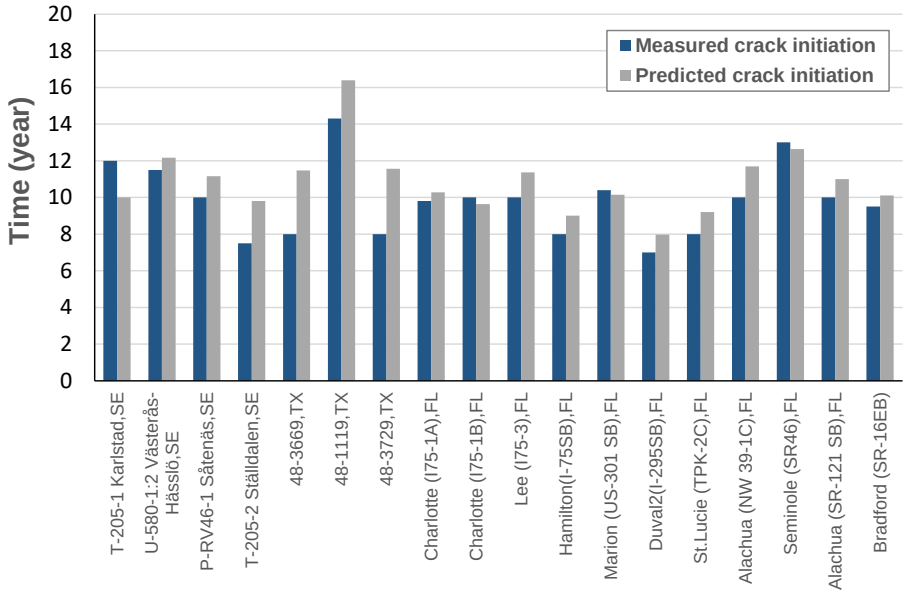

Figure 5.17 Comparison between observed and predicted crack initiation times for Swedish, Florida, and Texas pavement sections used in the study.

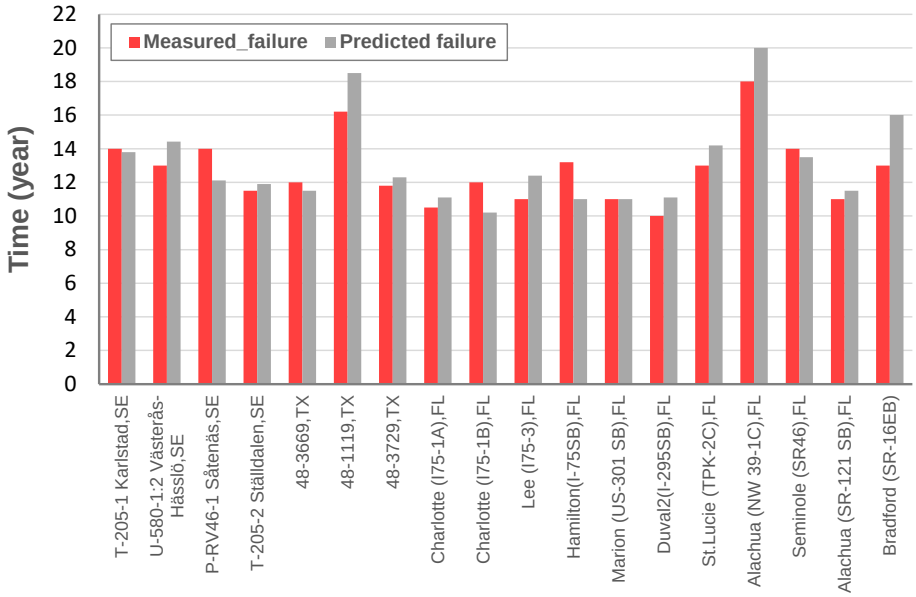

Figure 5.18 Comparison between observed and predicted pavement failure time.

5.7. Conclusions

This paper presents a novel unified mechanics-based framework for predicting the long-term TDC performance of asphalt pavements. The unified framework consists of two distinct sub-frameworks that are the crack initiation sub-framework and the crack propagation sub-framework. The required inputs for the unified crack initiation and propagation framework are either measured or predicted using established and verified models. Our robust input module and material module are capable to cover a wide range of different pavements all over the world with diverse specifications like traffic, climatic conditions, material properties, structural configuration, etc. To improve the crack initiation prediction, the HMA fracture mechanics-based framework is integrated to predict TDC initiation, which shows a significant improvement in accuracy compared with the original NCHRP 1-52 crack initiation sub-model. A more accurate predicted TDC initiation time is adopted as an essential inputs to the crack propagation sub-model based on the J-integral-based Paris' law. Eighteen pavement sections from different geographical locations with well-documented performance history and material properties were evaluated. The predicted results indicates that the proposed unified framework is able to accurately predict the crack initiation and failure time of field pavements.

The prediction results shown in this study were based on limited data available. More data is needed to help better validate the proposed framework. Future work will focus on extending the field validation sections to further evaluate the performance of the unified

TDC framework. In addition, future work will include establishing the performance prediction process described here for more comprehensive prediction of the initiation and growth of all forms of traffic-related pavement cracking distress, including TDC, BUC, reflective cracking, and thermal cracking. The thermal-induced crack growth model developed in the NCHRP 1-52 project may also be incorporated into the new unified cracking model. On the other hand, the authors will continue focusing on establishing and presenting improved material properties prediction in the material module that further improves the links between mixture composition and key performance properties.

6. PERFORMANCE IMPACTS OF TRUCK AUTOMATION AND TRUCK PLATOONING ON TEXAS PAVEMENTS AND BRIDGES

6.1. Introduction

The rise of private vehicles in cities leads to a number of problems including, but not limited to, increasing CO2 emission and energy consumption, increasing accident occurrence because of human error, exacerbating traffic congestion, reducing service life of road infrastructure. Autonomous vehicles (AVs) has received substantial attention because this technology is the potential solution to the problems mentioned above (Weisser 1998, Fagnant and Kockelman 2015, Litman 2017, Vahidi and Sciarretta 2018). According to the S-curve theory (Liu *et al.* 2019), it was predicted that the proportion of AVs circulating would reach 20% by the end of 2030s and occupy 50% by the end of 2050s.

The design and performance of pavement system (bridges and pavements) depend on climate, truck traffic, structure, and material properties (Mallick and El-Korchi 2008). Connected and autonomous trucks (CATs) affect truck traffic factor differently from HTs because of the characteristics of CATs in terms of lane choice, lateral positioning, and number of trucks and truck spacing within a platoon.

HTs (HTs) normally do not follow the exact path on a road while travelling. The term ‘wheel wander’ can be used to characterize this phenomenon and is defined as the lateral distribution of wheel loads over a pavement cross section (Gungor 2018). Wheel wander of HTs is affected by several factors including weather conditions (i.e. wind speed and precipitation), environment, time, type of vehicle, traffic conditions, and road

characteristics (i.e. road type, road configuration, road roughness, road markings) (Buiter *et al.* 1989). Blab and Litzka reported four factors that most influence lateral positioning of vehicles: lane width, vehicle width, vehicle speed and rut depth in the cross section (Blab and Litzka 1995). Field measurements showed that the wheel path of HTs is normally distributed within a traffic lane (Buiter *et al.* 1989). Standard deviation of its probability density curve is commonly used to characterize the spread of wheel loads. The standard deviation of wheel wander ranges from 8 to 24 inches depending on the lane width and vehicle size and so on, and it is taken as 10 inches in most pavement design (ARA Inc. 2004).

Compared with HTs, the wheel wander of ATs is programmed by the vehicle computer embedded into the vehicle steering system. Therefore, the ATs, theoretically, are able to follow any predefined lateral distributions that potentially have either positive or negative impact on the long-term performance of pavements. AVs can be programmed to follow a channelized wheel path with extremely small wheel wander (zero wheel wander). This type of wheel wander helps with increasing traffic safety due to more predictable traffic trajectory, increasing passenger comfort, and reducing the traffic lane width in design which reduces the total cost of pavement construction. On the other hand, the studies showed that the channelized wheel loads caused faster damage accumulation on one spot of the pavement which thereby yield a reduced service life (Forrest and Konca 2007, VdM Steyn and Fisher 2008, Litman 2017). Therefore, it is important to study the effect of ATs or CATs on the long-term performance of pavement system.

This study focused on developing a framework for evaluating autonomous truck effect on asphalt pavements and truck platooning effect on bridges in Texas highway system. This study is organized as follows. The next section introduces the framework for evaluating autonomous truck effect on asphalt pavements including input module, traffic module, material module, and pavement performance module. The data collection and results and discussion were included in the end of the first section. Section two conducted a high-level prioritization of existing Texas bridges using the National Bridge Inventory (NBI) data along with prior research. The prioritization levels for about 55000 bridges in Texas were calculated under various future truck-platoon-loading scenarios. The last section summarizes the significant findings of this study.

6.2. Framework for Evaluating Autonomous Truck Effect on TDC Performance of Asphalt Pavements in Texas

6.2.1. General Flow Chart of Framework

Chapter 5 developed a unified mechanics-based TDC predictive framework to evaluate the TDC performance of asphalt pavements. This section adopted the same framework with some modifications to study the autonomous truck effect on TDC performance of asphalt pavements. The major modifications includes incorporation of a resilient modulus prediction model that considers stress-moisture dependent behavior of unbound layers (i.e. base, subbase, and subgrade layers), and a new traffic load spectra model that distinguishes HTs from autonomous trucks. A generalized flowchart is presented in Figure 6.1 to illustrate the structure of the modified TDC framework.

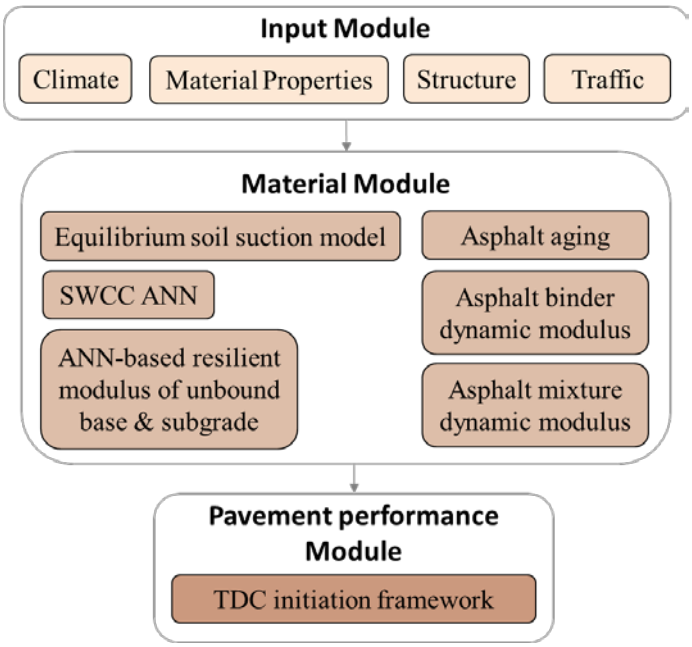

Figure 6.1 Illustration of the process and interdependencies of each module in TDC framework.

6.2.2. Input Module

The input parameters required to evaluate the autonomous truck (AT) effect on asphalt pavements are divided into five categories, namely, asphalt mixture, unbound material, climate, pavement structure, and traffic inputs. These input parameters can be obtained through direct measurements of the associated properties, obtained from an existing database, or predicted using previously developed material prediction models. They are:

- Asphalt mixture Inputs: The mixture inputs include the full gradation of aggregates, volumetric properties of the mixture, and the PG-grade of the binder. The mixture input properties are used to calculate the following properties of the asphalt concrete mixture, including the binder G* and phase angle, dynamic modulus of asphalt mixture, asphalt stiffness aging model, the mastic coating thickness, the Dissipated

Creep Strain Energy limit (DCSE_limit), the Healing potential of the asphalt mixture, and the creep strain rate of the asphalt mixture.

- Climate Inputs: The climate inputs are required to predict temporal and seasonal variations in temperature profiles in the pavement structure (Han *et al.* 2011), and to calculate Thornthwaite Moisture Index (TMI). The hourly variation in pavement temperature profile is used in the material module to predict the changes in the mixture properties, e.g., dynamic modulus and dissipated creep strain energy. TMI is used to represent the climate factor in the prediction of the equilibrium soil suction at the depth of moisture active zone. Typical climate inputs include the annual hourly air temperature and precipitation, and the mean annual air temperature (MAAT).
- Unbound material inputs: The unbound material inputs are required to predict modulus of unbound layers in asphalt pavements. The typical unbound material inputs include Atterberg limits, aggregate gradation, optimum moisture content, maximum dry density, and specific gravity.
- Pavement Structural Inputs: Pavement structural information is required to simulate pavement response due to the application of traffic load. The structural information required for the analysis includes the layer thicknesses, Poisson's ratio, and moduli of unbound layers and asphalt concrete mixture determined from the material module. This framework employs a Python-based Finite Element Method (FEM) algorithm to calculate pavement response including the stress, strain, and deformation fields in the pavement layers.

- Traffic Inputs: The traffic inputs are required to account for the influence of human-driven trucks (HTs) and/or autonomous trucks (ATs) on the long-term performance of asphalt pavements. Two levels of traffic data input were established based on data availability. WIM data is preferred when it is available (level one) because it best represents the field traffic condition. AADTT or ESAL can be used as level-two traffic input data when WIM data is not available.

6.2.3. Traffic Module

6.2.3.1. Traffic Load Spectra

Appropriate characterization of truck traffic is important in accurately predicting TDC performance of asphalt pavements. Section 2.2.2 of this dissertation introduced a traffic load spectra model developed in NCHRP 1-41 (Lytton *et al.* 2010). In NCHRP 1-41 traffic model, traffic load is categorized based on vehicle class (classes 4-13), axle types (single, tandem, tridem, and quadrem), and the number of tires (single tire and dual tire). To distinguish HTs from ATs, a user-defined autonomous truck type (class 14) was added to NCHRP 1-41 traffic model in this study. Table 6.1-6.2 present the updated vehicle class distribution and Average number of axle for each vehicle class, respectively. Figure 6.2 displays the axle configuration of the selected autonomous truck model (18-wheeler). The updated traffic load spectra model designates the number of tires for each axle for each vehicle class. As shown in Table 6.3, the single axle in vehicle class 6-7 and all axles in vehicle class 4-5 are designated as single tires, while the rest are dual tires. Therefore, the traffic load matrix can be characterized into 10 categories with 8 categories for HTs and 2 categories for ATs. The axle load distribution

for each load category is characterized by the axle load distribution curves with 38-level load bins by default (Figure 6.3). Notice that the truck type and axle load distribution for autonomous trucks used in this study are tentative as the research on ATs is still underway.

Table 6.1 Distribution of vehicle classes (USDOT 2016).

Vehicle Class	Distribution Factor (%)	Vehicle Class	Distribution Factor (%)
4	1.8	10	9.8
5	24.6	11	0.8
6	7.6	12	3.3
7	0.5	13	15.3
8	5	14	0
9	31.3	-	-

Figure 6.2 Selected axle configuration of autonomous truck (vehicle class 14).

Table 6.2 Average number of axle for each vehicle class (USDOT 2016).

Vehicle Class	Single Axle	Tandem Axle	Tridem Axle	Quadrem Axle
4	1.62	0.39	0	0
5	2	0	0	0
6	1.02	0.99	0	0
7	1	0.26	0.83	0
8	2.38	0.67	0	0
9	1.13	1.93	0	0
10	1.19	1.09	0.89	0
11	4.29	0.26	0.06	0
12	3.52	1.14	0.06	0
13	2.15	2.13	0.35	0
14	1	2	0	0

Table 6.3 Categories of traffic load (Lytton *et al.* 2010).

Vehicle Class	Single Axle	Tandem Axle	Tridem Axle	Quad Axle
4	1	3	5	7
5				
6		4	6	8
7				
8	2			
9				
10				
11				
12				
13				
14	9	10	-	

(Shaded areas are axles using single tire; unshaded areas are axles using dual tires)

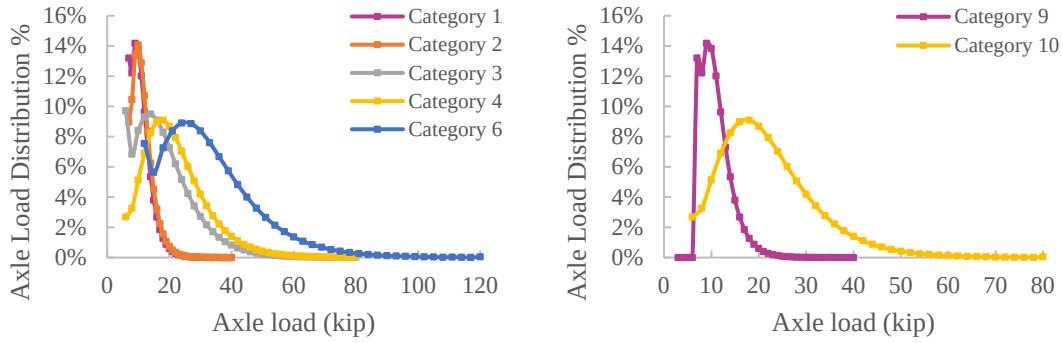

(a) (b)

Figure 6.3 Default axle load distribution for (a) HTs and (b) ATs.

6.2.3.2. Traffic Wheel Wander

The evaluation of pavement performance relies upon, among other factors, traffic loadings. The driving behavior of ATs is different from HTs in terms of both lane choice and lateral positioning (wheel wander). HTs do not normally follow the same repetitive path while traveling, while ATs are controlled by vehicle control systems and can follow a precise channelized wheel path which induces concentrated traffic loads (i.e., "zero-

wheel wander"). As a result of this characteristic, the service life of pavements will be shortened over time due to autonomous truck loads. Therefore, this study considered the wheel wander effect of HTs and ATs separately in modelling TDC performance of asphalt pavements. As an example, Figure 6.4 shows the one million tire deviations from the center of wheel path that follow normal distribution with standard deviations of 5, 10, and 15 inches, respectively.

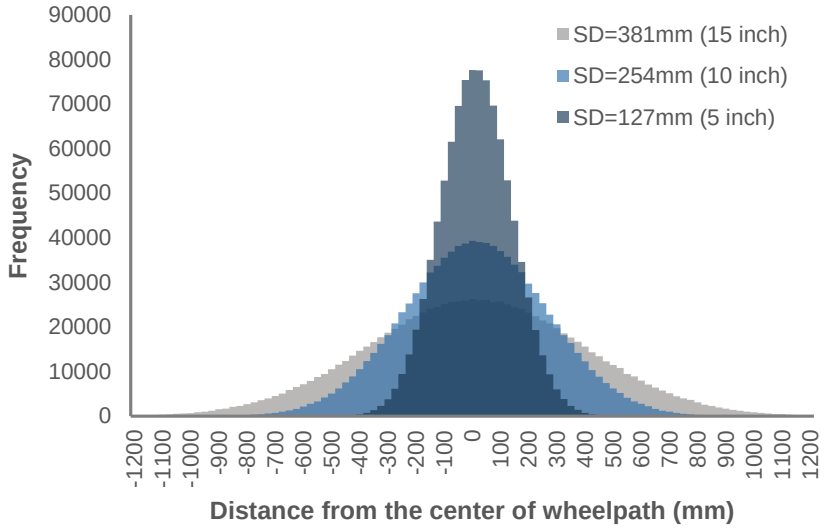

Figure 6.4 Normally distributed tire deviations with different standard deviations: 127 mm (5 inches), 254 mm (10 inches), and 381 mm (15 inches).

6.2.4. Material Module

6.2.4.1. Equilibrium Soil Suction Prediction

This study employed a modified equilibrium soil suction model (Saha et al. 2019) to predict the equilibrium soil suction at the depth of moisture active zone. The details are summarized in section 3.3.1 – 3.3.2 including the calculations of Thornthwaite Moisture Index (*TMI*), depth of moisture active zone (Z_m), Maximum available annual moisture

depth (d_{am}), diffusivity coefficient (α), mean annual moisture (d_m), and finally the equilibrium soil suction (u_e). The predicted equilibrium soil suction is converted into volumetric water content using ANN-based soil water characteristic curve (SWCC) (Saha *et al.* 2018a).

6.2.4.2. Resilient Modulus of Unbound Base and Subgrade Soil

Resilient modulus is a measure of stiffness for unbound materials (i.e. unbound aggregate base and fine-grained subgrade soil). Section 4.3 reviewed the research on modelling resilient behavior of unbound materials. To characterize the stress-dependency and moisture sensitivity in the subgrade soil, Lytton model (Lytton 1996) (Eqn. 6.1) was used in this study.

$$M_R = k_1 P_a \left(\frac{I_1 - 3\theta fh}{P_a} \right)^{k_2} \left(\frac{\tau_{oct}}{P_a} + 1 \right)^{k_3} \quad \textbf{(6.1)}$$

where I_1 is the first invariant of the stress tensor in kPa; P_a is atmospheric pressure in kPa; θ is volumetric water content; h is matric suction in kPa; f is saturation factor, $1 \le f \le \frac{1}{\theta}$; τ_{oct} is octahedral shear stress in kPa; and k_1, k_2, and k_3 are fitting coefficients where k_1 is in kPa and k_2 and k_3 are dimensionless.

f is a saturation factor which is multiplied by volumetric water content and soil suction to represent the stress exerted on the soil skeleton due to the existence of water. The expression of the saturation factor is given as

$$f = 1 + \frac{S - 85}{15}\left(\frac{1}{\theta} - 1 \right) \quad \textbf{(6.2)}$$

where S is degree of saturation in percent; and θ is volumetric water content in decimal.

Saha et al. (Saha *et al.* 2018b) developed an artificial neural network (ANN)-based model for unbound base material to predict coefficients used in Lytton model (Lytton 1996), while the applicability of this model to unbound subgrade soil is unknown. Therefore, this study collected resilient modulus test data with corresponding soil properties (e.g. Atterberg limits, aggregate gradation, optimum moisture content, maximum dry density, and specific gravity) from LTPP database to train and validate ANN models for predicting coefficients of Lytton model for subgrade soils.

A total of 305 plastic subgrade materials and 514 non-plastic subgrade materials were selected for construction of and validation of ANN models for plastic and non-plastic subgrade soil, respectively. Table 6.4 presents the input and output of the ANNs for plastic and non-plastic subgrade soil.

Similar to Saha's previous research (Saha *et al.* 2018b), we constructed the ANN with a three-layer structure including input layer, hidden layer, and output layer. The hidden layer consists of 10 neurons to characterize the relationship between input and output. 6 ANNs were finally constructed to predict Lytton model coefficients (k_1, k_2, and k_3) for both plastic and non-plastic subgrade soil. Figure 6.5 shows training and validation results of the 6 constructed ANNs for predicting Lytton model coefficients (k_1, k_2, and k_3) for both plastic and non-plastic subgrade soil. The coefficient of determination (R^2) in model validation were all larger than 0.96 which indicates high accuracy in the prediction of model coefficients (k_1, k_2, and k_3) for plastic and non-plastic subgrade soil.

Table 6.4 Input and output of ANN for plastic and non-plastic subgrade soil.

Input		Output
Plastic Soil (PI > 0)	Non-plastic Soil (PI = 0)	
%passing 3/8; *% passing #200*; *% passing #4*; *% passing #40*; *PL*; *PI*; *MDD*; *OMC*; *Compaction moisture content*; *Compaction dry density*; G_s	*OMC*; *MDD*; *% passing #3/8*; *% passing #40*; *% passing #200*; *Compaction moisture content*; *Compaction dry density*; G_s	k_1; k_2; k_3

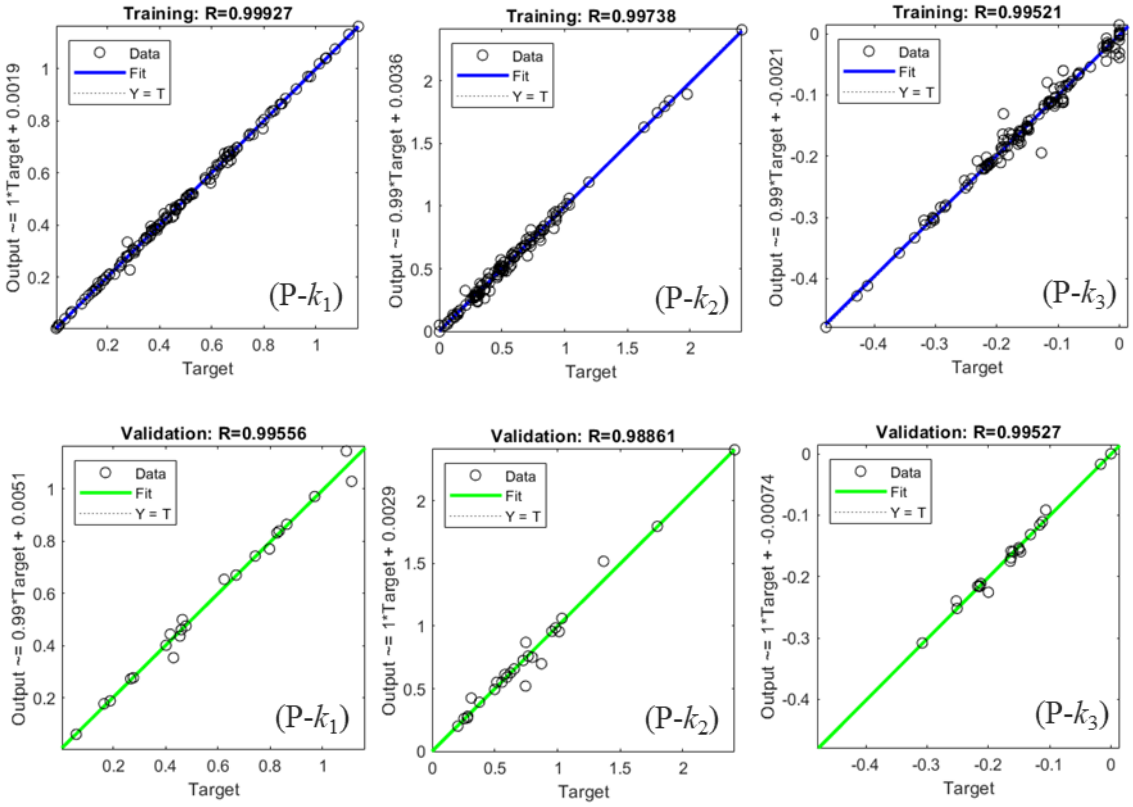

Figure 6.5 Training and validation results of k_1, k_2, and k_3 for plastic (P) and non-plastic (NP) subgrade soils.

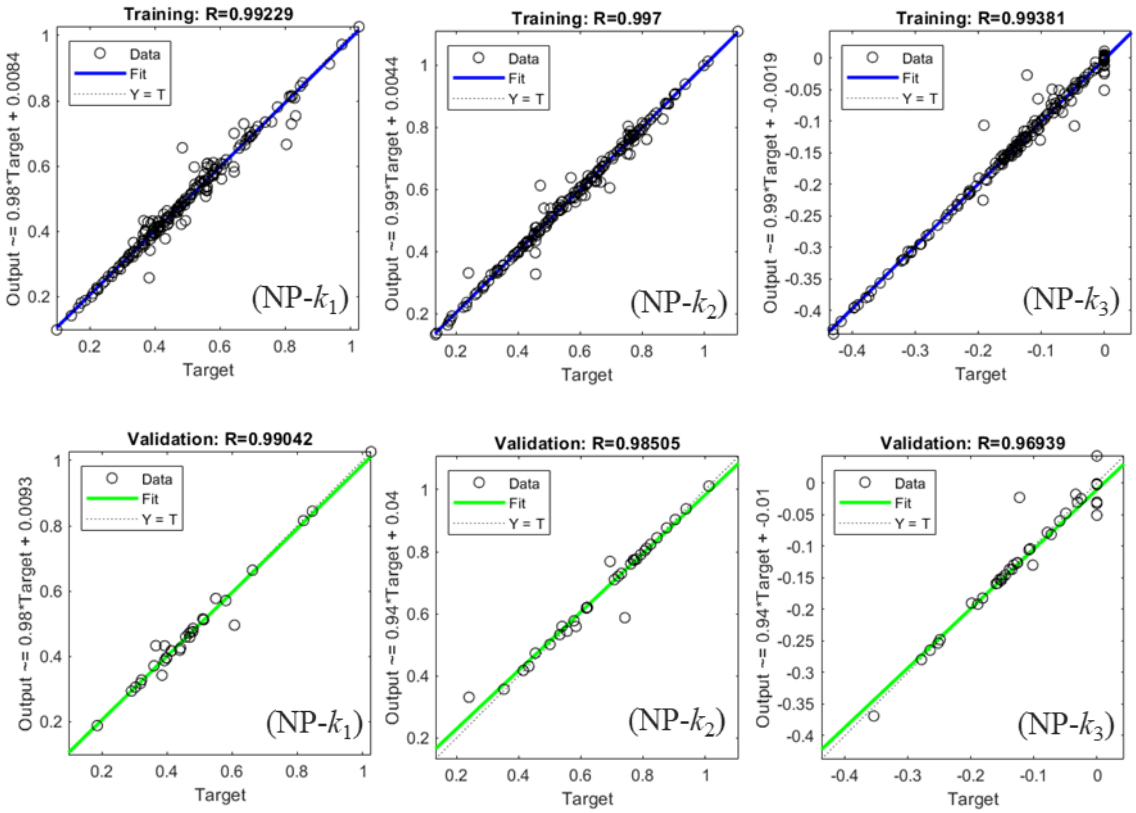

Figure 6.5 Training and validation results of k_1, k_2, and k_3 for plastic (P) and non-plastic (NP) subgrade soils (cont'd).

To further verify the constructed ANNs, ANN predicted k-values were input into Eqn. 6.1-6.2 to calculate resilient modulus (M_R) under various stress and moisture condition applied in the resilient modulus test. Figure 6.6 compares the ANN predicted M_R with lab measured M_R. R^2 were determined to be 0.9812 and 0.9878 for plastic and non-plastic subgrade soil, respectively, indicating high accuracy in the prediction of M_R for subgrade soil.

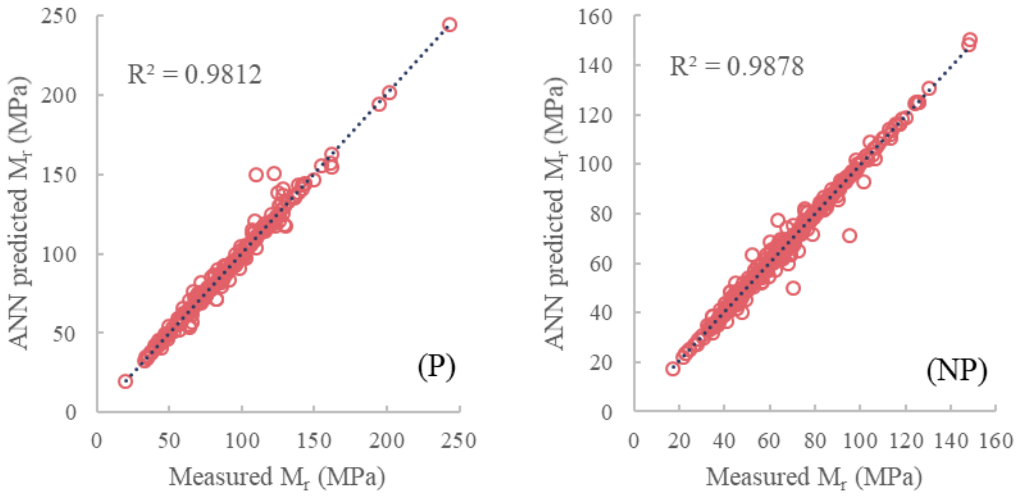

Figure 6.6 Comparison of measured and ANN predicted resilient modulus for plastic (P) and non-plastic (NP) subgrade soil.

Figure 6.7 outlined the structure of the stress-moisture-dependent resilient modulus prediction framework for unbound materials using the material modules presented above.

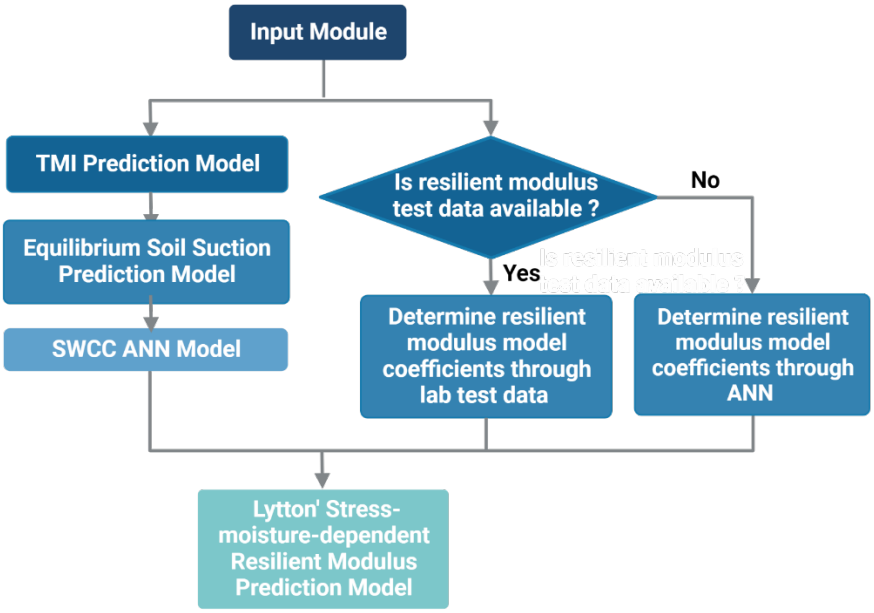

Figure 6.7 Flowchart of resilient modulus prediction framework.

6.2.4.3. Dynamic Modulus of Hot Mix Asphalt

Dynamic modulus is one of the most important parameters used in asphalt pavement design. In addition, it is also used in evaluating fatigue cracking and rutting performance of asphalt pavements. Therefore, accurately modelling dynamic modulus of asphalt mixture is crucial in the development of the TDC framework in this study.

This study adopted the framework introduced in section 5.2.3.1-5.2.3.3 of this dissertation for modelling dynamic modulus of asphalt mixture including a short-term and long-term aging model for asphalt binder, dynamic modulus model for asphalt binder, and Witczaks's 2006 dynamic modulus model for asphalt mixture. Figure 6.8 illustrates the flowchart of the dynamic modulus prediction framework for asphalt mixture.

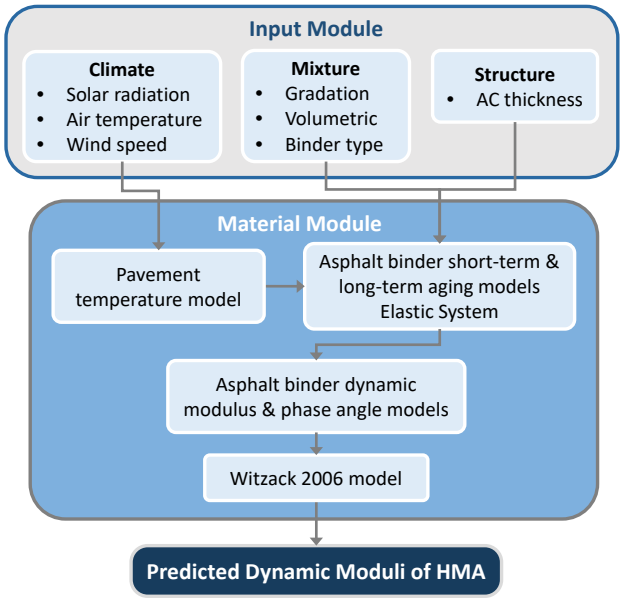

Figure 6.8 Flowchart of dynamic modulus prediction framework for asphalt mixture.

6.2.5. Pavement Performance Module

Dinegdae et al. (Dinegdae *et al.* 2015) developed a mechanics-based top-down crack initiation prediction framework for asphalt pavements based on the enhancement of HMA-FM. The fracture resistance and healing potential of asphalt mixture was characterized by incorporating a morphological parameter (Das *et al.* 2015). Huang et al. (Huang *et al.* 2021) recalibrated Dinegdae's TDC initiation model by a failure curve-based calibration methodology after considering the wheel wander effect of traffic loads. However, neither traffic load spectra nor traffic growth rate were considered in the TDC framework. In this study, the recalibrated TDC initiation model was further improved by incorporating a more realistic traffic load spectra model and stress-moisture dependent resilient modulus prediction model for unbound materials. A traffic load spectra model developed in NCHRP 1-41 (Lytton *et al.* 2010) was adopted and modified to reflect the percentage of HTs and ATs. Traffic growth rate was also considered in the modified traffic load spectra model. Figure 6.9 shows the structure of the TDC initiation framework developed in section 5.2.4 of this dissertation.

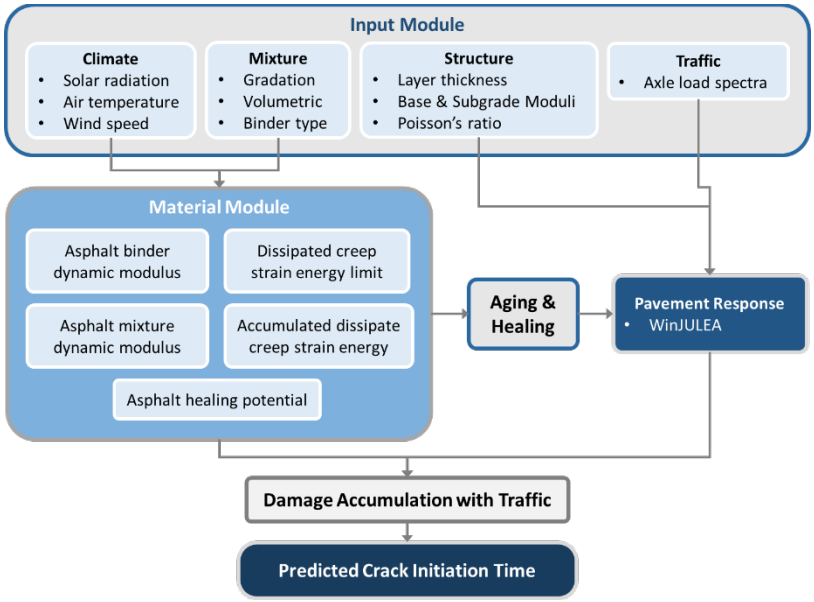

Figure 6.9 Flowchart of TDC initiation framework.

As shown in Figure 6.9, the employed TDC initiation framework considers the effects of temperature change, aging, and healing in asphalt layers on an hourly basis. Therefore, the dynamic modulus of AC is updated every hour, which means that the pavement response is dependent on not only the tire load but also the time when it is applied. As a result, the multi-layer linear elastic analysis program WinJULEA has to be called very frequently to obtain pavement response (i.e. tensile stress profile at pavement surface) to each load. The calculated pavement response is then used to calculate the remaining Accumulated Creep Strain Energy (*ACSE*) and the Dissipated Creep Strain Energy (*DCSE*) densities limit of the asphalt layer. When the remaining *ACSE* exceeds the *DCSE*_lim, a macro-crack initiates. In addition, the output of the traffic load spectra model used in this study includes single-axle-single-tire load spectra with 38-level load bins and single-axle-dual-tire load spectra with 38-level load bins. Therefore, we established the rules below to simplify the computation process.

- single-axle-dual-tire load spectra with 38-level load bins are grouped into single-axle-single-tire load spectra with 38-level load bins using equivalent axle load factor (EALF);
- pavement responses are updated every 6 hours for each load bin;
- RegularGridInterpolator function from python scipy library was used to replace WinJULEA with a simple 4D linear interpolation function.

To examine the accuracy of the generated scipy interpolation function, the pavement response (tensile stress profile at pavement surface) due to fixed dynamic modulus of AC and 5 different tire loads (3250 lbf, 7250 lbf, 11250 lbf, 15250 lbf, and 19000 lbf) were calculated by WinJULEA and the scipy interpolation function, respectively. Figure 6.10 - 6.11 compare the pavement response calculated by WinJULEA and the scipy interpolation function. The coefficient of determination (R^2) is 0.998, which indicates high accuracy of the scipy interpolation function in the prediction of pavement response.

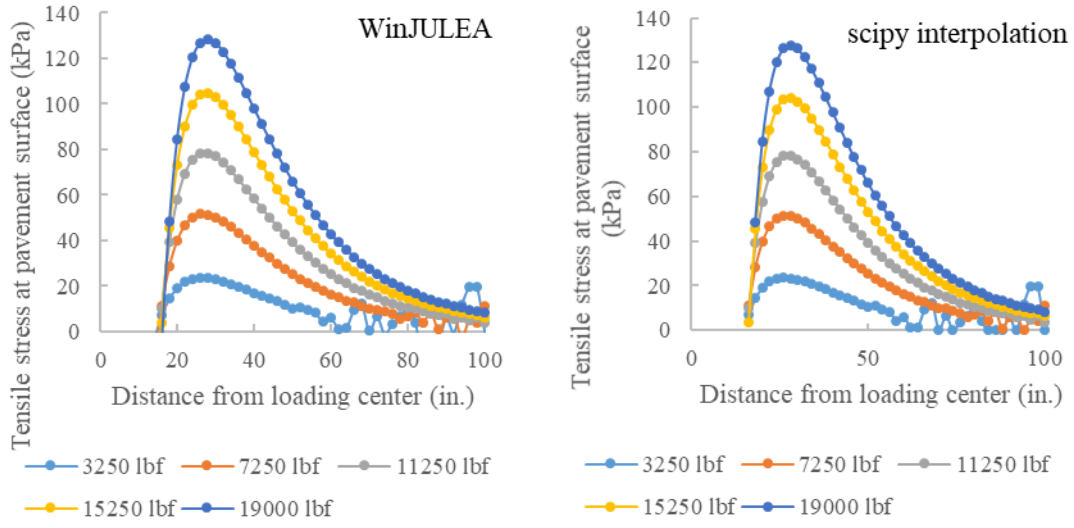

Figure 6.10 Pavement response calculated by WinJULEA and scipy interpolation, respectively.

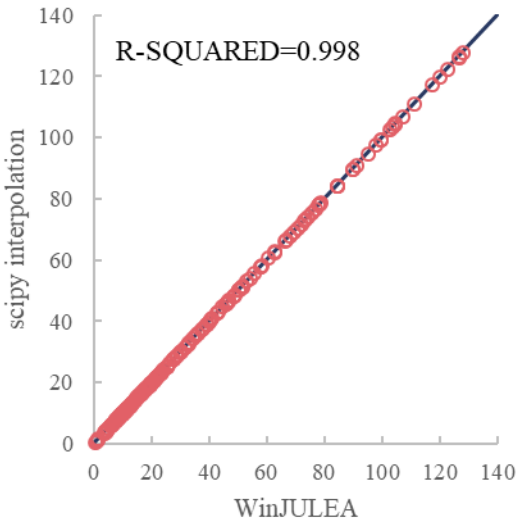

Figure 6.11 Comparison of pavement response calculated by WinJULEA and scipy interpolation function.

6.2.6. Data Collection

The FHWA Long-Term Pavement Performance (LTPP) program collects research quality data of climate, paving materials, and pavement performance from in service sections across USA and Canada (LTPP InfoPave 2020). This study selected 31 asphalt pavement sections in TX from LTPP database to study the autonomous truck effect on TDC performance of asphalt pavements in TX. The selected 31 sections cover a variety of binder types, mix design procedures, mix volumetrics, traffic, and overall pavement design. Figure 6.12 shows the geographic locations of the selected LTPP sections on Texas freight network. As shown in Figure 6.13, the selected 31 LTPP sections revealed 6 distinct types of pavement structure. Notice that some layers under AC are limestone or cement treated base/subbase. Stress dependency or water sensitivity were not considered in these layers. Instead, FWD backcalculated modulus were used in these

layers in evaluating the TDC performance of asphalt pavement under autonomous truck loads.

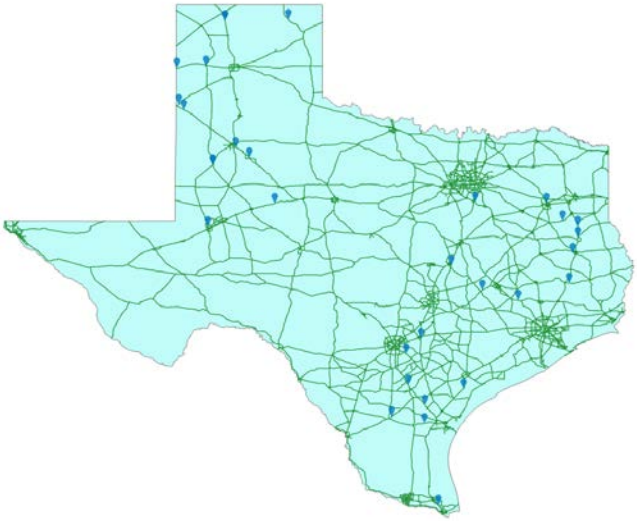

Figure 6.12 Geographic locations of selected LTPP sections on Texas freight network.

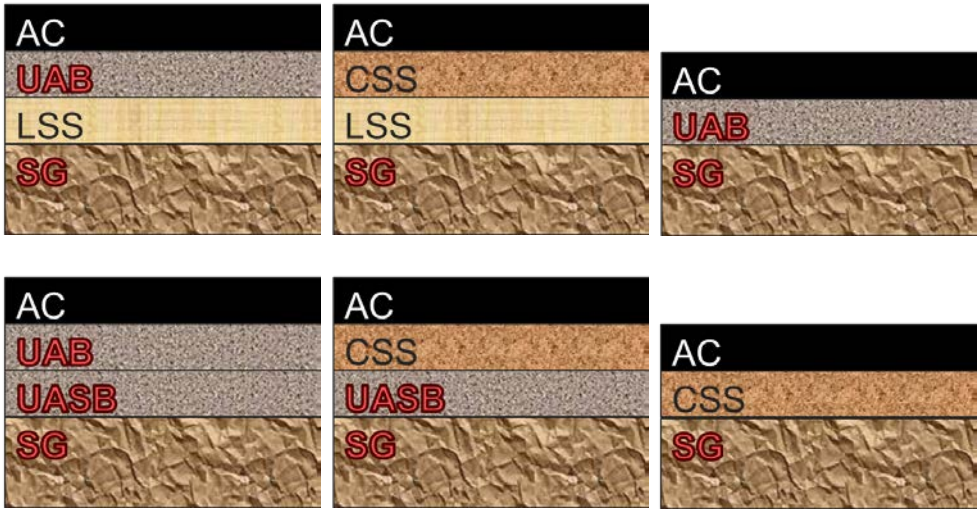

Figure 6.13 Pavement structures of selected LTPP sections.

6.2.7. Results and Discussion

6.2.7.1. Determination of Stress-moisture-dependent Resilient Modulus

This section used LTPP 48-1183 as an example to elaborate how resilient modulus of unbound materials are determined using the developed stress-moisture-dependent resilient modulus module.

Step 1: Collect input for the resilient modulus framework as shown in table 6.5.

Table 6.5 Input for the resilient moduli prediction framework.

Pavement structure	Traffic load	Climate	Geographic location	Material properties (unbound base & subbase & subgrade)
Thickness and Poisson ratio of each layer; modulus of each bounded layers	Tire radius and tire pressure	MAAT; monthly precipitation and air temperature	Latitude and longitude	Gradation; Atterberg Limit; MDD; OMC; TMC; G_s; resilient modulus test data

Step 2: Calculate TMI for at least 20 consecutive years and used the averaged TMI to represent the climate condition on site. As shown in Figure 6.14, the averaged TMI for LTPP 48-1183 is -26.75.

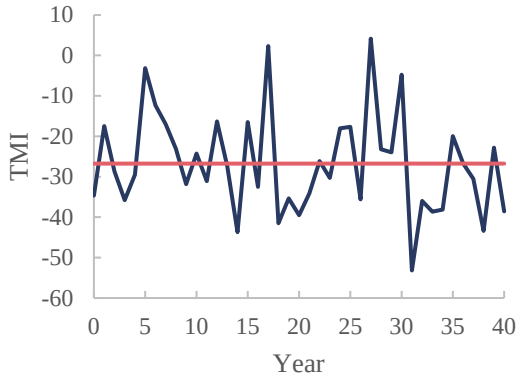

Figure 6.14 Calculated TMI vs. time for LTPP 48-1183.

Step 3: Predict equilibrium soil suction (u_e) at the depth of moisture active zone using the modified equilibrium soil suction model (Saha et al. 2019). The predicted u_e is 3.96 pF.

Step 4: Generate soil water characteristic curves for all unbound layers which are base and subgrade layers in this case using an ANN-based SWCC model (Saha *et al.* 2018a). The predicted SWCC are presented in Figure 6.15.

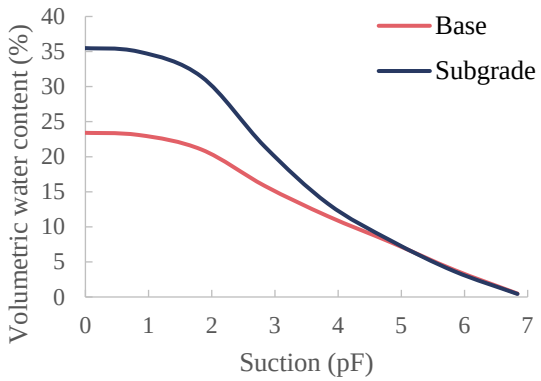

Figure 6.15 ANN-predicted SWCC for base and subgrade layers (LTPP 48-1183).

Step 5: Convert equilibrium soil suction to VWC for base and subgrade layers using the predicted SWCC obtained in step 4. The converted VWC were 11.06% and 12.57% for base and subgrade layers, respectively.

Step 6: As mentioned in Figure 6.7, there are two ways of determining resilient modulus model coefficients. One is to use the ANN model (Saha *et al.* 2018b), and other is to use the resilient modulus test data to fit the resilient modulus model. The resilient modulus test data of both unbound base and subgrade layer are available for LTPP pavement section 48-1183. Therefore, the second method was used and the fitting results for base

and subgrade layer are presented in Figure 6.16. The fitted model coefficients were k_1=0.518, k_2=0.743, and k_3=-0.234 for base and k_1=0.352, k_2=0.672, and k_3=-0.327 for subgrade.

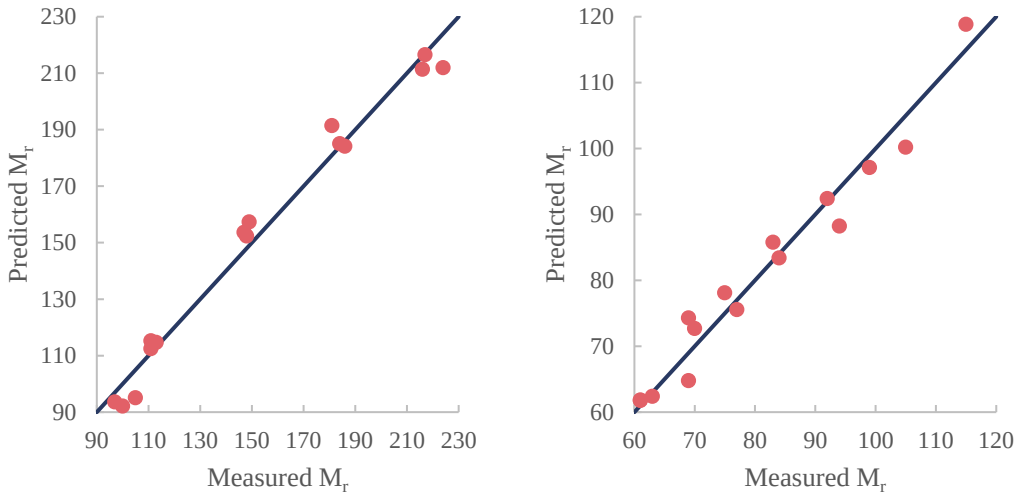

Figure 6.16 Predicted vs. measured resilient modulus for base and subgrade layers (LTPP 48-1183).

Step 7: Considering that resilient modulus of unbound base and subgrade layers are stress-dependent, and stress state of material are decided by its modulus, an iteration process is necessary to obtain converged resilient modulus for each layer. Figure 6.17 shows that both base and subgrade moduli converged after 6 times of iteration. The converged resilient moduli for base and subgrade were 184.3 MPa and 159.0 MPa, respectively.

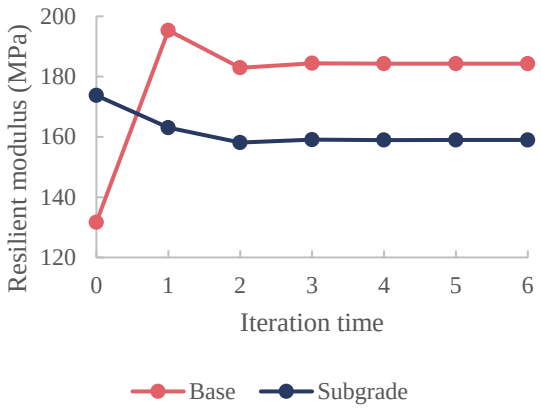

Figure 6.17 Converged resilient modulus for base and subgrade layers (LTPP 48-1183).

Table 6.6 summarized the predicted resilient moduli for the rest selected LTPP sections. The 'nan' value in the table means that the materials used in those layers are either limestone or cement treated materials, and only unbound layers were considered to be stress-dependent and moisture-sensitive in this study.

Table 6.6 Predicted resilient modulus for base, subbase, and subgrade layers.

Section	Eb (MPa)	Esb (MPa)	Esg (MPa)	Section	Eb (MPa)	Esb (MPa)	Esg (MPa)
1039	66.67	nan	75.18	1174	147.70	nan	88.87
1049	nan	nan	107.63	1178	64.35	nan	67.96
1050	193.71	nan	128.35	1181	68.63	nan	60.71
1056	152.80	nan	60.05	1183	184.30	nan	158.97
1060	12.21	nan	105.68	2133	nan	158.03	112.41
1061	184.12	nan	134.37	2172	nan	133.69	205.83
1065	54.76	nan	159.39	3669	nan	nan	80.32
1077	75.55	nan	69.14	3689	nan	nan	81.60
1087	91.32	nan	62.88	3729	53.97	nan	162.39
1111	146.01	nan	73.91	3875	180.37	nan	165.20
1116	68.81	nan	41.44	6079	39.25	nan	72.41
1119	68.81	nan	39.14	6086	22.71	nan	232.30
1122	227.84	62.89	63.25	6160	167.82	166.86	135.69
1130	64.19	nan	112.45	6179	199.87	183.09	155.48

6.2.7.2. Predicted TDC Initiation Time under HTs and ATs

ATs affect pavement design and performance differently from HTs in terms of lane choice and lateral positioning on pavements. Field measurements showed that the wheel path of HTs is normally distributed within a traffic lane (Buiter et al. 1989). Standard deviation of its probability density curve is commonly used to characterize the spread of wheel loads.

Because autonomous trucks and truck platooning technologies are still in development, there is very limited traffic data available for ATs. This section investigate the effect of autonomous trucks on TDC performance of asphalt pavements based on the following assumptions.

- Wheel path of HTs is normally distributed with standard deviation of 10 in.
- Wheel path of ATs is normally distributed with standard deviation of 0 in.
- HTs and ATs share the same annual traffic growth rate.

Figure 6.18 compares the predicted TDC initiation time due to 100% HTs (standard deviation of 10 in.) and ATs (standard deviation of 0 in.), respectively, for 31 LTPP sections. The predicted crack initiation times for all 31 LTPP sections were predicted to be 0.12 to 3.35 years earlier under AT loads than under HT loads. This is because the traffic-induced damage in pavement structure accumulates faster under concentrated AT loads and therefore results in earlier crack initiation time. The effect of ATs on the service life reduction in asphalt pavement varies from section to section due to different pavement structure, material properties, traffic, and local climate condition.

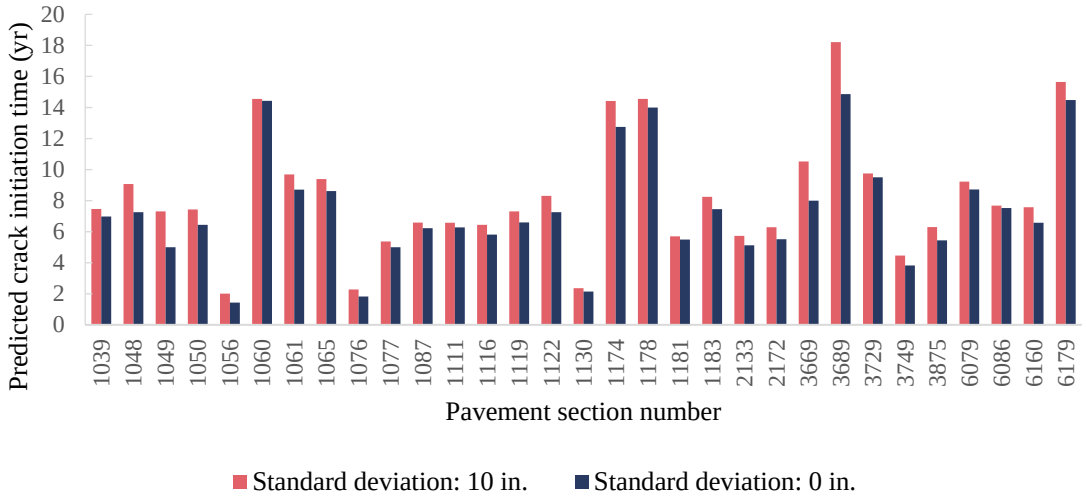

Figure 6.18 Predicted crack initiation time caused by human-driven and autonomous trucks, respectively, using simplified traffic model.

The improved TDC framework is also capable of studying the effect of AT percentage on the TDC performance of asphalt pavements. Figure 6.19 presents the predicted crack initiation time for 10 LTPP sections under a mixture of HT and AT loads with AT percentage of 0%, 25%, 50%, 75%, and 100%, respectively. According to the results, the remaining service life is reduced as AT percentage increases. There are 6 (out of 10) studied sections that were observed to have significant reduction in the remaining service life when the AT percentage increases from 0% to 25%. 3 (out of 10) studied sections show consistent drop in the remaining service life with the growth of AT percentage. Only 1 section is not sensitive to the change of AT percentage in the crack initiation time prediction. Further studies are warranted to find out how AT affect service life of asphalt pavements.

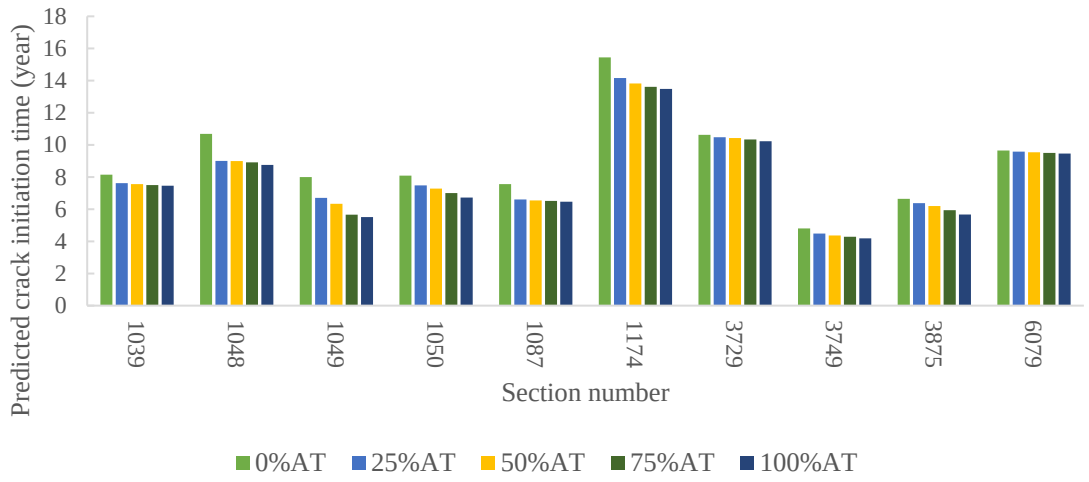

Figure 6.19 Predicted crack initiation time caused by a mixture of HTs and ATs using complete traffic model.

6.3. Truck Platooning Effect on Texas Highway Bridges

The objective for this portion of the study was to develop a framework to conduct a high-level prioritization of about 55000 existing Texas bridges, considering truck platoon loading. The National Bridge Inventory (NBI) database was leveraged, along with prior research, to evaluate each structure. The prioritization provides a relative comparison of the bridge performance under vertical loading of 6 different platooned truck configurations.

6.3.1. Methodology

The approach for this investigation was to take advantage of the existing bridge load ratings (Item 64 – Operating Rating) reported in the NBI dataset. This load rating is the absolute maximum permissible load level to which the structure may be subjected for vertical loading of conventional truck traffic. To distinguish future truck platoon loading from current truck loads, modifications were made to the load ratings. This is described

in the following section. In addition, the NBI appraisal ratings (item 67) were utilized to consider the current condition of each bridge.

6.3.2. Prioritization Metric for Bridges Subjected to Truck Platoon Loading

The prioritization metric for truck platoon loading (PM_{pl}) is defined in Equation 6.3. This expression is the product of an adjusted load rating (LR_{adj}) and a condition factor (CF) according to Table 6.7.

$$PM_{pl} = LR_{adj} CF \quad \textbf{(6.3)}$$

The adjusted load rating (LR_{adj}) was set up to be a function of the design methodology for the bridge. This information is not reported within the NBI dataset. However, the year the structure was built (item 27) is a reliable source for this information. Prior to 2005, bridges were designed using Allowable Stress Design (ASD) or Load Factor Design (LFD). After 2005, bridges were designed using the Load and Resistance Factor Design (LRFD) method. Prior research has shown that the live load model used for LRFD adequately envelops truck platoon demands (Yarnold and Weidner 2019, Tohme and Yarnold 2020). Conversely, bridges designed using the live load model within ASD and LFD can be unconservative for truck platoon loading for certain span lengths.

For bridges built prior to 2005 (ASD and LDF bridges), a modification factor approach was developed based on the work of Yarnold and Weidner (Yarnold and Weidner 2019). Essentially, the maximum flexural demand for two, three, and four-truck platoon configurations (for 20- and 40-foot platoon spacing) were compared with the design truck demands. This comparison included bridge span lengths from 50 to 300 feet, which covers the majority of the Texas bridge inventory. The modification factor was the ratio

of the truck platoon's maximum moment to the design truck's maximum moment. A best-fit cubic function was developed for each case. Figure 6.20 illustrates the dataset and best-fit function for a two-truck platoon at 20-foot spacing. Similar plots and functions were developed for the other five cases. Note that the bounds for the modification factor were set as 0.60 and 1.00.

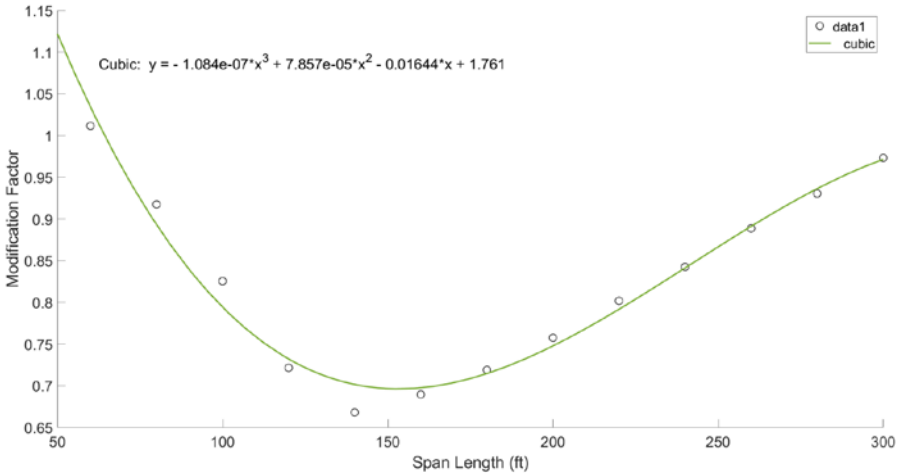

Figure 6.20 Load rating modification factor for two-truck platoons with 20-foot spacing.

The Condition Factors (*CF*) were applied according to Thulaseedharan and Yarnold's work (Thulaseedharan and Yarnold 2020). As shown in Table 6.7, Thulaseedharan and Yarnold identified *CF*s using Appraisal Ratings from NBI. Appraisal Ratings are a metric for bridge conditions based on visual inspection. The scale ranges from 0 to 9 where 9 is excellent condition. Therefore, Appraisal Ratings greater than 7 is considered a very good condition, and no need for concern.

Table 6.7 Condition Factors for each bridge Appraisal Rating.

Appraisal Rating	>7	7	6	5	<5
Factor	1	0.85	0.75	0.6	0.5

6.3.3. Prioritization Results

This section evaluates all Texas bridges using PM_{pl} in Equation 6.3. The determined PM_{pl} values were separated into five Prioritization Levels (PL). Level 1 indicates relatively low priority, and Level 5 indicates relatively high priority. A high priority indicates that the structure should be evaluated further for future truck platoon loading. Figure 6.21 illustrates the results for the Texas bridge inventory. Several observations were made from these results. First, more than half of the bridges are categorized as Level 1 or Level 2, indicating that a large percentage of the Texas bridge inventory is adequate for truck platoon loading. However, roughly a quarter of the bridges are at Level 4, indicating a good portion might need further evaluation to determine if additional strengthening should be performed. There is a relatively low portion of Level 5 (high priority) bridges. These are the structures that should be investigated first for the adequacy of future truck platoon loading.

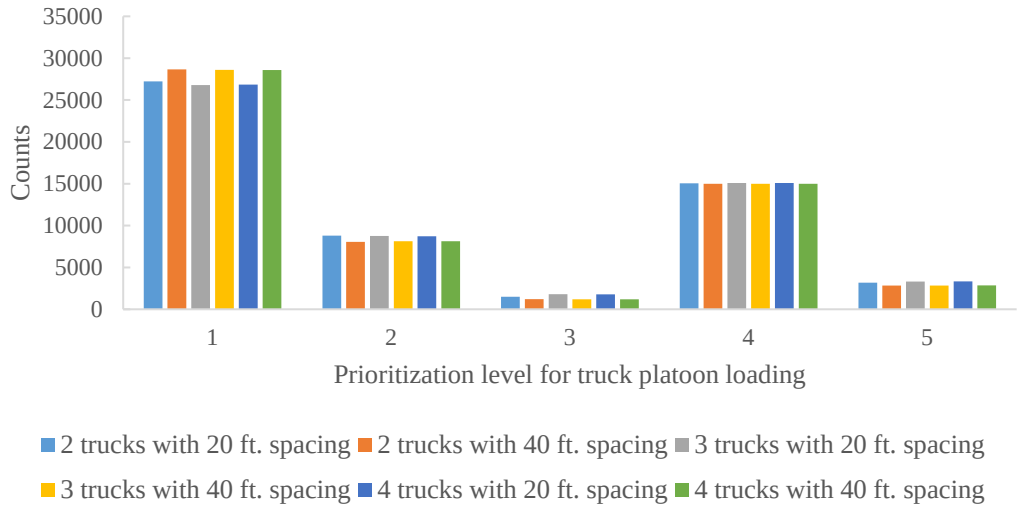

Figure 6.21 Bridge Prioritization Levels for Future Truck Platoon Loading.

Figure 6.22 shows the geographical locations of TX bridges categorized as level 1- 5, respectively, using the platooned truck configuration of two trucks with 20 ft. spacing. Similar plots were developed for the other five cases.

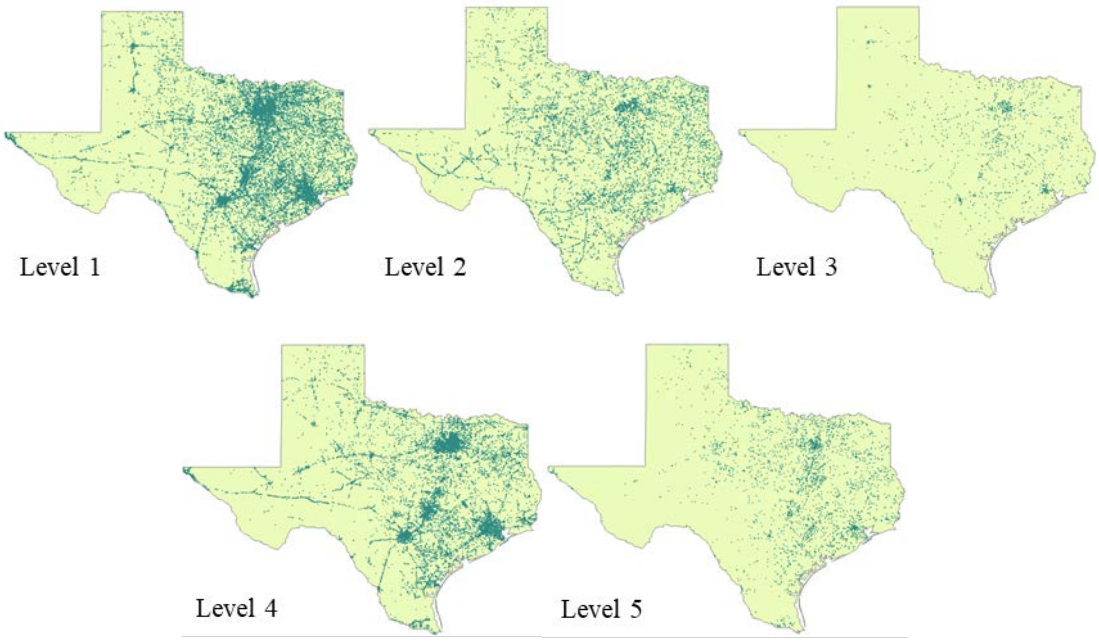

Figure 6.22 Geographical locations of bridges categorized as Level 1 - 5 due to platooned truck configuration of two trucks with 20 ft. spacing.

6.4. Conclusion

This study developed and implemented a framework for evaluating performance impact of autonomous truck and truck platooning on Texas highway system (pavements and bridges).

In the pavement module, a mechanics-based TDC initiation sub-framework was improved to study the effects of autonomous truck loads and autonomous truck percentage on the TDC performance of asphalt pavements. The major improvement includes the incorporation of a more realistic traffic load spectra model that distinguishes HTs from ATs, and a stress-moisture-dependent resilient modulus prediction model for unbound layers. The results show that the predicted crack initiation times (CIs) by autonomous truck loads are 0.12 to 3.35 years earlier than CIs by human-driven truck loads. This is because the traffic-induced damage in pavement structure accumulates faster under concentrated autonomous truck loads and therefore results in earlier crack initiation time. Different pavement sections display different sensitivity of service life reduction due to various pavement structure, material properties, traffic, and local climate condition.

In the bridge module, we developed an approach to conduct a prioritization study in about 55000 existing Texas bridges due to future platooning loads. The developed approach leveraged the National Bridge Inventory (NBI) database along with prior research to evaluate each bridge structure in Texas. Prioritization levels (from 5 to 1) were established for Texas bridge inventory under vertical loading of 6 different

platooned truck configurations. The results indicate that more than half of the bridges are categorized as Level 1 or Level 2, indicating that a large percentage of the Texas bridge inventory is adequate for future truck platoon loading. There is a relatively low portion of Level 5 (high priority) bridges that should be investigated first for the adequacy of future truck platoon loading.

The pavement and bridge performance analysis due to autonomous truck and truck platooning loads was an initial attempt in this study. Currently, the traffic data for autonomous truck and truck platooning are very limited; therefore, further investigations are warranted to verify the major conclusions drawn from this study.

7. SUMMARY, CONCLUSIONS, AND RECOMMENDATIONS

7.1. Summary

Autonomous truck (AT) as a new category in the vehicle classification has been making progressive steps towards commercial implementation. The expectation of ATs has shown exceptionally welcoming from the market perspective. ATs are different from Human-driven trucks (HTs) in traffic characteristics in terms of lane choice and lateral positioning. Current infrastructure is designed to serve traditional traffic configurations. Therefore, it is crucial to study the potential impact of ATs on the long-term performance of existing highway system (pavements and bridges) and the design of new pavements and bridges accommodating the epoch of AT.

The objective of this dissertation was to develop a mechanics-based framework to study the potential AT impact on the long-term performance of Texas highway system (pavements and bridges). The developed framework consists of input module, traffic characterization module, material property prediction module, pavement performance prediction module, and bridge analysis module. The major conclusion of each developed module was summarized in the next section followed by the limitations and recommendations of this study.

7.2. Conclusions

7.2.1. Traffic Characterization Module

Appropriate characterization of truck traffic is important in accurately predicting pavement performance. A new generalized framework was proposed in this dissertation to traffic load spectra both HTs and ATs. The developed framework considers axle load

distribution for each axle and vehicle type, different wheel wander parameters for HTs and ATs, respectively, and AT percentage. The impact indicator was introduced to quantify the AT impact on the performance of asphalt pavements in terms of top-down fatigue cracking (TDC), bottom-up fatigue cracking (BUC), and rutting.

7.2.2. Material Property Module

7.2.2.1. Moisture Prediction Model for Subgrade Soil

Subgrade soil under pavement structure is usually unsaturated, and moisture content in subgrade soil directly affect material properties (i.e. resilient modulus) and thereby pavement performance. Therefore, this dissertation proposed a mechanistic-empirical model for predicting moisture variation in subgrade soil by coupling a modified ME-based equilibrium soil suction model and Mitchell's diffusion equation. The major contributions of this part of the study are as follows.

- A new TMI model was introduced and validated by comparing with TMI-2006 using the climate data collected from 5852 weather stations across the United States.
- A previously developed equilibrium soil suction model was improved by incorporating with a new TMI model. The modified equilibrium soil suction model was validated using the moisture data from 3 MnROAD pavement sections and 1 LTPP section.
- We finally proposed a ME-based soil moisture prediction model by coupling the modified equilibrium soil suction model to Mitchell's diffusion equation. The proposed moisture prediction model was validated using the moisture data collected by 9 sensors at different depths in the subgrade soil.

7.2.2.2. Stress-moisture dependent resilient modulus model of subgrade soil

Fine-grained subgrade soil, used as the foundation of asphalt pavements, directly contributes to the overall stiffness and performance of pavement system. This portion of the study proposed a FWD-based backcalculation program to backcalculate stress-moisture-dependent resilient modulus of subgrade soil using COMSOL Multiphysics. Lytton model was employed to characterize the stress dependency and moisture sensitivity of subgrade resilient modulus. The new moisture prediction model was incorporated into the program to predict moisture and suction profile on the date when FWD testing was conducted. We used Bound Optimization by Quadratic Approximation (BOBYQA) as the optimization method to backcalculate the parameters used in Lytton model. The backcalculation program was verified using the FWD data collected from LTPP database. The following are the major conclusions made in this portion of the study.

- The moisture condition is predominant in fine-grained subgrade soil in determining the resilient modulus, while the stress state is predominant in the unbound aggregate base course.
- We found that Lytton model coefficients determined using RLT lab data could not reflect field condition because the coring in the field and/or the re-compaction of the soil specimens in lab could possibly change its inherent structure. Therefore, it is recommended to use field data (i.e. FWD) instead of RLT data to back-calculate material properties of subgrade soil (i.e. k_1).

7.2.3. Pavement Performance Prediction Module

Top-down fatigue cracking (TDC) is a common distress type in flexible pavements throughout the world. This portion of the study proposed a unified mechanics-based framework for evaluating long-term TDC performance of asphalt pavements. The unified framework was developed based on NCHRP 1-52 model and improved the robustness of NCHRP 1-52 model by replacing their empirical crack initiation model with a HMA-FM-based crack initiation model and incorporating with a novel aging model for asphalt mixture. The proposed framework was validated by 18 pavement sections from different geographical locations with well-documented performance history and material properties. The predicted results indicates that the proposed unified framework is able to accurately predict the crack initiation and failure time of field pavements.

7.2.4. Bridge Analysis Module

This portion of the study developed a framework to study the truck platooning effect on Texas bridges using National Bridge Inventory (NBI) database. A high-level prioritization for about 55000 existing Texas bridges were conducted to evaluate the bridge performance under vertical loading of 6 different platooned truck configurations. The calculated prioritization metrics were categorized into 5 levels with level 1 representing the lowest priority and level 5 representing the highest priority. A high priority bridge indicates that the structure should be evaluated urgently for future truck platoon loading. It was found that more than half of the bridges are categorized as Level 1 or Level 2, indicating that a large percentage of the Texas bridge inventory is adequate for truck platoon loading. However, roughly a quarter of the bridges are at Level 4,

indicating a good portion might need further evaluation to determine if additional strengthening should be performed. There is a relatively low portion of Level 5 (high priority) bridges. These are the structures that should be investigated first for the adequacy of future truck platoon loading.

7.2.5. Evaluation of Autonomous Truck effect on TDC Performance of Asphalt Pavements

This portion of the study further improved the unified mechanics-based TDC predictive framework by incorporating with the traffic load spectra model, wheel wander model, and stress-moisture-dependent resilient modulus model developed in this dissertation. A user-defined autonomous truck category was added to the NCHRP 1-41 traffic load spectra model to distinguish HTs from ATs. A new ANN-based resilient modulus model for subgrade soil was trained and validated using the data collected from LTPP database. RegularGridInterpolator function from python scipy library was used to more efficiently predict pavement response to traffic loads as a replacement of WinJULEA. 31 asphalt pavement sections in TX were selected from LTPP database to study the autonomous truck impact on the TDC initiation performance of asphalt pavements using the updated TDC framework. The results showed that the predicted crack initiation times (CIs) by autonomous truck loads are 0.12 to 3.35 years earlier than CIs by human-driven truck loads. This is because the traffic-induced damage in pavement structure accumulates faster under concentrated autonomous truck loads and therefore results in earlier crack initiation time. Different pavement sections display different sensitivity of service life

reduction due to various pavement structure, material properties, traffic, and local climate condition.

7.3. Limitations and Future Work

The framework (i.e. traffic characterization, paving material property, pavement performance, and bridge prioritization) developed in this study was based on limited data available. More data is needed to help further validate the developed framework.

One advantage of the developed framework is that the robust input and material modules are able to predict dynamic modulus of AC and resilient modulus of unbound according to the basic physical material properties and local climate condition; pavement performance can thereby be evaluated using the performance module given traffic information. Another advantage is that we can easily upgrade the developed framework by accommodating more pavement performance models and/or updating material module without changing the existing structure.

Therefore, future study will focus on (1) extending the field validation sections to further evaluate the performance of the proposed framework; (2) incorporating more performance models into the framework such as bottom-up fatigue cracking, rutting, and thermal-induced crack growth in asphalt pavements; (3) establishing and improving material property models that improves the links between material properties and pavement performance.

REFERENCE

AASHTO, 1993. *Guide for Design of Pavement Structures*. Washington D.C.

Ackerman, E., 2021. This Year, Autonomous Trucks Will Take to the Road With No One on Board [online]. *IEEE Spectrum*. Available from: https://spectrum.ieee.org/this-year-autonomous-trucks-will-take-to-the-road-with-no-one-on-board [Accessed 11 Aug 2022].

Ahmed, M.U., Hasan, M.M., and Tarefder, R.A., 2016. Investigating stress dependency of unbound layers using falling-weight deflectometer and resilient modulus tests. *Geotechnical Testing Journal*, 39 (6), 954–964.

Al-Qadi, I.L., Wang, H., and Tutumluer, E., 2010. Dynamic Analysis of Thin Asphalt Pavements by Using Cross-Anisotropic Stress-Dependent Properties for Granular Layer. *Transportation Research Record*, 2154 (1), 156–163.

ARA, I., 2004. Guide for Mechanistic–Empirical Design of New and Rehabilitated Pavement Structures. *Final Rep., NCHRP Project 1-37A*.

ARA Inc., 2004. *Guide for Mechanistic-Empirical Design of New and Rehabilitated Pavement Structures. NCHRP Project 1-37A Final Report*. Washington DC.: Transportation Research Board.

Archilla, A.R., 2015. Top-down fatigue cracking in high-temperature environments. *Transportation Research Record*, 2507 (1), 128–137.

Bae, A. and Stoffels, S.M., 2019. Evaluation of Pavement Subgrade Long-term Equilibrium Moisture with Suction Potential. *Ksce Journal of Civil Engineering*, 23 (1), 147–159.

Bai, J.H., Deng, W., Cui, B.S., and Ouyang, H., 2007. Water diffusion coefficients of horizontal soil columns from natural saline-alkaline wetlands in a semiarid area. *Eurasian Soil Science*, 40 (6), 660–664.

Banker, S., 2022. The 'Race' To Win The Autonomous Truck Market [online]. *Forbes*. Available from: https://www.forbes.com/sites/stevebanker/2022/04/19/the-race-to-win-the-autonomous-truck-market/ [Accessed 11 Aug 2022].

Bari, J., 2005. Development of a new revised version of the Witczak E* predictive models for hot mix asphalt mixtures. Ph.D. Arizona State University, United States -- Arizona.

Birgisson, B., Curtis, M., Matthew, Y., Jeffery, W., Brianne, G., Maxwell, S., Sunkari, S., Shengxin, C., and Dahye, L., 2020. Evaluate Potential Impacts, Benefits, Impediments, and Solutions of Automated Trucks and Truck Platooning on Texas Highway Infrastructure: Technical Report.

Birgisson, B., Soranakom, C., Napier, J.A.L., and Roque, R., 2003. Simulation of Fracture Initiation in Hot-Mix Asphalt Mixtures. *Transportation Research Record*, 1849 (1), 183–190.

Blab, R. and Litzka, J., 1995. Measurements of the lateral distribution of heavy vehicles and its effects on the design of road pavements. *In*: *Proceedings of the international symposium on heavy vehicle weights and dimensions, road transport technology, University of Michigan*. 389–395.

Brown, S.F., 1996. Soil mechanics in pavement engineering. *Géotechnique*, 46 (3), 383–426.

Brown, S.F. and Selig, E.T., 1991. The design of pavement and rail track foundations. *The design of pavement and rail track foundations*, 249–305.

Brunsell, N.A. and Gillies, R.R., 2003. Scale issues in land–atmosphere interactions: implications for remote sensing of the surface energy balance. *Agricultural and Forest Meteorology*, 117 (3–4), 203–221.

Buiter, R., Cortenraad, W.M.H., Van Eck, A.C., and Van Rij, H., 1989. Effects of transverse distribution of heavy vehicles on thickness design of full-depth asphalt pavements. *Transportation Research Record*, (1227).

Bulut, R., Muraleetharan, K.K., Zaman, M., Yue, E., Chen, L., Soltani, H., and Hossain, Z., 2014. Evaluation of the enhanced integrated climatic model for specification of subgrade soils in Oklahoma : final report.

Canestrari, F. and Ingrassia, L.P., 2020. A review of top-down cracking in asphalt pavements: Causes, models, experimental tools and future challenges. *Journal of Traffic and Transportation Engineering (English Edition)*, 7 (5), 541–572.

Ceylan, H., Guclu, A., Tutumluer, E., and Thompson, M.R., 2005. Backcalculation of full-depth asphalt pavement layer moduli considering nonlinear stress-dependent subgrade behavior. *International Journal of Pavement Engineering*, 6 (3), 171–182.

Chen, C., 2020. Validation of Laboratory Cracking Tests for Field Top-Down Cracking Performance. Ph.D. Auburn University, United States -- Alabama.

Chottani, A., Hastings, G., Murnane, J., and Neuhaus, F., 2018. Distraction or disruption? Autonomous trucks gain ground in US logistics. *McKinsey & Company*, 20.

Das, P.K., Birgisson, B., Jelagin, D., and Kringos, N., 2015. Investigation of the asphalt mixture morphology influence on its ageing susceptibility. *Materials and Structures*, 48 (4), 987–1000.

De Beer, M., Fisher, C., and Jooste, F.J., 1997. Determination of pneumatic tyre/pavement interface contact stresses under moving loads and some effects on pavements with thin asphalt surfacing layers. *In*: *Proceedings of the 8th international conference on asphalt pavements*. International Society for Asphalt Pavements Lino Lakes, Minn., 10–14.

Dennis, E., Buller, W., Xique, I., Fard, Z., Hart, B., and Brannon, G., 2019. Comparative Analysis of Sensor Types for Driver Assistance and Automated Driving Systems. *Transportation Research Board 2019 Annual Meeting*.

Dinegdae, Y.H., Onifade, I., Jelagin, D., and Birgisson, B., 2015. Mechanics-based top-down fatigue cracking initiation prediction framework for asphalt pavements. *Road Materials and Pavement Design*, 16 (4), 907–927.

Drumm, E.C., Reeves, J.S., Madgett, M.R., and Trolinger, W.D., 1997. Subgrade Resilient Modulus Correction for Saturation Effects. *Journal of Geotechnical and Geoenvironmental Engineering*, 123 (7), 663–670.

Epps, J.A., 2002. *Recommended Performance-related Specification for Hot-mix Asphalt Construction: Results of the WesTrack Project*. Transportation Research Board.

Erlingsson, S. and Ahmed, A., 2013. Fast layered elastic response program for the analysis of flexible pavement structures. *Road Materials and Pavement Design*, 14 (1), 196–210.

Fagnant, D.J. and Kockelman, K., 2015. Preparing a nation for autonomous vehicles: opportunities, barriers and policy recommendations. *Transportation Research Part A: Policy and Practice*, 77, 167–181.

Fattah, M.Y. and Salman, F.A., 2006. The active zone for heave of expansive soils. Presented at the Proceedings of the 4th Jordanian Civil Engineering Conference, 30.

Fitzpatrick, D., Cordahi, G., O'Rourke, L., Ross, C., Kumar, A., and Bevly, D., 2017. Challenges to CV and AV Applications in Truck Freight Operations. *NCHRP Web-Only Document*, (231).

Forrest, A. and Konca, M., 2007. Autonomous cars and society. *Worcester Polytechnic Institute*, 15, 23.

FPA, 2017. Design procedure for drilled concrete piers in expansive soil. Document No. FPA-SC-16-0, Houston, Texas.

Fredlund, D.G., Bergan, A.T., and Wong, P.K., 1977. Relation between resilient modulus and stress conditions for cohesive subgrade soils. *Transportation Research Record*, (642), 73–81.

Fredlund, D.G. and Rahardjo, H., 1993. *Soil Mechanics for Unsaturated Soils*. John Wiley & Sons.

Gay, D.A., 1994. Development of a predictive model for pavement roughness on expansive clay. Texas A&M University.

George, K.P., 2004. *Prediction of resilient modulus from soil index properties.* University of Mississippi, No. FHWA/MS-DOT-RD-04-172.

Georgouli, K., Plati, C., and Loizos, A., 2021. Autonomous vehicles wheel wander: Structural impact on flexible pavements. *Journal of Traffic and Transportation Engineering (English Edition)*, 8 (3), 388–398.

Göransson, N.-G., 2020. Uppföljning av vägars tekniska tillstånd: lägesrapport för observationssträckor ingående i det svenska LTPP-projektet till och med december 2019. *VTI NOTAT*, (21–2019).

Greer, L., Fraser, J.L., Hicks, D., Mercer, M., and Thompson, K., 2018. *Intelligent transportation systems benefits, costs, and lessons learned: 2018 update report*. United States. Dept. of Transportation. ITS Joint Program Office.

Gu, F., Luo, X., Zhang, Y., Lytton, R., and Sahin, H., 2016. Modeling of unsaturated granular materials in flexible pavements. *E3S Web of Conferences*, 9, 20002.

Gungor, O., 2018. A Literature Review on Wheel Wander. *Illinois Asphalt Pavement Association*.

Han, R., Jin, X., and Glover, C.J., 2011. Modeling Pavement Temperature for Use in Binder Oxidation Models and Pavement Performance Prediction. *Journal of Materials in Civil Engineering*, 23 (4), 351–359.

Hoffman, M.S. and Thompson, M.R., 1982. Backcalculating nonlinear resilient moduli from deflection data. *In*: *Transportation Research Record*. Presented at the 61st Annual Meeting of the Transportation Research Board, 42–51.

Huang, K., Onifade, I., and Birgisson, B., 2021. Calibration of mechanics-based pavement predictive framework for top-down cracking performance of flexible pavement considering wheel wander effect. *Construction and Building Materials*, 306, 124792.

Javid, A.H., Al-Dakheeli, H., and Bulut, R., 2022. Development of a Linear Equilibrium Suction Model Based on TMI and Climatic Regions for Oklahoma. *In*: E. Tutumluer, S. Nazarian, I. Al-Qadi, and I.I.A. Qamhia, eds. *Advances in Transportation Geotechnics IV*. Cham: Springer International Publishing, 391–401.

Javid, A.H. and Bulut, R., 2019. Evaluating equilibrium matric suctions under pavement system based on Thornthwaite moisture index (TMI). *Airfield and Highway Pavements 2019: Testing and Characterization of Pavement Materials*, 511–521.

Juárez-Badillo, E., 1975. Constitutive relationships for soils. *In*: *Proceedings Symposium on Recent Developments in the Analysis of Soils Behaviour and Their Application to Geotechnical Structures*. 231–257.

Karasahin, M., Dawson, A.R., and Holden, J.T., 1993. Applicability of resilient constitutive models of granular material for unbound base layers. *Transportation research record*, (1406), 98–107.

Khoury, N.N. and Zaman, M.M., 2004. Correlation Between Resilient Modulus, Moisture Variation, and Soil Suction for Subgrade Soils. *Transportation Research Record*, 1874 (1), 99–107.

Kim, M., Tutumluer, E., and Kwon, J., 2009. Nonlinear Pavement Foundation Modeling for Three-Dimensional Finite-Element Analysis of Flexible Pavements. *International Journal of Geomechanics*, 9 (5), 195–208.

Kutay, M.E. and Lanotte, M., 2018. Viscoelastic continuum damage (VECD) models for cracking problems in asphalt mixtures. *International journal of pavement engineering*, 19 (3), 231–242.

Laing, K., 2022. Can a Self-Driving 40-Ton Truck Be Safe? Developers Say Yes. *Bloomberg.com*, 9 Jan.

Lambe, T.W., 1958. The structure of compacted clays. *Journal of the Soil Mechanics and Foundations Division*, 84 (2), 1654–1.

Li, M. and Wang, H., 2019. Development of ANN-GA program for backcalculation of pavement moduli under FWD testing with viscoelastic and nonlinear parameters. *International Journal of Pavement Engineering*, 20 (4), 490–498.

Liang, R.Y., Rabab'ah, S., and Khasawneh, M., 2008. Predicting Moisture-Dependent Resilient Modulus of Cohesive Soils Using Soil Suction Concept. *Journal of Transportation Engineering*, 134 (1), 34–40.

Ling, M., Luo, X., Chen, Y., Gu, F., and Lytton, R.L., 2020. Mechanistic-empirical models for top-down cracking initiation of asphalt pavements. *International Journal of Pavement Engineering*, 21 (4), 464–473.

Ling, M., Luo, X., Chen, Y., Hu, S., and Lytton, R.L., 2019. A calibrated mechanics-based model for top-down cracking of asphalt pavements. *Construction and Building Materials*, 208, 102–112.

Ling, M., Luo, X., Hu, S., Gu, F., and Lytton, R.L., 2017. Numerical Modeling and Artificial Neural Network for Predicting J-Integral of Top-Down Cracking in Asphalt Pavement. *Transportation Research Record*, 2631 (1), 83–95.

Lira, B., Jelagin, D., and Birgisson, B., 2013. Gradation-based framework for asphalt mixture. *Materials and Structures*, 46 (8), 1401–1414.

Litman, T., 2017. *Autonomous vehicle implementation predictions*. Victoria Transport Policy Institute Victoria, BC, Canada.

Liu, Y., Tight, M., Sun, Q., and Kang, R., 2019. A systematic review: Road infrastructure requirement for Connected and Autonomous Vehicles (CAVs). *Journal of Physics: Conference Series*, 1187 (4), 042073.

LTPP InfoPave, 2020. Research quality pavement performance information. Available from: http://www.infopave.com/.

Lu, D., Li, Z., and Huang, D., 2017. Platooning as a service of autonomous vehicles. *In*: *2017 IEEE 18th International Symposium on A World of Wireless, Mobile and Multimedia Networks (WoWMoM)*. IEEE, 1–6.

Luo, X., Gu, F., Ling, M., and Lytton, R.L., 2018. Review of mechanistic-empirical modeling of top-down cracking in asphalt pavements. *Construction and Building Materials*, 191, 1053–1070.

Luo, X., Zhang, Y., and Lytton, R.L., 2016. Implementation of pseudo J-integral based Paris' law for fatigue cracking in asphalt mixtures and pavements. *Materials and Structures*, 49 (9), 3713–3732.

Lytton, R., 1997. Engineering structures in expansive soils. Keynote address. Proceedings of the third international symposium on unsaturated soils, Rio de Janeiro, Brazil.

Lytton, R.L., 1994. Prediction of movement in expansive clays. Presented at the Vertical and horizontal deformations of foundations and embankments, ASCE, 1827–1845.

Lytton, R.L., 1996. Foundations and pavements on unsaturated soils. Proceedings of the first international conference on unsaturated soils/unsat '95/Paris/France.

Lytton, R.L., Luo, X., Ling, M., Chen, Y., Hu, S., and Gu, F., 2018. *A Mechanistic–Empirical Model for Top–Down Cracking of Asphalt Pavements Layers*.

Lytton, R.L., Tsai, F.L., Lee, S.I., Luo, R., Hu, S., and Zhou, F., 2010. Models for predicting reflection cracking of hot-mix asphalt overlays. *NCHRP report*, 669, 48–56.

Lytton, R.L., Uzan, J., Fernando, E.G., Roque, R., Hiltunen, D., and Stoffels, S.M., 1993. *Development and validation of performance prediction models and specifications for asphalt binders and paving mixes*. Strategic Highway Research Program Washington, DC.

Mallick, R.B. and El-Korchi, T., 2008. *Pavement engineering: principles and practice*. CRC Press.

Mancuso, C., Vassallo, R., and d'Onofrio, A., 2002. Small strain behavior of a silty sand in controlled-suction resonant column torsional shear tests. *Canadian Geotechnical Journal*, 39 (1), 22–31.

Mather, J.R., 1974. *Climatology: fundamentals and applications*.

McKeen, R.G. and Johnson, L.D., 1990. Climate-Controlled Soil Design Parameters for Mat Foundations. *Journal of Geotechnical Engineering-Asce*, 116 (7), 1073–1094.

Mitchell, P.W., 1979. The structural analysis of footings on expansive soil. Presented at the Expansive Soils, ASCE, 438–447.

Moossazadeh, J. and Witczak, M.W., 1981. Prediction of subgrade moduli for soil that exhibits nonlinear behavior. *Transportation Research Record*, (810).

National Academies of Sciences and Medicine, 2020. *Reducing fuel consumption and greenhouse gas emissions of medium-and heavy-duty vehicles, phase two*. National Academies Press.

Ng, C.W.W., Zhou, C., Yuan, Q., and Xu, J., 2013. Resilient modulus of unsaturated subgrade soil: experimental and theoretical investigations. *Canadian Geotechnical Journal*, 50 (2), 223–232.

Noorvand, H., Karnati, G., and Underwood, B.S., 2017. Autonomous Vehicles: Assessment of the Implications of Truck Positioning on Flexible Pavement Performance and Design. *Transportation Research Record*, 2640 (1), 21–28.

Onifade, I. and Birgisson, B., 2020. Improved models for the prediction of asphalt binder dynamic shear modulus and phase angle. *Construction and Building Materials*, 250, 118753.

Onifade, I., Dinegdae, Y., and Birgisson, B., 2017. Hierarchical approach for fatigue cracking performance evaluation in asphalt pavements. *Frontiers of Structural and Civil Engineering*, 11 (3), 257–269.

Ozer, H., Al-Qadi, I.L., and Duarte, C.A., 2011. Effects of Nonuniform and Three-Dimensional Contact Stresses on Near-Surface Cracking. *Transportation Research Record*, 2210 (1), 97–105.

Pellinen, T., Rowe, G., and Biswas, K., 2004. Evaluation of surface (top down) longitudinal wheel path cracking. *Joint Transportation Research Program*, 93.

Peng, J., Zhang, J., Li, J., Yao, Y., and Zhang, A., 2020. Modeling humidity and stress-dependent subgrade soils in flexible pavements. *Computers and Geotechnics*, 120, 103413.

Pezo, R.F., 1993. A general method of reporting resilient modulus tests of soils, a pavement engineer's point of view. *In*: *72nd Annual Meeting of the TRB*.

Powell, M.J., 2009. The BOBYQA algorithm for bound constrained optimization without derivatives. *Cambridge NA Report NA2009/06, University of Cambridge, Cambridge*, 26.

Puppala, A.J., Mohammad, L.N., and Allen, A., 1999. Permanent Deformation Characterization of Subgrade Soils from RLT Test. *Journal of Materials in Civil Engineering*, 11 (4), 274–282.

Raad, L. and Figueroa, J.L., 1980. Load Response of Transportation Support Systems. *Transportation Engineering Journal of ASCE*, 106 (1), 111–128.

Rainie, L., Funk, C., Anderson, M., and Tyson, A., 2022. AI and Human Enhancement: Americans' Openness Is Tempered by a Range of Concerns. *Pew Research Center: Internet, Science & Tech*.

Randall, J.L., 2012. Traffic Recorder Instruction Manual.

Research and Markets, 2022. Autonomous Trucking Market by Infrastructure, Trucking Type and Business Model 2022 - 2027 [online]. Available from: https://www.researchandmarkets.com/reports/5403245/autonomous-trucking-market-by-infrastructure [Accessed 11 Aug 2022].

Roque, R., Birgisson, B., Drakos, C., and Dietrich, B., 2004. Development and Field Evaluation of Energy-Based Criteria for Top-down Cracking Performance of Hot Mix Asphalt (with discussion). *In*: *Journal of the Association of Asphalt Paving Technologists*. Presented at the Technical Sessions of the Journal of the Association of Asphalt Paving Technologists. 2004 Proceedings.

Roque, R., Birgisson, B., Sangpetngam, B., and Zhang, Z., 2002. Hot mix asphalt fracture mechanics: a fundamental crack growth law for asphalt mixtures. *In*: *Journal of the Association of Asphalt Paving Technologists*. Presented at the Asphalt Paving Technology 2002Association of Asphalt Paving Technologists (AAPT).

Roque, R., Zou, J., Kim, Y.R., Baek, C., Thirunavukkarasu, S., Underwood, B.S., and Guddati, M.N., 2010. *Top-down cracking of hot-mix asphalt layers: Models for initiation and propagation*.

SAE International, 2018. Taxonomy and definitions for terms related to driving automation systems for on-road motor vehicles. *SAE*.

Saha, S., Gu, F., Luo, X., and Lytton, R.L., 2018a. Prediction of Soil-Water Characteristic Curve for Unbound Material Using Fredlund–Xing Equation-Based ANN Approach. *Journal of Materials in Civil Engineering*, 30 (5), 06018002.

Saha, S., Gu, F., Luo, X., and Lytton, R.L., 2018b. Use of an artificial neural network approach for the prediction of resilient modulus for unbound granular material. *Transportation Research Record*, 2672 (52), 23–33.

Saha, S., Hariharan, N., Gu, F., Luo, X., Little, D.N., and Lytton, R.L., 2019. Development of a mechanistic-empirical model to predict equilibrium suction for subgrade soil. *Journal of Hydrology*, 575, 221–233.

Salour, F. and Erlingsson, S., 2013. Investigation of a pavement structural behaviour during spring thaw using falling weight deflectometer. *Road Materials and Pavement Design*, 14 (1), 141–158.

Schapery, R.A., 1984. Correspondence principles and a generalized J integral for large deformation and fracture analysis of viscoelastic media. *International journal of fracture*, 25 (3), 195–223.

Seed, H.B., Chan, C.K., and Lee, C.E., 1962. Resilience characteristics of subgrade soils and their relation to fatigue failures in asphalt pavements. Presented at the International Conference on the Structural Design of Asphalt Pavements. Supplement University of Michigan, Ann Arbor.

Seed, H.B., Mitry, F.G., Monismith, C.L., and Chan, C.K., 1967. Prediction of flexible pavement deflections from laboratory repeated-load tests. *NCHRP Report*, (35).

Shepardson, D., 2018. U.S. spending plan include $100 million for autonomous cars research, testing. *Reuters*, 22 Mar.

Short, J. and Murray, D., 2016. Identifying autonomous vehicle technology impacts on the trucking industry.

Siddharthan, R.V., Nasimifar, M., Tan, X., and Hajj, E.Y., 2017. Investigation of impact of wheel wander on pavement performance. *Road Materials and Pavement Design*, 18 (2), 390–407.

Sirin, O., Paul, D.K., and Kassem, E., 2018. State of the Art Study on Aging of Asphalt Mixtures and Use of Antioxidant Additives. *Advances in Civil Engineering*, 2018, e3428961.

Slowik, P. and Sharpe, B., 2018. Automation in the long haul: Challenges and opportunities of autonomous heavy-duty trucking in the United States. *The International Council on Clean Transportation*, 1–30.

Sun, X. and Yin, Y., 2019. Behaviorally stable vehicle platooning for energy savings. *Transportation research part C: emerging technologies*, 99, 37–52.

Teshale, E.Z., Shongtao, D., and Walubita, L.F., 2019. Evaluation of Unbound Aggregate Base Layers using Moisture Monitoring Data. *Transportation Research Record*, 2673 (3), 399–409.

Thompson, M.R. and Robnett, Q.L., 1979. Resilient Properties of Subgrade Soils. *Transportation Engineering Journal of ASCE*, 105 (1), 71–89.

Thornthwaite, C.W., 1948. An Approach toward a Rational Classification of Climate. *Geographical Review*, 38 (1), 55–94.

Thornthwaite, C.W. and Mather, J.R., 1955. The water balance.

Thulaseedharan, N.P. and Yarnold, M.T., 2020. Prioritization of Texas prestressed concrete bridges for future truck platoon loading. *Bridge Structures*, 16 (4), 155–167.

Tohme, R. and Yarnold, M., 2020. Steel bridge load rating impacts owing to autonomous truck platoons. *Transportation Research Record*, 2674 (2), 57–67.

TuSimple, 2023. Official website.

Tutumluer, E., 1995. *Predicting behavior of flexible pavements with granular bases*. Georgia Institute of Technology.

USDOT, 2016. Traffic monitoring guide. Washington, DC: Office of Highway Policy Information, FHWA.

Uzan, J., 1985. Characterization of granular material. *Transportation research record*, 1022 (1), 52–59.

Vahidi, A. and Sciarretta, A., 2018. Energy saving potentials of connected and automated vehicles. *Transportation Research Part C: Emerging Technologies*, 95, 822–843.

Varma, S. and Emin Kutay, M., 2016. Backcalculation of viscoelastic and nonlinear flexible pavement layer properties from falling weight deflections. *International Journal of Pavement Engineering*, 17 (5), 388–402.

VdM Steyn, W.J. and Fisher, C., 2008. Technical Memorandum: Phase1 of HVS Testing. CSIR Report CSIR/BE/IE/ER/2007/0033/B. *CSIR Built Environment, Pretoria*.

Wang, H., Ozer, H., Al-Qadi, I.L., and Duarte, C.A., 2013. Analysis of Near-Surface Cracking under Critical Loading Conditions Using Uncracked and Cracked Pavement Models. *Journal of Transportation Engineering*, 139 (10), 992–1000.

Weisser, H., 1998. Autonomous driving on vehicle test tracks: overview, motivation, and concept. *In*: *IEEE International Conference on Intelligent Vehicles. Proceedings of the 1998 IEEE International Conference on Intelligent Vehicles Vol. 2*.

Willmott, C.J. and Feddema, J.J., 1992. A More Rational Climatic Moisture Index*. *The Professional Geographer*, 44 (1), 84–88.

Witczak, M. and Uzan, J., 1988. The universal airport design system, report I of IV: granular material characterization. *Department of Civil Engineering, University of Maryland, College Park*.

Witczak, M.W. and Fonseca, O.A., 1996. Revised Predictive Model for Dynamic (Complex) Modulus of Asphalt Mixtures [online]. Available from:

https://journals.sagepub.com/doi/abs/10.1177/0361198196154000103 [Accessed 27 May 2022].

Witczak, M.W., Zapata, C.E., and Houston, W.N., 2006. *Models Incorporated into the Current Enhanced Integrated Climatic Model for Used in Version 1.0 of the MEPDG. NCHRP 9-23 Project Report*. Arizona State University, Tempe, Arizona.

Yang, S.-R., Huang, W.-H., and Tai, Y.-T., 2005. Variation of Resilient Modulus with Soil Suction for Compacted Subgrade Soils. *Transportation Research Record*, 1913 (1), 99–106.

Yarnold, M.T. and Weidner, J.S., 2019. Truck platoon impacts on steel girder bridges. *Journal of Bridge Engineering*, 24 (7), 06019003.

Yideti, T.F., Birgisson, B., Jelagin, D., and Guarin, A., 2013. Packing theory-based framework to evaluate permanent deformation of unbound granular materials. *International Journal of Pavement Engineering*, 14 (3), 309–320.

Yoshino, H., Yamaguchi, R., and Mikami, M., 2018. 5G Overall System Trial - An application of 5G Ultra-Low-Latency Communication to Truck Platooning. *The Internaional Telecommunication Union Association of Japan*.

Yue, E. and Veenstra, J.N., 2018. Prediction of active zone depth in Oklahoma using soil matric suction. *Journal of GeoEngineering*, 13 (1), 029–038.

Zapata, C.E., Perera, Y.Y., and Houston, W.N., 2009. Matric Suction Prediction Model in New AASHTO Mechanistic–Empirical Pavement Design Guide. *Transportation Research Record*, 2101 (1), 53–62.

Zhang, D., Birgisson, B., Luo, X., and Onifade, I., 2019a. A new short-term aging model for asphalt binders based on rheological activation energy. *Materials and Structures*, 52 (4), 68.

Zhang, D., Birgisson, B., Luo, X., and Onifade, I., 2019b. A new long-term aging model for asphalt pavements using morphology-kinetics based approach. *Construction and Building Materials*, 229, 117032.

Zhang, J., Peng, J., Liu, W., and Lu, W., 2021. Predicting resilient modulus of fine-grained subgrade soils considering relative compaction and matric suction. *Road Materials and Pavement Design*, 22 (3), 703–715.

Zhang, Y., Birgisson, B., and Lytton, R.L., 2016. Weak form equation–based finite-element modeling of viscoelastic asphalt mixtures. *Journal of Materials in Civil Engineering*, 28 (2).

Zhang, Y., Gu, F., Luo, X., Birgisson, B., and Lytton, R.L., 2018. Modeling Stress-Dependent Anisotropic Elastoplastic Unbound Granular Base in Flexible Pavements. *Transportation Research Record*, 2672 (52), 46–56.

Zhang, Z., Roque, R., Birgisson, B., and Sangpetngam, B., 2001. Identification and verification of a suitable crack growth law (with discussion). *In*: *Journal of the Association of Asphalt Paving Technologists*. Presented at the Asphalt Paving Technology 2001Association of Asphalt Paving Technologists (AAPT).

Zhao, Y., Tan, Y., and Zhou, C., 2012. Determination of axle load spectra based on percentage of overloaded trucks for mechanistic-empirical pavement design. *Road Materials and Pavement Design*, 13 (4), 850–863.

Zhou, F., Hu, S., Xue, W., and Flintsch, G.W., 2019. *Optimizing the Lateral Wandering of Automated Vehicles to Improve Roadway Safety and Pavement Life*. SAFE-D: Safety Through Disruption National University Transportation Center, Report.

APPENDIX A

Table A1 Pavement structural properties and binder type of field sections.

Section Name	Layer thickness (in.)			Layer modulus (ksi)			Binder type
	AC	Base	Sub-base	Base	Subbase	Subgrade	
Florida source							
Charlotte (I75-1A),FL	6.54	12.00	12.00	54.80	50.10	30.10	PG 67-22
Charlotte (I75-1B),FL	6.24	12.00	12.00	63.60	51.40	36.10	PG 67-22
Lee (I75-3),FL	6.48	12.00	12.00	59.60	34.80	36.20	PG 67-22
Hamilton(I-75SB),FL	7.40	22.32	-	74.86	-	35.54	PG 64-22
Marion (US-301 SB),FL	6.42	22.80	-	60.23	-	36.64	PG 64-22
Duval2(I-295SB),FL	7.76	22.01	-	65.86	-	31.87	PG 76-22
St.Lucie (TPK-2C),FL	6.10	12.00	12.00	34.00	19.00	24.00	PG 67-22
Alachua (NW 39-1C),FL	4.00	12.50	12.00	28.00	71.00	28.00	PG 67-22
Seminole (SR46),FL	5.00	6.50	-	200.00	-	16.80	PG 67-22
Alachua (SR-121 SB),FL	5.51	20.51	-	50.98	-	23.07	PG 67-22
Bradford (SR-16EB),FL	7.76	17.99	-	29.33	-	32.25	PG 67-22
Sweden source							
T-205-1 Karlstad,SE	3.54	5.91	20.47	37.22	27.18	63.50	160/220
U-580-1:2 Västerås-Hässlö,SE	1.77	4.33	20.47	117.16	20.96	25.07	160/220
P-RV46-1 Såtenäs,SE	2.76	4.92	19.69	145.15	17.42	41.44	160/220
T-205-2 Ställdalen,SE	1.97	3.15	20.87	112.75	20.30	15.98	160/220
LTPP source							
48-3669,TX	5.80	15.90	-	12.72	-	16.88	PG 70-22S
48-1119,TX	6.20	7.20	-	27.11	-	4.83	AC-20
48-3729,TX	10.10	10.50	5.40	60.50	34.25	14.00	PG 64-22

Table A2. Asphalt material properties of field section

	Gradation										Volumetrics			
Sieve size	1.5"	1"	3/4"	1/2"	3/8"	P4	P10	P40	P80	P200	Va	Vbe	VMA	Pb
Florida source														
Charlotte (I75-1A),FL	100	100	100	95.7	91.8	73.6	57.6	26.9	12.7	5.9	5.4	10.7	16.1	6.2
Charlotte (I75-1B),FL	100	100	100	97.7	93.7	74.6	55.6	25.6	12.3	5.6	3.2	10.7	13.9	6.8
Lee (I75-3),FL	100	100	100	93.8	86.2	65.1	52.7	27.3	13.2	5.5	7.2	8.2	15.4	6.6
Hamilton(I-75SB),FL	100	100	100	93.0	89.0	45.0	38.0	28.2	18.9	4.9	4.2	10.0	14.2	6.5
Marion (US-301 SB),FL	100	100	100	93.0	88.0	75.0	55.6	25.6	12.3	5.0	5.8	10.1	15.9	6.5
Duval2(I-295SB),FL	100	100	100	95.0	87.0	59.0	50.4	23.7	13.1	4.7	5.8	5.3	11.1	6.5
St.Lucie (TPK-2C),FL	100	100	100	99.3	94.8	67.9	54.2	22.9	10.7	7.3	4.6	10.7	15.3	5.2
Alachua (NW 39-1C),FL	100	100	100	91.0	76.2	52.7	40.3	28.2	18.9	5.5	8.9	9.9	18.8	5.4
Seminole (SR46),FL	100	100	100	99.5	98.2	75.1	56.7	30.6	14.2	9.0	5.7	10.3	16.0	5.9
Alachua (SR-121 SB),FL	100	100	100	99.5	90.0	73.0	55.5	27.3	11.7	5.5	7.3	7.3	14.6	6.0
Bradford (SR-16EB),FL	100	100	100	97.9	88.0	67.0	51.0	24.0	10.0	5.4	9.2	7.8	17.0	6.0
Sweden source														
T-205-1 Karlstad,SE	100	94.0	82.5	66.0	57.5	43.0	30.0	14.5	9.5	6.0	5.2	10.7	15.9	4.2
U-580-1:2 Västerås-Hässlö,SE	100	94.0	82.5	66.0	57.5	43.0	30.0	14.5	9.5	6.0	5.2	10.7	15.9	4.2
P-RV46-1 Såtenäs,SE	100	94.0	82.5	66.0	57.5	43.0	30.0	14.5	9.5	6.0	5.2	10.7	15.9	4.2
T-205-2 Ställdalen,SE	100	94.0	82.5	66.0	57.5	43.0	30.0	14.5	9.5	6.0	5.2	10.7	15.9	4.2
LTPP source														
48-3669,TX	100	100	100	100	95.0	75.0	56.0	47.0	18.0	6.0	5.2	10.5	15.7	6.0
48-1119,TX	100	100	100	87.0	75.0	49.0	36.0	34.0	17.0	2.0	4.7	7.9	12.6	6.0
48-3729,TX	100	100	100	100.0	98.0	59.0	35.0	28.0	18.0	8.7	4.6	14.9	19.5	6.2

Table A3. Traffic Data for Florida Sections

Section Name	ESALs_yearly	Age	Percent Truck	Truck Factor
Charlotte (I75-1A),FL	573000	15	0.148	1.595
Charlotte (I75-1B),FL	558000	14	0.146	1.595
Lee (I75-3),FL	674000	15	0.153	1.595
Hamilton(I-75SB),FL	1040000	11	0.243	1.595
Marion (US-301 SB),FL	510000	11	0.219	1.595
Duval2(I-295SB),FL	1410000	-	-	-
St.Lucie (TPK-2C),FL	166000	10	0.123	1.03
Alachua (NW 39-1C),FL	190000	14	0.022	1.03
Seminole (SR46),FL	141983	14	0.125	1.03
Alachua (SR-121 SB),FL	60000	-	-	-
Bradford (SR-16EB),FL	40000	13	0.081	1.03

Table A4. Traffic Data for Sweden Sections (measured when open to traffic)

	T-205-1 Karlstad,SE	U-580-1:2 Västerås-Hässlö,SE	P-RV46-1 Såtenäs,SE	T-205-2 Ställdalen,SE
Annual average daily traffic (AADT)	1487	400	2027	942
Percent Truck (%T)	14	20	14	11.68
Truck factor (TF)	1.7	1.7	1.7	1.7
Directional distribution factor (%D)	50	50	50	50
Lane distribution factor (%L)	92	92	92	92
Traffic growth rate (%r)	1	2.6	1.3	1

Table A5. AADTT for Texas (USA) Sections

Time (yr)	48-3669, TX	48-1119, TX	48-3729, TX
0	283	107	766
1	179	113	766
2	179	119	766
3	167	125	766
4	311	131	766
5	218	138	766
6	222	145	766
7	144	153	766
8	99	161	766
9	73	169	766
10	112	178	766
11	133	187	931
12	100	197	1369
13	160	207	1369
14	139	281	1489
15	152	205	1130
16	162	262	1288
17	148	257	1275
18	100	265	1286
19	160	260	1263